SOFT CONTACT MODELING FOR IN-HAND MANIPULATION CONTROL AND PLANNING

Marco Costanzo

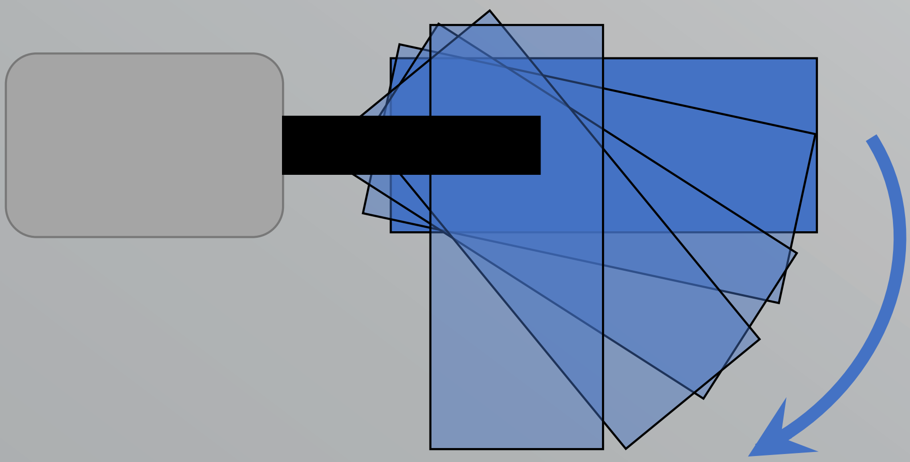

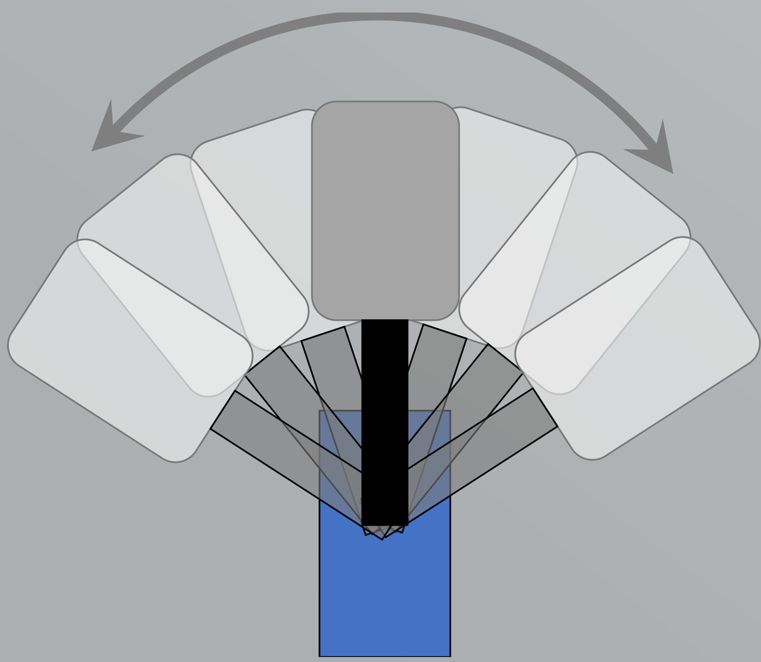

Università
degli Studi
della Campania
Luigi Vanvitelli

Dipartimento di
Ingegneria

Dottorato di Ricerca in
Ingegneria Industriale e dell'Informazione
XXXIII Ciclo

Ph.D. Thesis

Soft Contact Modeling for In-Hand Manipulation Control and Planning

S.S.D. ING-INF/04-Automatica

A.A. 2019/2020

Author
Costanzo Marco
Matr. D129/40

Coordinator
Prof.
Oronzio Manca

Advisor
Prof.
Giuseppe De Maria

Co-Advisor
Prof.
Ciro Natale

Marco Costanzo Oronzio Manca Giuseppe De Maria Ciro Natale

The work presented in this thesis has been developed within the REFILLS project, that has received funding from the European Commission under the European Union's Horizon 2020 Research and Innovation programme (grant agreement No 731590 - REFILLS).

Soft Contact Modeling for In-Hand Manipulation Control and Planning
by Marco Costanzo

Sommario

Questa tesi tratta la manipolazione robotica destra di oggetti facendo leva sul concetto di *destrezza estrinseca*. La destrezza non è limitata all'intriseca abilità della mano robotica, infatti è possibile manipolare un oggetto usando risorse esterne come la gravità o i contatti con l'ambiente. Queste abilità non richiedono l'utilizzo di mani complesse ma possono essere eseguite da semplici gripper paralleli.

La prima abilità necessaria per la manipolazione di oggetti è la *slipping avoidance*. Consiste nell'afferrare un oggetto evitando scivolamenti sia translazionali che rotazionali. La tesi si sofferma su una particolare abilità di manipolazione chiamata *pivoting*. Essa consiste nel far ruotare un oggetto nella mano usando la gravità. Questa manovra può essere eseguita in due modi. Il primo, chiamato *object pivoting*, consiste nell'avere il gripper fermo nello spazio mentre l'oggetto ruota con un movimento simile ad un pendolo. Il secondo, chiamato *gripper pivoting*, corrisponde alla manovra duale e consiste nell'avere l'oggetto fermo nello spazio mentre il gripper ruota attorno all'asse di grasp così da cambiare l'orientamento relativo tra il gripper e l'oggetto. Il problema è affrontato dal punto di vista del controllo con un approccio basato sul modello. Questa tesi presenta un nuovo modello di *slider planare* che descrive il moto come una pura rotazione istantanea attorno al cosiddetto Centro di Rotazione e unisce il concetto di Superficie Limite con il modello dinamico di attrito di LuGre. Dopo una completa analisi di stabilità e osservabilità, viene proposto un osservatore non lineare per stimare la velocità di scivolamento. Infine, basandosi sulla modellazione fatta, vengono presentati gli algoritmi di slipping avoidance e pivoting.

Le abilità di manipolazione in-hand, da sole, non sono abbastanza. Per usare il loro potenziale con un più alto livello di autonomia, questa tesi propone due pianificatori di moto/manipolazione che hanno l'abilità di sfruttarlo. Infine, la tesi presenta un *task planner* di più alto livello che usa uno dei suddetti pianificatori ed è in grado sia di eseguire un compito di *pick-and-place* che scegliere automaticamente la posa di presa iniziale. L'approccio è validato sperimentalmente in uno scenario simulato in laboratorio simile a quello di un supermercato.

Abstract

The focus of this thesis is on the dexterous robotic manipulation of objects. We leverage the concept of *extrinsic dexterity*. The dexterity is not limited to the robot hand intrinsic capability, indeed, it is possible to manipulate an object by using external aids, such as gravity or the contact with the environment. Such abilities do not require complex hands but they can be performed by simple parallel-jaw grippers.

The first ability that the grasping device needs is the *slipping avoidance*. It consists in firmly grasping an object avoiding both translational and rotational sliding. Then, we focus on a particular in-hand manipulation ability, namely, *pivoting*. It consists in rotating the grasped object in-hand by using gravity. This maneuver can be executed in two ways. The first one, called *object pivoting*, consists in having the gripper fixed in the space while the object rotates in a pendulum-like motion. The second one, called *gripper pivoting*, is the dual one and consists in having the object fixed in the space while the gripper rotates about the grasp axis so as to change the relative orientation between the gripper and the object. The problem is addressed from a control point of view by following a model-based approach. This thesis presents a novel planar slider dynamic model that describes the motion as a pure instantaneous rotation about the so-called Center of Rotation and merges the Limit Surface concept with the LuGre dynamic friction model. After a complete stability and observability analysis, a nonlinear observer is designed to estimate the slipping velocity. Finally, basing on the proposed framework, the slipping avoidance and pivoting algorithms are presented.

The in-hand manipulation skills, on their own, are not enough. To use this potential with a higher degree of autonomy, this thesis proposes two motion/manipulation planning strategies that have the ability to use it. Finally, the thesis presents a higher-level task planner that uses one of the aforementioned manipulation planners to both execute a complete pick and place task and automatically choose the initial grasp pose. The proposed approach is experimentally validated in a lab-simulated in-store logistic scenario.

Acknowledgments

It is hard to thank in a few words the people that directly or indirectly supported me during these years.

I wish to express my sincere gratitude to my advisors, Prof. Giuseppe De Maria and Prof. Ciro Natale, for their constant and enthusiastic support in these years.

Thanks to Francesca, for your lovely support, for distracting me when I needed it, and for all the moments we have spent these years.

Thanks to my parents, thank you for supporting my decisions without knowing exactly what I was doing.

I would like to thank all my friends and colleagues at university, old friends like Antonio, Giovanni, and Gaetano, and new ones like all the Ph.D. students and researchers that I have met these years. Thank you guys for all the funny lunches and for the time spent together. Special thanks to the foreign guys, they made me richer in many ways. “Uè Man!” thank you!

Contents

Notation

The symbols are chosen according to the following conventions:

- Scalar values or signals are denoted by italic letters such as x;
- Vectors are denoted by boldface lowercase letters such as $\boldsymbol{x}$;
- Matrices are denoted by boldface uppercase letters such as $\boldsymbol{A}$;
- Sets are denoted by calligraphic letters such as $\mathcal{Z}$.

This thesis uses the following mathematical symbolism:

$\mathrm{sign}(\cdot)$	sign of a scalar, not defined at 0
$\boldsymbol{x} \times \boldsymbol{y}$	cross product between the vectors $\boldsymbol{x}$ and $\boldsymbol{y}$
$\mathcal{L}_{\boldsymbol{f}}^{i}$	Lie derivative operator of order i along the vector function $\boldsymbol{f}(\cdot)$
$\boldsymbol{x}^{b}$	vector $\boldsymbol{x}$ expressed with reference to the frame $\{b\}$.
$\boldsymbol{R}_{a}^{b}$	orthonormal rotation matrix that represents the rotation of the frame $\{a\}$ with reference to the frame $\{b\}$
$\boldsymbol{T}_{a}^{b}$	homogeneous rototranslation matrix that represents the frame $\{a\}$ with reference to the frame $\{b\}$

The following acronyms have a special meaning:

LS	Limit Surface
NLS	Normalized Limit Surface
CoR	Center of Rotation
CoP	Center of Pressure
μ	Coulomb friction coefficient
ρ	radius of the contact area for axisymmetric pressure distributions

δ, γ	parameters of the contact area radius model, namely, $\rho = \delta f_n^\gamma$
k	exponent parameter of the pressure distribution
f_n	normal load
f_t	tangential force
τ_n	torsional torque
f_{tf}	tangential friction force
τ_{nf}	torsional friction torque
f_{tLS}	tangential force belonging to the Limit Surface
τ_{nLS}	torsional torque belonging to the Limit Surface
c	CoR coordinate on the x-axis for axisymmetric pressure distributions
$\tilde{c}$	normalized c with respect to ρ
$f_{t\max}$	maximum possible value of f_{tLS} corresponding to an infinitely far CoR ($c \to \infty$)
$\tau_{n\max}$	maximum possible value of τ_{nLS} corresponding to a CoR located at the CoP ($c = 0$)
$\tilde{f}_t$	normalized tangential force with respect to $f_{t\max}$
$\tilde{\tau}_n$	normalized torsional torque with respect to $\tau_{n\max}$
$\tilde{f}_{tLS}$	normalized f_{tLS} with respect to $f_{t\max}$
$\tilde{\tau}_{nLS}$	normalized τ_{nLS} with respect to $\tau_{n\max}$
$\tilde{f}^*_{tLS}(\tilde{c})$, $\tilde{\tau}^*_{nLS}(\tilde{c})$	functions discriminating the shape of the NLS
f_{tv}	tangential viscous friction force
τ_{nv}	torsional viscous friction torque
β_A	viscous friction coefficient per area unit
σ_0	stiffness of the micro asperities in the LuGre model
$\sigma_1(f_n, c)$, $\sigma_1(\cdot)$	generalized viscous friction coefficient in the planar slider model
$g(f_n, c)$, $g(\cdot)$	maximum dry generalized friction torque in the planar slider model

Chapter 1

Introduction

Humans are able to pick a wide variety of tools (e.g., a pencil, pair of scissors, telephone, or screwdriver) and move them between fingers to shift to a useful grasp. Humans can trivially pick a pencil from the desk by using any convenient pick grasp pose and then subconsciously manipulate it by changing the grasp on the fly so that actually use the pencil and write on a paper. These kinds of tasks are possible thanks to the manipulation abilities of the human hand that is able to exploit the friction forces and the consequent rolling and sliding motion.

Sliding itself increases the dexterity of the hand but has to be controlled. This is possible if the force required to initiate the sliding and the resulting motion are predictable.

On the other hand, when holding a heavy (and possibly fragile) object, the main objective is to prevent unwanted slips while, at the same time, avoiding to damage the object. Also in this scenario, it is important to predict the force at which the sliding takes place so as to apply just a slightly greater force.

In robotics, most of the tasks involve pick and place operations. Safe grasp and the ability to change the pose of an object with respect to a world frame are the basic actions of a pick and place task. This may be performed by using just the arm dexterity with a firm grasp or by in-hand manipulation. In the first case, the object should be picked with a grasp configuration compatible with both the pick and place poses as they both need to belong to the robot workspace. This solution might be difficult to obtain or even it likely might not exist. Therefore, a regrasp phase might be needed with the resulting need for a buffer location and waste of time in the task execution. The solution with in-hand manipulation is certainly more efficient but requires more dexterity in the end effector.

At a first sight, one might think that in-hand manipulation can be performed only by multifingered hands (Controzzi, Cipriani, and Carrozza 2014; Grebenstein, Chalon, Friedl, et al. 2012; Kawasaki et al. 1999; Palli et al. 2014; Piazza et al. 2019; Shadow Robot Company 2003). However, currently available anthropomorphic robotic hands still have high complexity and cost (Grebenstein, Chalon, Roa, et al. 2018). The control of complex multifingered hands is handled in two main ways, namely, by resorting to dimensionality reduction using the concept of postural synergies (Santello, Flanders, and Soechting 1998), or, more recently, by applying learning strategies (Funabashi et al. 2020; Huang et al. 2016; van Hoof et al. 2015), even with soft fingers (Nassour et al. 2018). However, robotic handling applications in the real world mostly adopt simple grippers, especially in industrial and professional service environments. Parallel jaw grippers are by far the most widespread, owing to their reliability, low cost, and ease of integration and control. Such kind of gripper typically has one degree of freedom (DOF) and limited intrinsic dexterity; nevertheless, recent studies by Chavan-Dafle, Rodriguez, et al. (2014) and Stepputtis, Yang, and Ben Amor (2018) have demonstrated that they can be used to perform dexterous manipulation actions exploiting the so-called *extrinsic dexterity.* The dexterity is not given only by the degrees of freedom of the end-effector or manipulator, but also by external aids such as environment constraints or gravity.

Nowadays, manipulation (and, in general, robotics) applications use two main approaches: *model-based* and *model-free.*

Typically, model-based approaches use more or less complex models to describe the system and then apply a control strategy. As an example, Ho, Z. Wang, and Hirai (2013) propose a Beam bundle model to model a human fingertip during pushing and sliding actions. While, Reinecke et al. (2014) compare various approaches to detect slip, such as friction cones, vibration-based detection, and bandpass filtering.

Instead, model-free approaches prefer to construct the model or directly the control algorithm by using data and machine-learning techniques. Veiga et al. (2015) use tactile data and random forest classifiers to create slip predictors, and then use them in a feedback loop to avoid slippage. Spiers et al. (2016) use tactile sensors and random forests to achieve object classification. Other authors use a deep-learning approach and convolutional neural networks. For example, Meier et al. (2016) use deep-learning and tactile data to detect and distinguish translational and rotational slippage. Li, Dong, and Adelson (2018) merge tactile and visual data to detect slip, while Zapata-Impata, Gil, and Torres (2019) apply deep-learning to detect the slip direction.

A recent study by Rosset et al. (2019) compares a model-free and a model-based approach using spatial and temporal tactile data in slipping avoidance applications during pick-and-place tasks; the paper shows how the model-based approach performed better in their case of study. Recently, Zeng et al. (2020) propose a hybrid approach to solve a task in which a robot has to throw arbitrary objects. The authors implement a model-based controller and use a deep network to predict residuals on top of control parameters.

The work of this thesis belongs to the model-based approaches for in-hand manipulation that use force/tactile feedback. It has been developed under the European Commission's Horizon 2020 REFILLS research project. The REFILLS project proposes to develop solutions allowing robots to improve logistics processes in a supermarket, revolutionizing their current structure. Thus, despite the results presented in this thesis can be applied in other contexts, the experimental evaluation will be presented in an in-store logistic scenario. Nowadays, automation is improving the experience of customers at retail shops both in terms of ordering and customer comfort. One of the core activities is certainly logistics, this is because the average logistics costs in the retail sector are higher than for manufacturing companies. Additionally, up to 60% of the total operational store costs result from in-store logistics (Kuhn and Sternbeck 2013). In the last years, many robots have been sold in the logistic sector, especially the so-called UAV (Unmanned Autonomous Vehicles). 69 thousand units have been sold in 2017 (162% more than the previous year)(IFR International Federation of Robotics 2018). Nevertheless, there is still a lack of automation in the in-store logistics management. Most of the logistics tasks include item handling; item transportation; shelf replenishment and backroom management. Supermarket clerks perform these time-consuming, repetitive, inefficient, monotonous, and wearing tasks and the most time consuming one is certainly the shelf replenishment. Nowadays, it is very difficult to find an automated solution that fills supermarket shelves. This is because such tasks require sophisticated manipulation skills due to the very large number of items to handle, and their variety in terms of shape, surface, fragility, stiffness, and weight. Moreover, often simply pick and place them is not enough; pulling, pushing, rotating, and eventually relocating items in narrow spaces are required actions.

1.1 Objectives and Contributions

The objective of this thesis is to study the dynamics of an object grasped by a robotic gripper from a control point of view. Such investigation is aimed to provide a suitable framework for the in-hand manipulation that could be exploited for control and planning problems.

This thesis presents a model-based approach for in-hand manipulation and planning strategies able to exploit such abilities. The approach is based on a novel planar slider dynamic model. A planar slider is a rigid body in a spatially distributed contact with friction with a plane and it is able to translate and rotate subject to external forces and torques.

The basic concept on which the model is built is the Limit Surface (LS) theory, originally proposed by Goyal, Ruina, and Papadopoulos (1991a). In the LS framework, the planar motion of a body is described as a pure instantaneous rotation about the so-called Center of Rotation (COR). In static conditions, the LS provides the dry friction force and torque given the CoR position.

The first contribution of this thesis is a novel method to invert the LS relation and estimate the CoR position given the measure of the friction force and torque. Moreover, the LS framework is extended by describing also the viscous friction.

The second contribution is the aforementioned novel planar slider dynamic model. Given the CoR position, the dynamic model is built up by merging the LuGre dynamic friction model (Canudas De Wit et al. 1995) with the LS maximum dry friction. The result is a 1DOF velocity model that describes the sliding motion as a pure instantaneous rotation about CoR. Moreover, a complete stability and observability analysis is provided and a slipping velocity observer is proposed.

Finally, this thesis proposes a slipping controller built on top of the proposed framework that provides both slipping avoidance and controlled pivoting. The proposed approach needs measures of contact force and torques. The measurements are performed by the integrated force/tactile sensor SUN-Touch (Appendix B) presented by D'Amore et al. (2011) and De Maria, C. Natale, and Pirozzi (2012).

The manipulation abilities, on their own, are not enough. To fully use this new potential, they have to be combined with a motion planner able to exploit them. The last contribution of this thesis is a motion/manipulation planner built on top of standard motion planners and able to use the aforementioned manipulation abilities. This is done by adding an additional virtual joint to the robot kinematic chain that has to satisfy some feasibility constraints. The planner is able to execute a full pick-and-place task in an in-store logistic scenario by automatically choosing the grasp configuration and the slipping control modality.

1.2 Related Works

The recent literature is rich in works on robotics manipulation that uses tactile feedback, vision, or shape information.

Torres-Jara and L. Natale (2018) underline the importance of tactile feedback in robotic manipulation, the main idea of the paper is to exploit the tactile information generated by the interaction between the robot and the object so as to guide the exploration and consequent actions. Regoli et al. (2016) use tactile feedback to improve grasp stability, the paper proposes an approach based on both classical control theory and machine learning. Also Hogan et al. (2020) use tactile feedback, they provide a method to move an object to the desired pose using manipulation primitives (pull, push, and pivot) made available through a dual-palm robotic system and tactile feedback.

Grasping and in-hand manipulation are difficult to evaluate without appropriate metrics. Bottarel et al. (2020) propose a protocol and a set of metrics to evaluate the performance of a grasping pipeline. While Cruciani, Sundaralingam, et al. (2020) propose a benchmark to evaluate the planning and control aspects of an in-hand manipulation system defining the task as changing the grasp pose without placing the object in an intermediate location. Haustein et al. (2019) present a planning algorithm that exploits a dual robot arm to first compute a sequence of in-hand pushing actions to adjust the grasp pose and then place the object. Cruciani, Yin, and Kragic (2020) propose a planning algorithm to change the grasp pose by using object shape information, the main characteristic is the on-line construction of the so-called Dexterous Manipulation Graph while the planning algorithm is running.

Examples of in-hand manipulation with parallel grippers are provided by Chavan-Dafle and Rodriguez (2015) and Viña B. et al. (2016), where an adaptive control algorithm was used to allow a grasped object to rotate in-hand to achieve a given orientation. While, to accomplish the same task, Antonova et al. (2017) adopt a reinforcement learning approach.

Recent papers dealing with in-hand manipulation are proposed by Shi, Woodruff, et al. (2017), Zhou, Hou, and Mason (2019), Chavan-Dafle, Holladay, and Rodriguez (2020). The first one proposes a method for planning in-hand manipulation of a laminar object by acting on the acceleration of the gripper. The second one solves a planar pushing problem by making use of the differential flatness concept and the feedback linearization technique. Also the third one deals with pushing problems but it focuses on planning pushing trajectories based on the concept of motion cones. Shi, Weng, and Lynch (2020) study similar pushing problems introducing the concept of spring-sliding compliance, in this paper the fingertips are modeled as attached to multidimensional springs mounted to position-controlled anchors. Hou, Jia, and Mason (2019) solve the problem of reorienting a rigid object on a table using a two-fingered pinch gripper and introducing two motion primitives, namely, pivot-on-support and roll-on-support. The same authors in (Hou, Jia, and Mason 2020) deal with the problem of shared-grasp, i.e., a non-prehensile grasp where the object is in contact with both the robot hand and the environment.

A model-based approach for controlled sliding, like the one presented in this thesis, has to deal with friction modeling. A vast literature has been produced in this field. A first survey by Armstrong-Hélouvry, Dupont, and Canudas De Wit (1994) focuses on control applications where the main aim is to compensate undesired friction forces in motion control. A more recent review by Marques et al. (2016), including 21 static and dynamic friction models, testifies the current interest of the research community in the topic. Many friction models rely on classical Coulomb law that describes the relation between the normal load and the translational friction. But, in-hand manipulation involves also rotational slide, thus, a more general model should be used. A well-known method to extend the Coulomb law to the general case of a planar rototranslational motion is the Limit Surface (LS) theory developed by Goyal, Ruina, and Papadopoulos (1991a,b).

The first paper that exploited the LS theory to solve a control problem is (Howe and Cutkosky 1996), where an axisymmetric pressure distribution is assumed. To control also the rotational sliding motion, a friction torque is needed. It can take place only if the contact is distributed. For this reason, the contact is typically soft. The use of soft fingers for both grasping and manipulation is widespread as they can improve grasp stability and enlarge the variety of objects that can be handled. Xydas and Kao (1999) propose a quite general approach to model the LS for soft contacts.

The planar slider dynamic model proposed in this thesis is inspired by the LuGre model by Canudas De Wit et al. (1995). It is a 1DOF nonlinear model, simple but able to capture physical phenomena such as the stick-slip motion, the Stribeck effect in the incipient slipping, or the break-away force reduction caused by the rate of variation of the load. Coulomb and LuGre models, as they were originally formulated, are suitable for describing friction forces in linear motions. In many applications, such as the one in this thesis, it is important to withstand not only linear loads but also torsional ones. Of course, this can be achieved only if the contact is spatially distributed so that a torsional moment can exist.

Concerning slipping control strategies, many have been proposed in the past literature, such as (Engeberg and Meek 2013), where a frequency approach was used, or (Gunji et al. 2008; Heyneman and Cutkosky 2013; Kaboli, Yao, and Cheng 2016; Romano et al. 2011; Schoepfer et al. 2010; Ueda, Ikeda, and Ogasawara 2005), which proposed control strategies based on heuristics and sensor signal more or less correlated with the contact phenomenon.

The aforementioned pivoting maneuver has been performed in different ways, e.g., Viña B. et al. (2016) use both visual and tactile sensors, the visual feedback is used to control the object orientation, while the tactile sensor is used to control the grasp force. In this thesis, instead, only force sensors on the fingertip are used for both grasp force control and for executing the pivoting maneuver. Note that, performing the pivoting task using the sole tactile feedback and no vision is very challenging even for humans and an accurate control of the object orientation is not possible. However, in Chapter 3 this issue is solved by using a combination of pivoting and fixed grasp maneuvers.

1.3 Outline

This section briefly describes the outline of this thesis.

Chapter 2 – Soft Contact Modeling

This chapter recalls the Limit Surface theory (Goyal, Ruina, and Papadopoulos 1991a) and the concept of instantaneous Center of Rotation. Moreover, it proposes a novel method to estimate the CoR position given the friction forces and torques. Finally, it extends the limit surface concept to the case of viscous friction.

This chapter is an extension of the LS method described in the following publication:

M. Costanzo, G. De Maria, and C. Natale (2020b). "Two-Fingered In-Hand Object Handling Based on Force/Tactile Feedback". In: *IEEE Transactions on Robotics* 36.1, pp. 157–173, **Award**: "Fabrizio Flacco" Young Author Best Paper Award 2020, IEEE Robotics and Automation Society Italian Chapter.

Chapter 3 – Dynamic Modeling and Grasp Control

This chapter presents the dynamic model of the planar slider. It is a modified version of the LuGre dynamic friction model (Canudas De Wit et al. 1995) and describes the motion as a pure rotation about the CoR. It uses the

LS concept to compute the maximum dry friction needed by the LuGre model. After a complete stability and observability analysis, the chapter proposes a nonlinear observer aimed to estimate the slipping velocity. Finally, it proposes control strategies for slipping avoidance and in-hand manipulation that exploited the proposed framework enabling the *pivoting* abilities.

This chapter is mainly based on and extends the following publications:

A. Cavallo, M. Costanzo, G. De Maria, and C. Natale (2020). "Modeling and slipping control of a planar slider". In: *Automatica* 115.108875. ISSN: 0005-1098.

M. Costanzo, G. De Maria, and C. Natale (2020a). "Control of Sliding Velocity in Robotic Object Pivoting Based on Tactile Sensing". In: *IFAC-PapersOnLine*. 21th IFAC World Congress, Berlin, Germany, July 12-17, 2020, pp. 10085–10090.

Chapter 4 – Manipulation Planning and Execution

This chapter proposes two approaches for motion/manipulation planning that use the in-hand manipulation abilities of Chapter 3. The resulting planners are built on top of standard motion planners. Moreover, this chapter presents a higher-level task planner that exploits the underling manipulation planner and is able to execute a complete pick and place task by automatically choosing the grasp pose.

This chapter extends the following publications:

M. Costanzo, S. Stelter, C. Natale, S. Pirozzi, G. Bartels, A. Maldonado, and M. Beetz (2020). "Manipulation Planning and Control for Shelf Replenishment". In: *IEEE Robotics and Automation Letters* 5.2, pp. 1595–1601.

M. Costanzo, G. De Maria, G. Lettera, and C. Natale (2020). "Grasp Control for Enhancing Dexterity of Parallel Grippers". In: *2020 IEEE International Conference on Robotics and Automation (ICRA).* 31 May - 31 August. Paris, France, pp. 524–530.

Chapter 5 – Conclusion

This chapter discusses the results and gives directions for possible future extensions.

Chapter 2

Soft Contact Modeling

Any manipulation task involves the interaction between the robot and an object through contact forces and torques. Typically, the robot touches an object by means of fingertips located on an artificial finger.

To allow in-hand manipulation, torques are of paramount importance. In fact, they are needed to change the orientation between the robot end effector and the grasped object. But a friction torque can take place only if the contact is distributed, the more the contact surface area, the more the friction torque that is possible to generate at the contact interface. For this reason, typically, the robots are equipped with soft fingertips that guarantee a distributed contact. Figure 2.1 shows an example, on the left a transparent object is pushed against a soft fingertip and the contact area is clearly visible, while, on the right, a soft fingertip pushes against an object and the finger deforms.

This chapter describes the relationship between sliding motion and applied forces and torques in a soft contact. To describe such a relationship it is necessary to model the friction phenomenon. In quasi-static conditions, the main approach is the classical Coulomb friction law and its rototranslational generalization, the Limit Surface (LS).

Three main contributions of this thesis are related to the Limit Surface concept.

The first contribution concerns a novel description of the LS in the normalized wrench space that allows us to describe the *forward LS problem* in a closed form, i.e., finding the dry friction wrench given the motion. The second one is a novel method to resolve the *inverse LS problem*, i.e., finding the motion given the friction forces.

It is worth clarifying that, in dynamics, the words *forward* and *inverse* assume the opposite meaning. In dynamics, the forward problem consists in finding the motion given the load. In the Limit Surface description, the

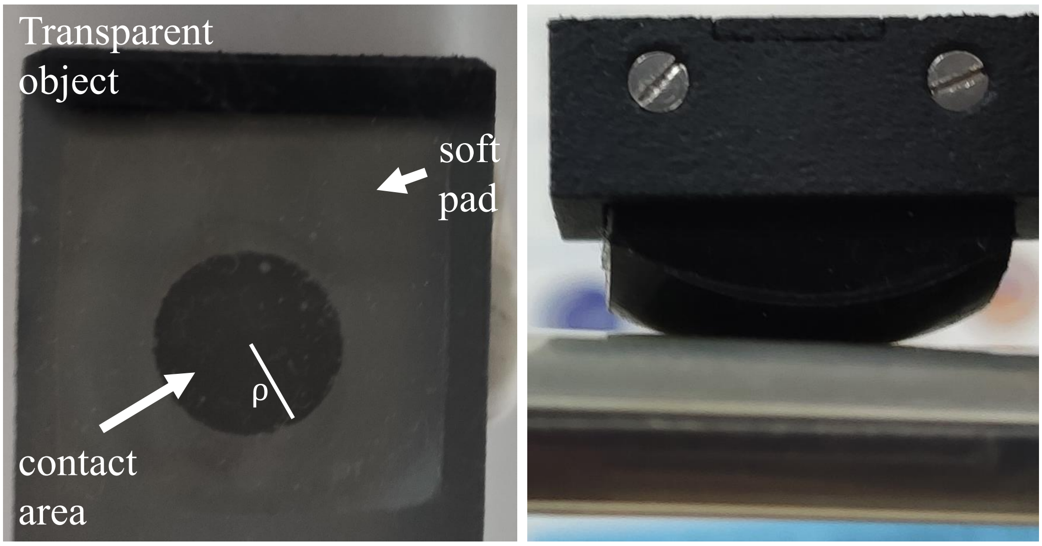

Figure 2.1: Example of soft contact. (left) A transparent object is pushed against a soft fingertip. (right) Side view of a soft fingertip pushing against an object. The contact is distributed over an area.

input is the instantaneous motion and the output is the dry friction which indirectly depends on the load.

The third contribution provides a unified description of the dry and viscous friction in the rototranslational case by using an extension of the Limit Surface concept. The generalization of the *inverse LS problem* in this case is provided as well.

The Limit Surface formulation is described in the following sections in order to show some mathematical details that are needed to formulate and solve the inverse problem and are typically overlooked in the Limit Surface literature. Then, this chapter will focus on the case of axisymmetric pressure distribution which describes a large set of real case scenarios involving soft fingertips. Finally, a suitable description of the LS in the normalized space will be exploited to solve the inverse LS problem. At the end of the chapter, the LS description is extended by introducing the viscous friction.

The framework provided in this chapter will be used in Chapter 3 to build the planar slider dynamic model. In particular, the LS provides a model for the maximum friction load and the LS inverse problem provides the instantaneous rototranslational motion.

2.1 Limit Surface – General Formulation

The Limit Surface (LS) concept has been developed in (Goyal 1989; Goyal, Ruina, and Papadopoulos 1991a). It provides a mapping between the applied forces and the resulting motion of a body sliding on a plane. Basically, the *forward LS problem* consists in computing the dry friction force and torque given the instantaneous rototranslational motion.

The following assumptions are needed:

1. a body slides on a planar surface;
2. the pressure distribution across the contact area is known;
3. the friction force depends only on the local value of pressure distribution and the direction of the slip, and not on the magnitude of the slipping velocity or its history;
4. the relative slipping velocity across the contact area corresponds to a pure rotation around a unique instantaneous Center of Rotation (CoR). This is always true for a rigid body and can be applied to the deformable ones if the deformation rate of the contact area is slow compared to the sliding speed.

The classical Coulomb dry friction law satisfies these assumptions, it states that for a body in sliding motion the tangential friction force is proportional to the normal force and opposed to the direction of the sliding velocity. So, in one dimension

$$\begin{array}{ll} \left|f_{tf}\right| \leq \mu f_n, & \text{if } v = 0 \\ f_{tf} = -\mu f_n \,\mathrm{sign}(v), & \text{if } v \neq 0 \end{array} \tag{2.1}$$

where f_{tf} is the translational friction force which lies to the contact area, μ is the friction coefficient, f_n is the normal force and v is the sliding velocity at the contact. When the sliding velocity is zero, the friction force is high enough to counteract any external force but it is always less than the maximum friction force μf_n. On the other hand, when the sliding velocity is non-zero, the magnitude of the friction force is equal to its maximum value and the direction is opposite to the sliding velocity.

The extension of this principle to two dimensions leads to the *Limit Surface* concept. In two dimensions, the direction of the slider velocity at each point of the contact surface contributes to the determination of the friction force. Moreover, because of the contact surface extension, the friction includes also a torsional moment normal to the surface and thus it is represented by a 3-dimensional wrench with two force components and one torque

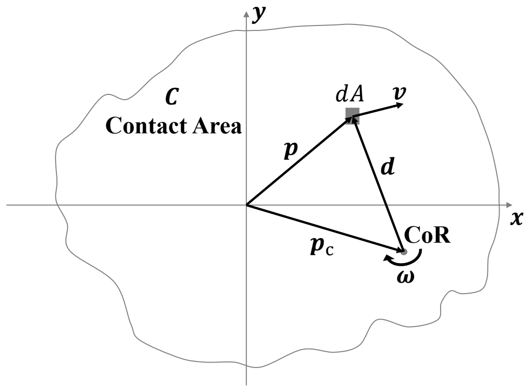

Figure 2.2: Contact area. In this example the object is rotating clockwise around the CoR, this results in a slider velocity $\boldsymbol{v}$ at the infinitesimal point $\boldsymbol{p}$.

component. The Limit Surface represents the boundary of the set of the possible friction wrenches that the contact can withstand, in other words, it is a generalization of the maximum Coulomb friction force μf_n.

Figure 2.2 shows the sliding plane. Let define a Cartesian coordinate system in the plane. It is convenient, but not mandatory, to place the origin in the friction weighted Center of Pressure (CoP) that can be computed as

$$\boldsymbol{p}_{\mathrm{CoP}} = \frac{\left[\int_{\mathcal{C}} x\mu(x,y)p(x,y)\,\mathrm{d}A \quad \int_{\mathcal{C}} y\mu(x,y)p(x,y)\,\mathrm{d}A\right]^T}{\int_{\mathcal{C}} \mu(x,y)p(x,y)\,\mathrm{d}A}, \tag{2.2}$$

where $\mu(x,y)$ and $p(x,y)$ are the values of the friction coefficient and the pressure distribution at location $\begin{bmatrix}x & y & 0\end{bmatrix}^T$, respectively, and $\mathrm{d}A$ is an infinitesimal area on the contact surface $\mathcal{C}$. With reference to Fig. 2.2, $\boldsymbol{p} = \begin{bmatrix}x & y & 0\end{bmatrix}^T$ is the position vector of the elementary contact area; $\boldsymbol{p}_c$ is the position vector of the CoR; $\boldsymbol{d}(x,y) = \boldsymbol{p} - \boldsymbol{p}_c = \begin{bmatrix}d_x & d_y & 0\end{bmatrix}^T$; $\boldsymbol{v}$ is the slider velocity at the point $\boldsymbol{p}$, it is a direct consequence of the pure rotational velocity ω around the CoR. Since the friction is assumed independent of the speed we can represent the velocity by its unit vector $\hat{\boldsymbol{v}}$. According to the definition of the CoR (Lynch and Park 2017), the sliding velocity is orthogonal to $\boldsymbol{d}$, namely,

$$\hat{\boldsymbol{v}}(x,y) = \frac{\boldsymbol{\omega} \times \boldsymbol{d}}{\|\boldsymbol{\omega} \times \boldsymbol{d}\|} = \frac{\begin{bmatrix}-d_y & d_x & 0\end{bmatrix}^T}{\|\boldsymbol{d}(x,y)\|}\,\mathrm{sign}(\omega) \tag{2.3}$$

where

$$\boldsymbol{\omega} = \begin{bmatrix} 0 & 0 & \omega \end{bmatrix}^T. \tag{2.4}$$

Note that sign(ω) is needed to take into account also the direction of rotation.

It is possible to apply the one-dimensional Coulomb friction law at each infinitesimal contact area and then integrate over the whole contact surface. The normal elementary force at dA is given by

$$\mathrm{d}f_n = p(x, y)\mathrm{d}A, \tag{2.5}$$

the corresponding local friction force is opposed to the velocity, i.e.,

$$\mathrm{d}\boldsymbol{f}_{tLS} = -\mu(x, y)\mathrm{d}f_n\hat{\boldsymbol{v}}(x, y) = -\mu(x, y)p(x, y)\hat{\boldsymbol{v}}(x, y)\mathrm{d}A. \tag{2.6}$$

Finally, by integrating over the contact area it is possible to compute the total friction force

$$\boldsymbol{f}_{tLS} = \begin{bmatrix} f_{xLS} \\ f_{yLS} \\ 0 \end{bmatrix} = -\int_{\mathcal{C}} \mu(x, y)p(x, y)\hat{\boldsymbol{v}}(x, y)\,\mathrm{d}A. \tag{2.7}$$

$\mathrm{d}\boldsymbol{f}_{tLS}$ generates a friction torque orthogonal to the sliding plane. The elementary torque is given by the cross product

$$\mathrm{d}\boldsymbol{\tau}_{nLS} = \begin{bmatrix} 0 \\ 0 \\ \mathrm{d}\tau_{nLS} \end{bmatrix} = \begin{bmatrix} x \\ y \\ 0 \end{bmatrix} \times \mathrm{d}\boldsymbol{f}_{tLS} \tag{2.8}$$

which can be integrated yielding the total friction moment

$$\boldsymbol{\tau}_{nLS} = \begin{bmatrix} 0 \\ 0 \\ \tau_{nLS} \end{bmatrix} = -\int_{\mathcal{C}} \left(\begin{bmatrix} x & y & 0 \end{bmatrix}^T \times \hat{\boldsymbol{v}}(x, y)\right) \mu(x, y)p(x, y)\,\mathrm{d}A. \tag{2.9}$$

Equations (2.7) and (2.9) represent the mapping between any instantaneous motion (described by the CoR position) and the dry friction force and torque. The pressure distribution $p(x, y)$ and the friction coefficient $\mu(x, y)$ are the parameters of the soft contact model..

The Limit Surface can be built by computing these integrals for various CoR positions.

Note that the CoR and the integrals (2.7) – (2.9) make sense only for non-zero velocity.

Figure 2.3 shows an example of Limit Surface, it is represented in the wrench space (f_x, f_y, τ_n). If the external wrench is inside this surface, the

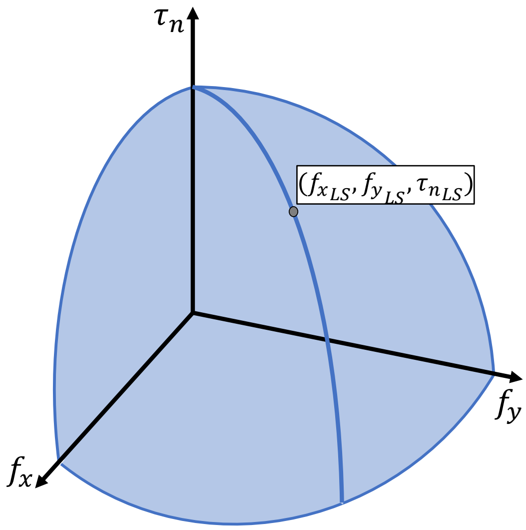

Figure 2.3: An example of Limit Surface in the wrench space (f_x, f_y, τ_n)

friction wrench balances the external one and no slippage takes place; if the external wrench is exactly on the Limit Surface, the forces are balanced as well, but, the motion is a constant velocity one; finally, if the external wrench is outside the surface, the forces are not balanced and the slider accelerates.

Unfortunately, except for very special cases, explicit solutions to integrals (2.7) and (2.9) do not exist. The next section will cover the case of axisymmetric pressure distribution, it is a quite general case that covers contacts between soft fingertips and rigid bodies.

2.2 Axisymmetric Pressure Distribution

Common scenarios in robotics involve parallel grippers or complex hands that manipulate rigid objects with fingertips typically rounded and soft. In such cases, the pressure distribution is well approximated with an axisymmetric one as shown by Xydas and Kao (1999). A further nonrestrictive assumption is to consider the friction coefficient $\mu(x, y)$ axisymmetric as well (in practice, later on, it will be considered uniform over the contact area). This thesis will consider this type of contact.

Without loss of generality, it is possible to choose the x-axis of the Cartesian reference frame such that it passes through the CoR with the origin located at the centroid of the contact area. In this way the coordinates of the CoR position become

$$\boldsymbol{p}_c = \begin{bmatrix} c & 0 & 0 \end{bmatrix}^T \tag{2.10}$$

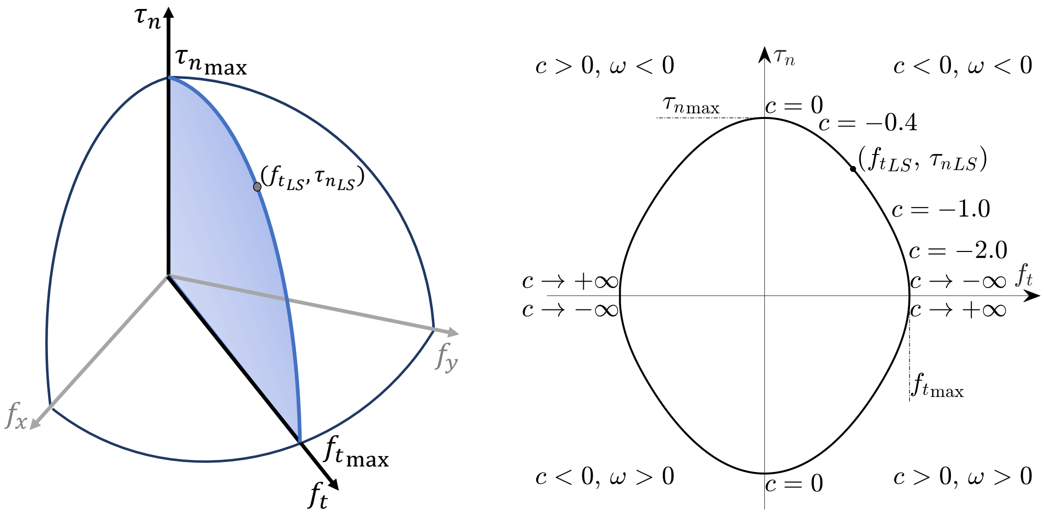

(a) View in the 3D space $(f_x,\ f_y,\ \tau_n)$ (b) View in the 2D space $(f_t,\ \tau_n)$

Figure 2.4: Axisymmetric Limit Surface

where c is the x coordinate of the CoR position.

By solving the integrals (2.7) – (2.9) in this particular case it is possible to show that the friction force f_{xLS} in the x direction is always zero. This means that, for this particular choice of the reference frame, the translational friction force $\boldsymbol{f}_{tLS}$ lies on the y-axis. So, it is possible to consider f_t as a scalar and describe the Limit Surface in the 2D space $(f_t,\ \tau_n)$.

The pressure distribution $p(x, y)$ is considered axisymmetric, then in polar coordinates $(r,\ \theta)$, it depends only on the r coordinate. Thus, the pressure distribution can be written as $p(r)$. The same holds for the friction coefficient $\mu(r)$. Moreover, the axisymmetric nature of the distribution implies that the contact area is a circle with radius ρ.

In view of these considerations, the integrals (2.7) and (2.9), become

$$f_{tLS} = -\operatorname{sign}(\omega) \int_0^{2\pi} \int_0^{\rho} \mu(r) p(r) \frac{(r\cos\theta - c)r}{\sqrt{r^2 + c^2 - 2cr\cos\theta}} \, \mathrm{d}r \mathrm{d}\theta \tag{2.11}$$

$$\tau_{nLS} = -\operatorname{sign}(\omega) \int_0^{2\pi} \int_0^{\rho} \mu(r) p(r) \frac{(r - c\cos\theta)r^2}{\sqrt{r^2 + c^2 - 2cr\cos\theta}} \, \mathrm{d}r \mathrm{d}\theta. \tag{2.12}$$

Figure 2.4 summarises the situation in the wrench space. Figure 2.4a represents a generic axisymmetric Limit Surface in the 3D space $(f_x,\ f_y,\ \tau_n)$. The axial symmetry implies that it is possible to use any radial cross-section to describe the actual 3D surface. The direction of the tangential force $\boldsymbol{f}_t$, orthogonal to the CoR position, is highlighted in the figure. The directions of f_t and τ_n define a radial cross section, i.e., the 2D space in which f_{tLS} and τ_{nLS} are defined. Obviously, by changing the CoR position, the orientation of $\boldsymbol{f}_t$ may change, but equations (2.11)–(2.12) remain the same and they depend only on the position c of the CoR. Figure 2.4b shows the situation in the $(f_t,\ \tau_n)$ plane, obtained by solving (2.11) – (2.12) using a uniform pressure distribution.

Figure 2.4b shows that the Limit Surface has a shape similar to an ellipse, called *limit curve* (nevertheless, we will still call it *Limit Surface*). The 2D Limit Surface shows the coupling between the friction force and torque during sliding, i.e., the maximum friction force f_{tLS} decreases as the applied torque increases and vice versa. Each quadrant corresponds to a different sign of c and ω as indicated in Fig. 2.4b.

Each point on the Limit Surface corresponds to a CoR position c as highlighted in Fig. 2.4b. It is possible to invert this relation: given the wrench, calculate the CoR position c. In Section 2.4 and Section 2.5.2 we propose a novel approach to estimate the CoR position from the measure of the friction wrench obtained by a force/tactile sensor. The estimated CoR position will be used to build a dynamic model for the Planar Slider in Chapter 3.

Note that, when c goes towards infinity, the motion becomes a pure translation and it is possible to recover the classical Coulomb friction law, the corresponding torque is zero and the corresponding tangential force is the maximum possible value of the tangential friction force, let call it $f_{t\max}$. This derives from equations (2.11) – (2.12) by computing the limits for $c \to \infty$

$$f_{t\max} = \left| \lim_{c\to\infty} f_{tLS} \right| = \int_0^{2\pi}\int_0^{\rho} \mu(r)p(r)r\,\mathrm{d}r\mathrm{d}\theta \tag{2.13}$$

$$\begin{aligned}\lim_{c\to\pm\infty} \tau_{nLS} &= \pm\,\mathrm{sign}(\omega)\int_0^{2\pi}\int_0^{\rho} \mu(r)p(r)r^2\cos\theta\,\mathrm{d}r\mathrm{d}\theta \\ &= \pm\,\mathrm{sign}(\omega)\int_0^{\rho}\mu(r)p(r)r^2\,\mathrm{d}r\int_0^{2\pi}\cos\theta\,\mathrm{d}\theta \\ &= 0.\end{aligned} \tag{2.14}$$

In many cases the friction coefficient is considered uniform over the contact area, in such case $f_{t\max}$ becomes

$$f_{t\max} = \mu \int_0^{2\pi} \int_0^{\rho} p(r) r \,\mathrm{d}r\mathrm{d}\theta = \mu f_n, \tag{2.15}$$

which is the well-known maximum dry Coulomb friction.

On the other hand, when the motion is a pure rotation, the CoR position coincides with the Center of Pressure (i.e., $c = 0$). f_{tLS} becomes zero and the corresponding torque is the maximum possible value of torsional friction torque, let call it $\tau_{n\max}$. The zero translational force can be shown by solving (2.11) for $c = 0$, note that this ends up to integrate the $\cos(\cdot)$ function over a period, hence

$$\lim_{c \to 0} f_{tLS} = 0. \tag{2.16}$$

As equation (2.12) for $c = 0$ depends on the particular pressure distribution, $\tau_{n\max}$ can not be written in a closed form even assuming a uniform friction coefficient μ. Its expression is

$$\begin{aligned} \tau_{n\max} = \left| \lim_{c \to 0} \tau_{nLS} \right| &= \int_0^{2\pi} \int_0^{\rho} \mu(r) p(r) r^2 \,\mathrm{d}r\mathrm{d}\theta \\ &= 2\pi \int_0^{\rho} \mu(r) p(r) r^2 \,\mathrm{d}r, \end{aligned} \tag{2.17}$$

therefore, it is essential to consider a pressure distribution model.

2.2.1 From Hertzian to Uniform Pressure Distributions

Hertzian Pressure Distribution

Contact mechanics is not a recent research field. Hertz (1882) studied the interaction between two linear elastic materials, in particular, he studied the size of the contact area as a function of the applied normal force. Hertz derived that the radius of the contact area is proportional to the normal force raised to the power of 1/3

$$\rho \propto {f_n}^{1/3}. \tag{2.18}$$

The pressure distribution associated with the Hertzian contact is (Howe and Cutkosky 1996)

$$p_H(r) = \begin{cases} \frac{3}{2}\frac{f_n}{\pi\rho^2}\sqrt{1-\left(\frac{r}{\rho}\right)}, & \text{if } 0 \leq r \leq \rho \\ 0, & \text{if } r > \rho \end{cases}. \tag{2.19}$$

By using the Hertzian pressure distribution, it is possible to compute $\tau_{n\max}$ in (2.17) as

$$\tau_{n\max} = \frac{3\pi}{16}\mu f_n \rho \propto f_n^{4/3}. \tag{2.20}$$

Uniform Pressure Distribution

A substantially different pressure distribution is the uniform one. It is still axisymmetric, so with a circular contact area, but the pressure is the same over the contact. It can be written as

$$p_U(r) = \begin{cases} \frac{f_n}{\pi\rho^2}, & \text{if } 0 \leq r \leq \rho \\ 0, & \text{if } r > \rho \end{cases}. \tag{2.21}$$

Now, by using the pressure distribution p_U, $\tau_{n\max}$ in (2.17) becomes

$$\tau_{n\max} = \frac{3}{2}\mu f_n \rho. \tag{2.22}$$

A General Axisymmetric Pressure Distribution Class

The set of pressure distributions considered in this thesis is a more general one, it contains Hertzian, uniform, and other distributions in between. It is described by Xydas and Kao (1999) and has the following expression

$$p(r) = \begin{cases} \xi_k \frac{f_n}{\pi\rho^2}\left(1-\left(\frac{r}{\rho}\right)^k\right)^{1/k}, & \text{if } 0 \leq r \leq \rho \\ 0, & \text{if } r > \rho \end{cases} \tag{2.23}$$

with

$$\rho = \delta f_n^\gamma \tag{2.24}$$

and

$$\xi_k = \frac{3}{2}\frac{k\Gamma(3/k)}{\Gamma(1/k)\Gamma(2/k)}, \tag{2.25}$$

being δ and γ coefficients of the radius model and $\Gamma(\cdot)$ the Gamma function. The coefficient k discriminates the shape of the pressure distribution. Note that, when $k = 2$, this distribution corresponds to the Hertzian one, while when $k \to \infty$ it becomes a uniform pressure distribution.

Xydas and Kao (1999) show that this pressure distribution is suitable for anthropomorphic rounded soft fingers. In particular, the radius of the contact area (2.24) is proportional to the normal force raised to a power γ, which ranges from 0 to 1/3. The lower bound corresponds to the *ideal soft finger*, while $\gamma = 1/3$ corresponds to the linear elastic Hertzian contact model.

Adopting the pressure distribution (2.23) the maximum torsional torque (2.17) becomes

$$\tau_{n\max} = 2\mu\xi_k f_n \rho \int_0^1 \mu(\tilde{r})\tilde{r}^2 \left(1 - \tilde{r}^k\right)^{1/k} \mathrm{d}\tilde{r} \tag{2.26}$$

where $\tilde{r} = r/\rho$ is the integration variable normalized with respect to the radius of the contact area. By considering μ uniform over the contact area, the remaining integral does not depend on any variable of the contact mechanics, it is just a sequence of the variable k, let call this sequence ν_k. By means of a symbolic calculation tool, an explicit solution has been found in the form of the Beta function, i.e.,

$$\nu_k = \int_0^1 \tilde{r}^2 \left(1 - \tilde{r}^k\right)^{1/k} \mathrm{d}\tilde{r} = \frac{1}{k} B(3/k, 1 + 1/k). \tag{2.27}$$

This brings us to an explicit formulation for $\tau_{n\max}$

$$\tau_{n\max} = 2\mu\xi_k\nu_k f_n \rho = 2\mu\xi_k\nu_k\delta f_n^{\gamma+1}. \tag{2.28}$$

The more general pressure distribution considered in this section, and the corresponding Limit Surface model, will be adopted for the rest of the thesis.

As a remark, the parameters of the contact model are only μ, δ, γ, and k. Note that, in case of a rigid object in contact with a soft fingertip, the parameters of the pressure distribution (δ, γ, and k) are properties of the soft fingertip while μ depends on the interaction of the object and the fingertip. Common robotic applications involve a single hand/gripper that grasps multiple objects, thus the pressure distribution parameters can be estimated only once and the only parameter to be estimated for each object is μ. Appendix B will show the procedure to estimate the pressure distribution parameters for the sensorized fingertips used in this thesis as well as the friction coefficient.

This new formulation will be used in the following section to define the normalized space.

2.3 Normalized Limit Surface

The limit surface described so far depends on the contact parameters and the normal force. Contact parameters can be estimated just once, but the normal force can be time-varying. It is time-consuming to resolve the Limit Surface integrals for every value of the parameters and normal force. To simplify the analysis, it is convenient to normalize the Limit Surface with respect to the maximum values of the tangential friction force and torque, i.e., $f_{t\max}$ and $\tau_{n\max}$ respectively. In this thesis, the tilde symbol $\tilde{\cdot}$ indicates a normalized variable.

The first step is to normalize the CoR position c with respect to the radius of the contact area ρ

$$\tilde{c} = \frac{c}{\rho}. \tag{2.29}$$

Adopting the axisymmetric pressure distribution (2.23) – (2.24) with a uniform friction coefficient μ and changing the integration variable r with its normalized version $\tilde{r} = r/\rho$, the Limit Surface equations (2.11) – (2.12) can be written as

$$f_{tLS} = -\operatorname{sign}(\omega)\frac{\mu\xi_k f_n}{\pi}\int_0^{2\pi}\int_0^1 \frac{\tilde{r}(\tilde{r}\cos\theta - \tilde{c})(1-\tilde{r}^k)^{1/k}}{\sqrt{\tilde{r}^2+\tilde{c}^2-2\tilde{c}\tilde{r}\cos\theta}}\,\mathrm{d}\tilde{r}\mathrm{d}\theta \tag{2.30}$$

$$\tau_{nLS} = -\operatorname{sign}(\omega)\frac{\mu\xi_k f_n \rho}{\pi}\int_0^{2\pi}\int_0^1 \frac{\tilde{r}^2(\tilde{r} - \tilde{c}\cos\theta)(1-\tilde{r}^k)^{1/k}}{\sqrt{\tilde{r}^2+\tilde{c}^2-2\tilde{c}\tilde{r}\cos\theta}}\,\mathrm{d}\tilde{r}\mathrm{d}\theta. \tag{2.31}$$

The second step is to define the normalized plane $(\tilde{f}_t,\, \tilde{\tau}_n)$ as

$$\tilde{f}_t = f_t/f_{t\max}, \qquad \tilde{\tau}_n = \tau_n/\tau_{n\max}. \tag{2.32}$$

Finally, it is possible to obtain the *Normalized Limit Surface* (NLS) by using (2.32), i.e.,

$$\tilde{f}_{tLS} = -\operatorname{sign}(\omega)\frac{\xi_k}{\pi}\int_0^{2\pi}\int_0^1 \frac{\tilde{r}(\tilde{r}\cos\theta - \tilde{c})(1-\tilde{r}^k)^{1/k}}{\sqrt{\tilde{r}^2+\tilde{c}^2-2\tilde{c}\tilde{r}\cos\theta}}\,\mathrm{d}\tilde{r}\mathrm{d}\theta \tag{2.33}$$

$$\tilde{\tau}_{nLS} = -\operatorname{sign}(\omega)\frac{1}{2\pi\nu_k}\int_0^{2\pi}\int_0^1 \frac{\tilde{r}^2(\tilde{r} - \tilde{c}\cos\theta)(1-\tilde{r}^k)^{1/k}}{\sqrt{\tilde{r}^2+\tilde{c}^2-2\tilde{c}\tilde{r}\cos\theta}}\,\mathrm{d}\tilde{r}\mathrm{d}\theta. \tag{2.34}$$

Note that the points of the NLS $\tilde{f}_{tLS}$ and $\tilde{\tau}_{nLS}$ are functions of the CoR position $\tilde{c}$ and the sign of the rotational velocity about the CoR ω. Moreover, the NLS does not depend on any of the contact parameters except for k.

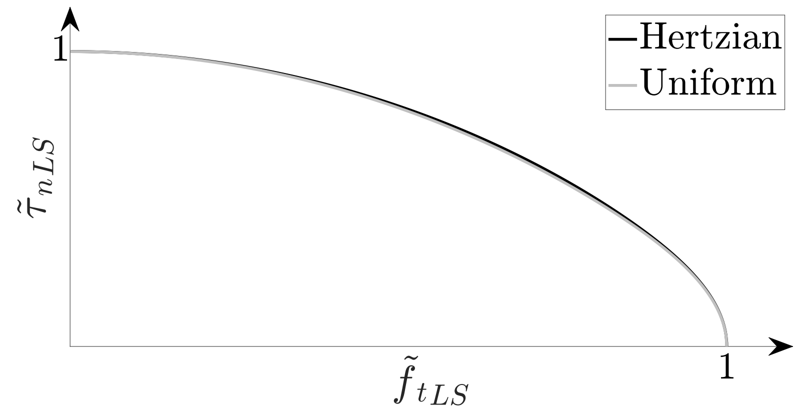

Figure 2.5: The Normalized Limit Surface in the Hertzian and Uniform cases.

Figure 2.5 shows the Normalized Limit Surface for two significantly different values of k, i.e., $k = 2$, which represents an Hertzian contact, and $k \to \infty$, which corresponds to the uniform pressure distribution case. The remaining cases are contained between the two limit curves in the plot. It is evident that the NLS weakly depends on the parameter k, so its estimation is not crucial for the description in the Normalized Plane.

Equations (2.33) – (2.34) can be further simplified by introducing the following functions

$$\tilde{f}^*_{t\,LS}(\tilde{c}) = \frac{\xi_k}{\pi} \int_0^{2\pi} \int_0^1 \frac{\tilde{r}(\tilde{r}\cos\theta - \tilde{c})(1-\tilde{r}^k)^{1/k}}{\sqrt{\tilde{r}^2 + \tilde{c}^2 - 2\tilde{c}\tilde{r}\cos\theta}} \, \mathrm{d}\tilde{r}\mathrm{d}\theta \tag{2.35}$$

$$\tilde{\tau}^*_{nLS}(\tilde{c}) = \frac{1}{2\pi\nu_k} \int_0^{2\pi} \int_0^1 \frac{\tilde{r}^2(\tilde{r} - \tilde{c}\cos\theta)(1-\tilde{r}^k)^{1/k}}{\sqrt{\tilde{r}^2 + \tilde{c}^2 - 2\tilde{c}\tilde{r}\cos\theta}} \, \mathrm{d}\tilde{r}\mathrm{d}\theta. \tag{2.36}$$

These functions, given k, can be numerically computed for various values of $\tilde{c}$ only once and then they can be approximated by resorting to any universal approximator. Figure 2.6 shows $\tilde{f}^*_{t\,LS}(\tilde{c})$ and $\tilde{\tau}^*_{nLS}(\tilde{c})$ for $k = 0$ and $k \to \infty$, it is not surprising that, once again, the plots weakly depend on the value of k. Taking into account their shapes, it is convenient to use a superposition of sigmoidal functions to approximate $\tilde{f}^*_{t\,LS}(\tilde{c})$ and of Gaussian ones to approximate $\tilde{\tau}^*_{nLS}(\tilde{c})$, which are both radial basis functions and thus can be used as

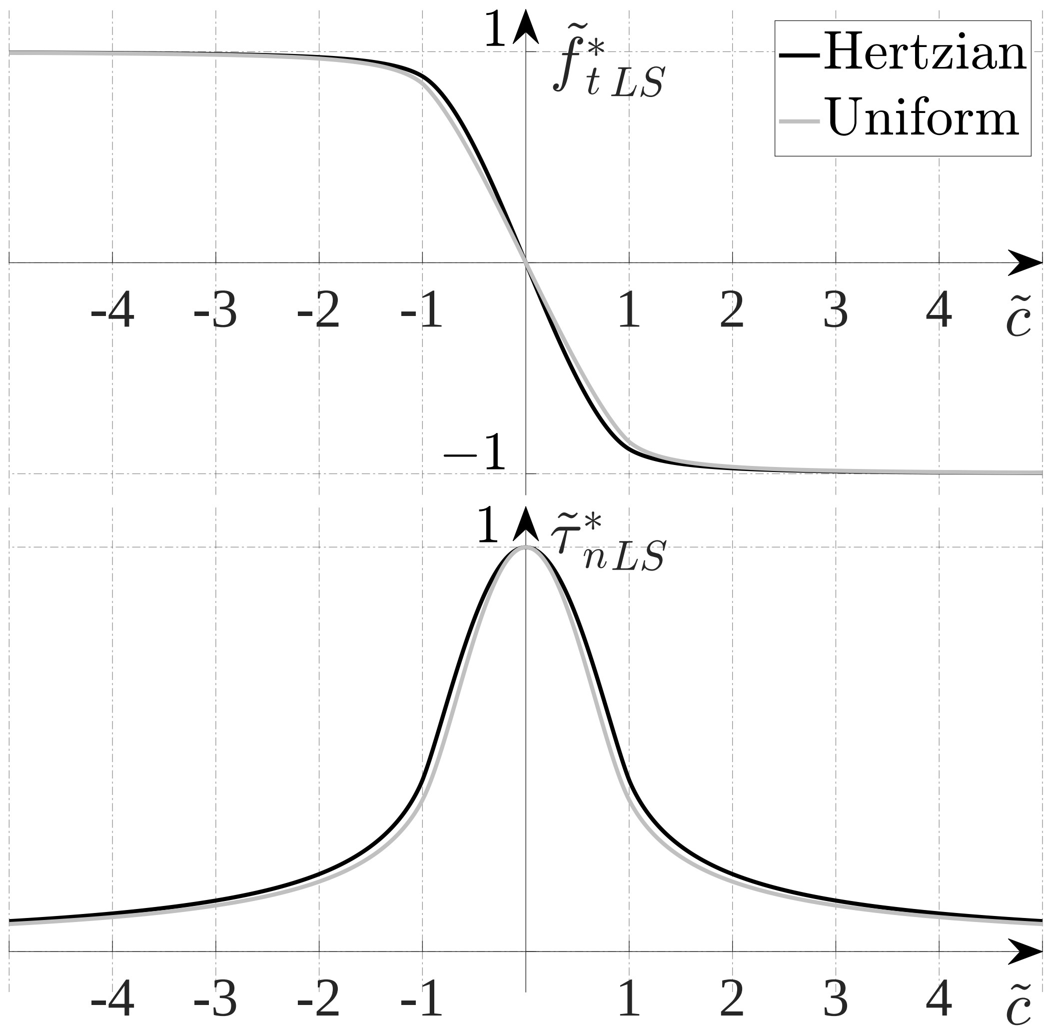

Figure 2.6: Typical graphs (uniform and Hertzian pressure distributions) of $\tilde{f}^*_{t\,LS}$ and $\tilde{\tau}^*_{nLS}$ as functions of $\tilde{c}$.

universal approximators (Hornik 1991; Moody and Darken 1988), i.e.,

$$\tilde{f}^*_{t\,LS}(\tilde{c}) = \sum_{i=1}^{n} w_{f_i} \left(\frac{2}{1 + e^{a_i(\tilde{c} - m_{f_i})}} - 1 \right) \tag{2.37}$$

$$\tilde{\tau}^*_{nLS}(\tilde{c}) = \sum_{i=1}^{n} w_{\tau_i} e^{-\frac{(\tilde{c} - m_{\tau_i})^2}{2 s_i^2}} \tag{2.38}$$

where w_{f_i}, a_i, m_{f_i}, w_{τ_i}, m_{τ_i}, s_i and n are parameters of the approximators (Cavallo et al. 2020). Nevertheless, in the rest of the thesis, the functions $\tilde{f}^*_{t\,LS}(\tilde{c})$ and $\tilde{\tau}^*_{nLS}(\tilde{c})$ will be considered known, which means that they can be numerically computed from (2.35) – (2.36) or approximated by any approximator.

By using the formulation of the LS concept described so far, the parametric equations of the Normalized Limit Surface in function of $\tilde{c}$ and $\mathrm{sign}(\omega)$ can be simply rewritten as

$$\tilde{f}_{tLS}(\tilde{c}, \omega) = -\,\mathrm{sign}(\omega) \tilde{f}^*_{t\,LS}(\tilde{c}) \tag{2.39}$$

$$\tilde{\tau}_{nLS}(\tilde{c}, \omega) = -\,\mathrm{sign}(\omega) \tilde{\tau}^*_{nLS}(\tilde{c}) \tag{2.40}$$

An important observation is that

$$\mathrm{sign}(\tilde{f}^*_{t\,LS}) = -\,\mathrm{sign}(\tilde{c}) \tag{2.41}$$

$$\tilde{\tau}^*_{nLS}(\tilde{c}) > 0 \quad \forall \tilde{c}, \tag{2.42}$$

as shown in Fig. 2.6. This observation and equations (2.39) – (2.40) imply that

$$\mathrm{sign}(\tilde{\tau}_{nLS}) = \mathrm{sign}(\tau_{nLS}) = -\,\mathrm{sign}(\omega) \tag{2.43}$$

$$\mathrm{sign}(\tilde{f}_{tLS})\,\mathrm{sign}(\tilde{\tau}_{nLS}) = \mathrm{sign}(f_{tLS})\,\mathrm{sign}(\tau_{nLS}) = -\,\mathrm{sign}(\tilde{c}). \tag{2.44}$$

Now we have a powerful formulation of the static friction problem in the normalized space, which does not depend on any parameter (except the weakly dependence on k). It is possible to normalize the force and torque by using equation (2.32), make any needed computation in the normalized space, and then denormalize the result. The relevant friction parameters enter only in the normalization/denormalization phase. This framework will be used to build a method to solve the *inverse LS problem*, i.e., given a measured friction wrench, estimate the instantaneous motion in terms of CoR location and instantaneous velocity direction.

2.4 The Inverse LS Problem

The Limit Surface is typically used to solve the *forward LS problem* problem, i.e., given the instantaneous motion (CoR position and sign of ω) compute the friction force and torque. In this thesis, the LS modeling for axisymmetric pressure distribution is exploited to solve the *inverse LS problem* given a measure of the friction force f_{tf} and torque τ_{nf}. This is important for the dynamic sliding modeling and grasp control in Chapter 3. In fact, this thesis will present a model-based grasp controller that regulates the grasp force based on the measurement of friction forces and torques. Thus, it necessary to know the instantaneous motion given the friction measures.

First of all, the Center of Rotation is defined only when the object is actually sliding, i.e., when $\omega \neq 0$. Thus, trying to estimate the CoR position when $\omega = 0$ does not make sense. The easiest way to solve the inverse problem is to consider that, during the sliding, the measured friction wrench is equal to the maximum static friction wrench that is represented by a point on the limit surface. This is true both for the normalized and not normalized variables, in particular

$$\omega \neq 0 \implies (\tilde{f}_{tf},\, \tilde{\tau}_{nf}) = (\tilde{f}_{tLS},\, \tilde{\tau}_{nLS}). \tag{2.45}$$

Recalling the normalization equation (2.32) and equations (2.39) – (2.40), the condition above becomes

$$\left(\frac{f_{tf}}{\mu f_n},\, \frac{\tau_{nf}}{2\mu \xi_k \nu_k \delta {f_n}^{\gamma+1}}\right) = \Big(-\operatorname{sign}(\omega)\tilde{f}^*_{tLS}(\tilde{c}),\, -\operatorname{sign}(\omega)\tilde{\tau}^*_{nLS}(\tilde{c})\Big)\,. \tag{2.46}$$

The equivalence must be true for both components. By studying the sign of the second component and by using the relation (2.43) it follows that

$$-\operatorname{sign}(\omega) = \operatorname{sign}(\tau_{nf}). \tag{2.47}$$

Finally, the equation of the first component can be rearranged as

$$\frac{f_{tf}}{\mu f_n}\operatorname{sign}(\tau_{nf}) = \tilde{f}^*_{tLS}(\tilde{c}) \tag{2.48}$$

that is a nonlinear equation in the unknown $\tilde{c}$ that can be solved both by inverting the function $\tilde{f}^*_{tLS}(\tilde{c})$ or by using any numerical algorithm such as the Newton method.

This algorithm can be used to estimate the normalized CoR position $\tilde{c}$ by using only the measure of the wrench at the contact area f_{tf}, τ_{nf} and f_n. But this approach has a drawback, it can be used only if the measured friction

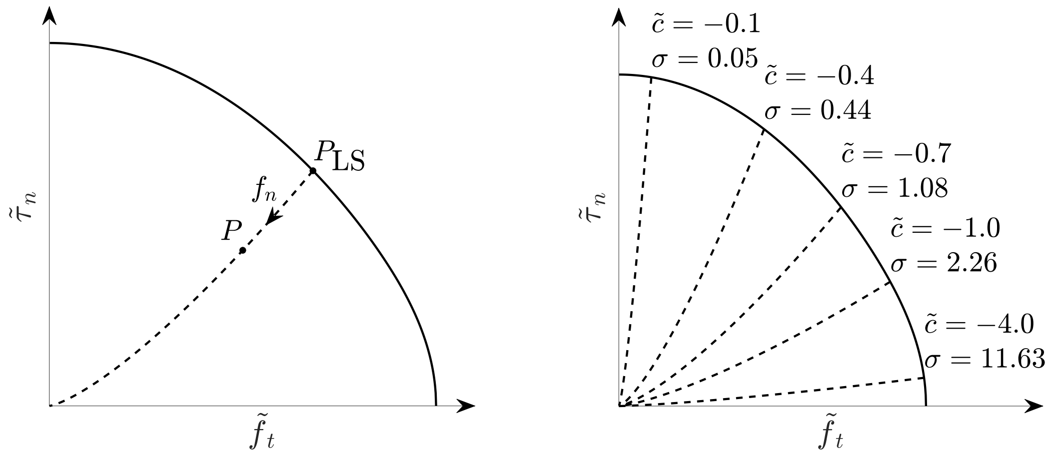

(a) A σ-curve.

(b) Various σ-curve and their relation with $\tilde{c}$.

Figure 2.7: σ-curves in the normalized space

wrench is exactly on the Limit Surface. Neglecting possible measurement errors, this is true only if there is no viscous friction and the body is actually sliding. In the case of viscous friction the actual friction wrench could be outside the LS, this issue will be treated in Section 2.5.2. Instead, if the body is not sliding the friction wrench is inside the LS and the CoR is not defined at all.

The planar slider dynamic model proposed by this thesis will be presented in Section 3.2. It describes the motion as a 1-DOF system that can rotate about the CoR axis. Thus, it needs that the CoR position is defined also when the velocity is zero.

This issue is solved by introducing the *Virtual Center of Rotation*.

Definition 2.1 (Virtual Center of Rotation)**.** If the sliding velocity is zero then the Virtual Center of Rotation (VCoR) is the CoR which would result if the normal force were small enough to allow the starting of the sliding.

The definition of VCoR extends the definition of CoR in case of zero velocity. To simplify the notation, in the rest of this thesis the acronym CoR will be used to indicate the VCoR or CoR, indistinctly.

Figure 2.7 helps to visualize this concept in the normalized space. With reference to Fig. 2.7a, the point $P = (\tilde{f}_{tf}, \tilde{\tau}_{nf})$ indicates the location of the actual friction wrench on the normalized space, the dashed curve represents the motion of the point P on the plane when f_n varies but not f_{tf} and τ_{nf}. An arrow indicates the growing direction of f_n. Note that the position of

P depends on f_n because of the normalization formula (2.32). As expected, when f_n decreases, i.e., when the gripper reduces the grasp force, the point P goes towards the NLS, otherwise, it goes towards the origin. Let call the depicted line σ-curve. In the non-normalized plane, this situation would be the opposite one, i.e., the point P would be fixed, and the Limit Surface would grow as f_n grows, i.e., when the gripper increases the grasping force. The σ-curve intercepts the NLS in the point $P_{LS} = (\tilde{f}_{tLS}, \tilde{\tau}_{nLS})$ that corresponds to a unique value of the normalized CoR position $\tilde{c}$. Such value represents the VCoR associated to a zero velocity and the actual friction wrench (f_{tf}, τ_{nf}).

Figure 2.7b shows the σ-curve for various locations of the actual friction wrench. From the plot, it is clear that the correspondence between the σ-curve and the VCoR is unique, each σ-curve corresponds to one value of $\tilde{c}$.

Equation (2.32) can be seen as a parametric expression of the σ-curve from which it is easy to derive its explicit version

$$\tilde{\tau}_n = \frac{1}{\sigma}\left|\tilde{f}_t\right|^{\gamma+1} \quad \text{with } \tilde{f}_t \,:\, \operatorname{sign}(\tilde{f}_t) = \operatorname{sign}(f_{tf}) \tag{2.49}$$

where

$$\sigma = \frac{2\xi_k \nu_k \delta}{\mu^\gamma}\frac{\left|f_{tf}\right|^{\gamma+1}}{\tau_{nf}}. \tag{2.50}$$

As a remark, $\operatorname{sign}(\tilde{f}_t) = \operatorname{sign}(f_{tf})$ is the condition that must be verified to ensure that the term $(\tilde{f}_t/f_{tf})^{1+\gamma}$ that has a non-integer exponent is well defined. Note that the σ-curve depends on all contact parameters and on the actual friction wrench (f_{tf}, τ_{nf}) but not on the normal force f_n. This will be crucial in the grasp control of Chapter 3 because it implies that it is possible to compute the CoR using only the friction forces measured by the tactile sensors and not the control input f_n.

Moreover, (2.49) implies that

$$\operatorname{sign}(\tilde{\tau}_n) = \operatorname{sign}(\sigma) \quad \forall \tilde{\tau}_n \text{ on the } \sigma\text{-curve} \tag{2.51}$$

Now it is possible to infer the VCoR. Equation (2.49) holds for all the points on the σ-curve, in particular, it holds also for the point P_{LS} which is the intersection between the σ-curve and the Limit Surface. This implies that

$$\sigma = \frac{\left|\tilde{f}^*_{tLS}(\tilde{c})\right|^{\gamma+1}}{-\operatorname{sign}(\omega)\tilde{\tau}^*_{nLS}(\tilde{c})} \quad \text{with } -\operatorname{sign}(\omega)\operatorname{sign}(\tilde{f}^*_{tLS}(\tilde{c})) = \operatorname{sign}(f_{tf}). \tag{2.52}$$

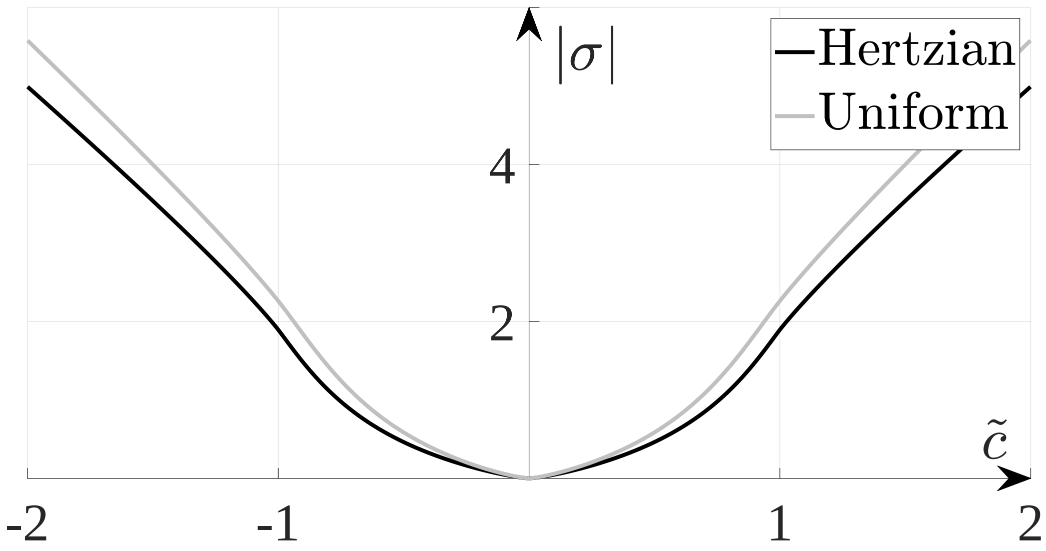

Figure 2.8: Absolute value of σ as a function of $\tilde{c}$. The plot shows the function for the two limit values of k, i.e., $k = 0$ (Hertzian) and $k \to \infty$ (Uniform).

Also (2.51) holds for P_{LS}, thus, recalling (2.41) and (2.43),

$$|\sigma| = \frac{\left|\tilde{f}^*_{t\,LS}(\tilde{c})\right|^{\gamma+1}}{\tilde{\tau}^*_{nLS}(\tilde{c})} \quad \text{with } \operatorname{sign}(\tilde{c}) = -\operatorname{sign}(f_{tf})\operatorname{sign}(\tau_{nf}). \tag{2.53}$$

The left side of the equation depends only on the contact parameters and on the actual friction wrench, but not on the normal force; the right side is a nonlinear function of the variable $\tilde{c}$. The inverse of (2.53) allows to compute the VCoR coordinate $\tilde{c}$. The function $|\sigma(\tilde{c})|$ is shown in Figure 2.8, note that it is invertible only if the domain is limited to the left or right plane, i.e., if the constraint $\operatorname{sign}(\tilde{c}) = -\operatorname{sign}(f_{tf})\operatorname{sign}(\tau_{nf})$ is satisfied.

There is a singular situation when $\tau_{nf} = 0$, in fact, this implies that σ in (2.50) is not well defined. In such a case, the σ-curve coincides with the positive or negative $\tilde{f}_t$-axis if f_{tf} is positive or negative, respectively. But, this situation is trivial, it coincides with the pure translational motion. This means that the VCoR is located at infinity, and, to have a finite translational velocity, the rotational velocity must be infinitesimal. In particular, there are two possible equivalent solutions: $\omega \to 0^-$ and $c \to \pm\infty$ (the positive f_{tf} the positive c), or, $\omega \to 0^+$ and $c \to \mp\infty$ (the positive f_{tf} the negative c). Note that this situation can be easily avoided in practice by considering an arbitrary small τ_{nf} instead of the zero one, this implies that the CoR becomes very large (but not infinity) and the sign of the velocity depends on the sign of τ_{nf}.

To summarize, the *Virtual Center of Rotation* can be computed from the actual friction force f_{tf} and torque τ_{nf} by solving Equation (2.53) with its constraint. The computation can be done numerically by using any numerical methods able to find the zero of a function.

2.5 Viscous Friction

The Limit Surface can be seen as an extension to the rototranslational case of the classical Coulomb dry friction. Such a description takes into account only the direction of the slipping velocity and not its magnitude as clearly stated in the assumption 3 in Section 2.1. But the total friction depends on the velocity and it is given by the sum of the dry friction and the viscous one.

In one dimension, the Coulomb friction law (2.1), in presence of viscous friction, becomes

$$\begin{cases} |f_{tf}| \leq \mu f_n, & \text{if } v = 0 \\ f_{tf} = -\mu f_n \operatorname{sign}(v) - \beta v, & \text{if } v \neq 0 \end{cases} \tag{2.54}$$

where β is the viscous friction coefficient.

The viscous friction is important to build a dynamic model of the system because the corresponding term βv directly depends on a state variable. This section will be focused on the extension of (2.54) to the rototranslational case, studying all the implications on the Limit Surface description made so far.

With reference to the same description of Fig. 2.2, in the presence of viscous friction, the total friction force acting on the infinitesimal contact area $\mathrm{d}A$ is

$$\mathrm{d}\boldsymbol{f}_{tf} = -\mu(x, y)\mathrm{d}f_n\hat{\boldsymbol{v}}(x, y) + \mathrm{d}\boldsymbol{f}_{tv} \tag{2.55}$$

where

$$\mathrm{d}\boldsymbol{f}_{tv} = -\beta_A(x, y)\mathrm{d}A\boldsymbol{v}(x, y) \tag{2.56}$$

represents the viscous friction acting on the area $\mathrm{d}A$ and $\beta_A(x, y)$ is the viscous friction coefficient per area unit at $\mathrm{d}A$ (Shkulipa, den Otter, and Briels 2005). The corresponding torque at the origin will be

$$\mathrm{d}\boldsymbol{\tau}_{nf} = \begin{bmatrix} 0 \\ 0 \\ \mathrm{d}\tau_{nf} \end{bmatrix} = \begin{bmatrix} x \\ y \\ 0 \end{bmatrix} \times \mathrm{d}\boldsymbol{f}_{tf} \tag{2.57}$$

Note that the first term of equation (2.55) corresponds to the dry friction (2.6). Due to the linearity of the integral operator, the total friction force and torque (with $\omega \neq 0$) is

$$\boldsymbol{f}_{tf} = \boldsymbol{f}_{tLS} + \boldsymbol{f}_{tv} \tag{2.58}$$

$$\boldsymbol{\tau}_{nf} = \boldsymbol{\tau}_{nLS} + \boldsymbol{\tau}_{nv} \tag{2.59}$$

where

$$\boldsymbol{f}_{tv} = -\int_{\mathcal{C}} \beta_A(x,y)\mathrm{d}A\boldsymbol{v}(x,y) \tag{2.60}$$

$$\boldsymbol{\tau}_{nv} = \begin{bmatrix} 0 \\ 0 \\ \tau_{nv} \end{bmatrix} = \int_{\mathcal{C}} \begin{bmatrix} x & y & 0 \end{bmatrix}^T \times \mathrm{d}\boldsymbol{f}_{tv}. \tag{2.61}$$

Recalling that $\boldsymbol{v}(x,y)$ is due to the rotation about the CoR and that $\boldsymbol{d} = \boldsymbol{p} - \boldsymbol{p}_c$, the velocity has expression

$$\boldsymbol{v}(x,y) = \boldsymbol{\omega} \times \boldsymbol{d}(x,y). \tag{2.62}$$

So, integrals (2.60) – (2.61) become

$$\boldsymbol{f}_{tv} = -\int_{\mathcal{C}} \beta_A(x,y)(\boldsymbol{\omega} \times \boldsymbol{d}(x,y))\,\mathrm{d}A \tag{2.63}$$

$$\boldsymbol{\tau}_{nv} = -\int_{\mathcal{C}} \beta_A(x,y) \begin{bmatrix} x & y & 0 \end{bmatrix}^T \times (\boldsymbol{\omega} \times \boldsymbol{d}(x,y))\,\mathrm{d}A. \tag{2.64}$$

These equations represent the mapping between an instantaneous motion (described by the CoR position and the angular velocity) and the viscous friction force and torque. The only parameter is the distribution of the viscous friction coefficient per unit area β_A.

2.5.1 Axisymmetric Viscous Friction

In this thesis, similarly as already done with the function $\mu(x,y)$ in Section 2.2, $\beta_A(x,y)$ is considered uniform over the contact area. Following the same mathematical steps used for the Limit Surface, we will first derive the expression of the viscous friction when $\beta_A(x,y)$ is axisymmetric and then we will consider the uniform case as a specialization of the axisymmetric one.

Following the same steps as in Section 2.2, without loss of generality, it is possible to choose the x-axis such that it passes through the CoR with the origin located at the CoP. In this way, it is possible to describe the CoR position with the x-coordinate only, i.e., c.

As with the pressure distribution, the axisymmetric $\beta_A(x, y)$ written in polar coordinates (r, θ) depends only on the r coordinate. Thus, it can be rewritten as $\beta_A(r)$ and the integration set is a circle with radius ρ.

Moreover, it is possible to show that also the viscous friction $\boldsymbol{f}_{tv}$ lies on the y-axis. This happens because the integral of the x-component ends up integrating a sinusoidal function over a period. Thus, it is possible to consider f_{tv} as scalar and describe the viscous friction in the 2D space $(f_t,\, \tau_n)$, note that this is the same space in which the axisymmetric Limit Surface is defined.

Under these considerations, equations (2.63) and (2.64), in polar coordinates, become

$$f_{tv} = 2\pi\omega c \int_0^\rho r\beta_A(r)\,\mathrm{d}r \tag{2.65}$$

$$\tau_{nv} = -2\pi\omega \int_0^\rho r^3\beta_A(r)\,\mathrm{d}r. \tag{2.66}$$

Finally, assuming $\beta_A(r)$ uniform permits to solve the integrals in closed form

$$f_{tv} = \pi\rho^2\beta_A\omega c \tag{2.67}$$

$$\tau_{nv} = -\frac{\pi}{2}\rho^4\beta_A\omega. \tag{2.68}$$

Note that, the viscous friction depends on the contact area radius ρ which depends on f_n through equation (2.24). This means that the viscous friction force and torque are

$$f_{tv} = \pi\beta_A\delta^2 f_n^{2\gamma}\omega c \tag{2.69}$$

$$\tau_{nv} = -\frac{\pi}{2}\beta_A\delta^4 f_n^{4\gamma}\omega. \tag{2.70}$$

Because the 2D space $(f_t,\, \tau_n)$ is the same used for the Limit Surface description, the viscous friction can be represented in the same normalized space $(\tilde{f}_t,\, \tilde{\tau}_n)$ and has the following expression

$$\tilde{f}_{tv} = \frac{\pi\delta^3\beta_A f_n^{3\gamma-1}}{\mu}\omega\tilde{c} \tag{2.71}$$

$$\tilde{\tau}_{nv} = -\frac{1}{4\xi_k\nu_k}\frac{\pi\delta^3\beta_A f_n^{3\gamma-1}}{\mu}\omega. \tag{2.72}$$

Finally, the total normalized friction force and torque can be rewritten as

$$\tilde{f}_{tf} = -\operatorname{sign}(\omega)\tilde{f}^*_{t\,LS}(\tilde{c}) + \frac{\pi\delta^3\beta_A f_n^{3\gamma-1}}{\mu}\omega\tilde{c} \tag{2.73}$$

$$\tilde{\tau}_{nf} = -\operatorname{sign}(\omega)\tilde{\tau}^*_{nLS}(\tilde{c}) - \frac{1}{4\xi_k\nu_k}\frac{\pi\delta^3\beta_A f_n^{3\gamma-1}}{\mu}\omega. \tag{2.74}$$

Now it is possible to extend the dry friction case analysis made in the normalized space to the Limit Surface with viscous friction.

2.5.2 The Inverse LS Problem Generalization

With the introduction of the viscous friction, the Definition 2.1 ("*Virtual Center of Rotation*") does not change. In fact, when the sliding velocity is zero, the viscous term is zero as well and the actual friction force is the dry one. On the other hand, in the case of non-zero sliding velocity, the VCoR definition matches the classic CoR definition regardless of the value of the applied force. Nevertheless, the relation between the instantaneous motion and the friction force and torque does change.

In Section 2.4, without the viscous term, the actual friction wrench could not stay outside the Limit Surface. But now, because of the viscous term, the total friction wrench can be anywhere in the wrench space. In particular, when the sliding velocity ω is zero, the friction wrench can be only inside the Limit Surface; when $\omega \neq 0$ it can be only on or outside the Limit Surface.

When the sliding velocity is zero, the viscous term is zero and the result is exactly the same presented in Section 2.4. The only issue is that this result is valid only if the friction wrench is inside the LS, thus it is necessary to check such condition. Let define the set of the points inside the Limit Surface and its analogous in the normalized space

$$\mathcal{V}_L = \{(f_t, \tau_n) \,:\, (f_t, \tau_n) \text{ is inside the LS}\} \tag{2.75}$$

$$\tilde{\mathcal{V}}_L = \{(\tilde{f}_t, \tilde{\tau}_n) \,:\, (\tilde{f}_t, \tilde{\tau}_n) \text{ is inside the NLS}\}. \tag{2.76}$$

$\mathcal{V}_L$ is the *Limit Volume* and $\tilde{\mathcal{V}}_L$ is the *Normalized Limit Volume*. Because of the convexity of the Limit Surface, the following applies

$$(f_{tf}, \tau_{nf}) \in \mathcal{V}_L \iff \tilde{f}_{tf}^{\,2} + \tilde{\tau}_{nf}^{\,2} < \tilde{f}^{*\,2}_{t\,LS}(\tilde{c}) + \tilde{\tau}^{*\,2}_{nLS}(\tilde{c}). \tag{2.77}$$

Note that this condition depends on $\tilde{c}$ which is the unknown to be found by solving (2.53), thus, in practice, it is necessary to first solve (2.53) and then check the condition (2.77). If the condition is not satisfied then the resulting $\tilde{c}$ is not the correct one, but the point (f_{tf}, τ_{nf}) is certainly not inside the

Limit Surface, it can be only on the LS or outside it. The sliding velocity ω is non-zero and the viscous friction should be taken into account.

We have defined the σ-curve as the locus of points on which the normalized actual friction wrench can vary as the normal force varies. In Section (2.53) we ended up to the curve equation (2.49) that is implicitly defined only if $(\tilde{f}_t,\, \tilde{\tau}_n)$ is inside the Normalized LS, since it takes into account only the dry friction. The generalization of the σ-curve follows by considering that, outside the NLS the point $(\tilde{f}_{tf},\, \tilde{\tau}_{nf})$ has the parametric expression represented by equations (2.73) – (2.74), then the curve has the same parametric expression. The explicit expression can be directly found by merging the two equations, i.e.,

$$\tilde{\tau}_n = -\frac{1}{4\xi_k \nu_k}\frac{1}{\tilde{c}}(\tilde{f}_t - \tilde{f}_{tLS}(\tilde{c},\omega)) + \tilde{\tau}_{nLS}(\tilde{c},\omega). \tag{2.78}$$

Note that this is the equation of a straight line that passes through the NLS point $(\tilde{f}_{tLS}(\tilde{c},\, \omega), \tilde{\tau}_{nLS}(\tilde{c},\, \omega))$ and has angular coefficient $-\frac{1}{4\xi_k\nu_k}\frac{1}{\tilde{c}}$. Moreover it is defined only if $(\tilde{f}_t, \tilde{\tau}_n)$ is outside the NLS otherwise equations (2.73) – (2.74) are not valid.

Finally, it is possible to write the complete expression of the σ-curve in presence of viscous friction, i.e.,

$$\tilde{\tau}_n = \begin{cases} \frac{1}{\sigma}\left|\tilde{f}_t\right|^{\gamma+1} \text{ with } \tilde{f}_t \,:\, \text{sign}(\tilde{f}_t) = \text{sign}(f_{tf}), & \text{if } (\tilde{f}_t, \tilde{\tau}_n) \in \tilde{\mathcal{V}}_L \\ -\frac{1}{4\xi_k\nu_k}\frac{1}{\tilde{c}}(\tilde{f}_t - \tilde{f}_{tLS}(\tilde{c},\omega)) + \tilde{\tau}_{nLS}(\tilde{c},\omega), & \text{if } (\tilde{f}_t, \tilde{\tau}_n) \notin \tilde{\mathcal{V}}_L \end{cases} \tag{2.79}$$

Figure 2.9 shows a typical σ-curve in presence of viscous friction. Note that inside the NLS, the curve is the same as those in Fig. 2.7. On the contrary, outside the LS the curve changes shape and becomes a straight line. At the intersection with the NLS the curve is continuous. The figure reports also the growing direction of the normal force.

Now we are ready to invert the relationship between c and the friction wrench when the latter is outside the NLS (i.e., $(\tilde{f}_{tf}, \tilde{\tau}_{nf}) \notin \tilde{\mathcal{V}}_L$). This can be done by solving equations (2.73) – (2.74) in the unknown $\tilde{c}$. The obtained solution is valid only when $(\tilde{f}_{tf}, \tilde{\tau}_{nf}) \notin \tilde{\mathcal{V}}_L$, instead the solution of (2.53) is valid only when $(\tilde{f}_{tf}, \tilde{\tau}_{nf}) \in \tilde{\mathcal{V}}_L$. For writing the complete general solution of the *inverse LS problem*, it is sufficient to rearrange all the equations together,

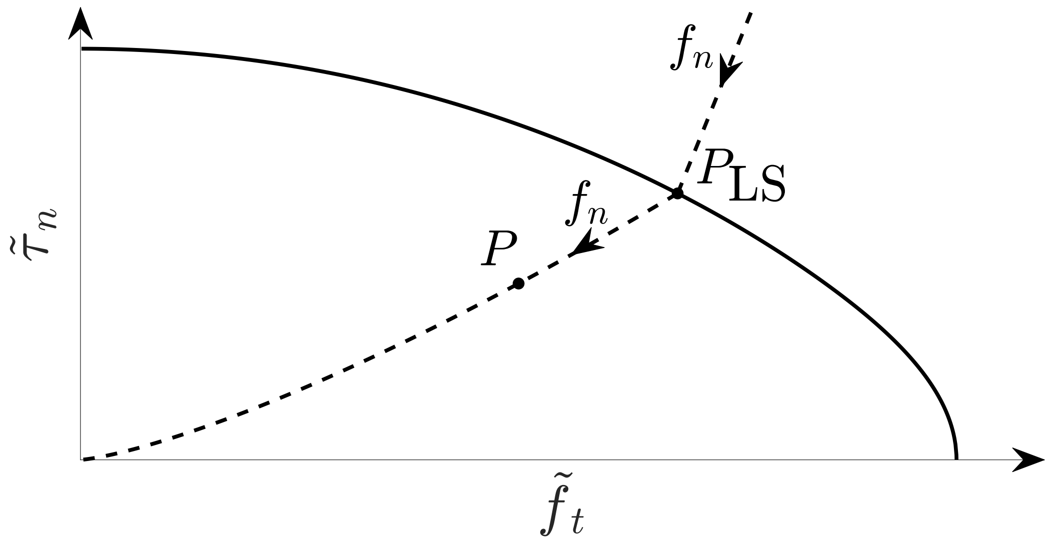

Figure 2.9: The generalization of the σ-curve in the case of viscous friction.

i.e.,

$$\begin{cases} \tilde{c}\,:\ \begin{array}{l} |\sigma| = \dfrac{\left|\tilde{f}^*_{t\,LS}(\tilde{c})\right|^{\gamma+1}}{\tilde{\tau}^*_{nLS}(\tilde{c})} \\ \text{s.t. } \operatorname{sign}(\tilde{c}) = -\operatorname{sign}(f_{tf})\operatorname{sign}(\tau_{nf}) \end{array}, & \begin{array}{l}\text{if } (\tilde{f}_{tf}, \tilde{\tau}_{nf}) \in \tilde{\mathcal{V}}_L \\ \text{and } \tau_{nf} \neq 0\end{array} \\ \tilde{c}\,:\ \begin{array}{l} \tilde{f}_{tf} = \operatorname{sign}(\tau_{nf})\tilde{f}^*_{t\,LS}(\tilde{c}) + \\ \quad -4\xi_k\nu_k\tilde{c}(\tilde{\tau}_{nf} - \operatorname{sign}(\tau_{nf})\tilde{\tau}^*_{nLS}(\tilde{c})) \end{array}, & \begin{array}{l}\text{if } (\tilde{f}_{tf}, \tilde{\tau}_{nf}) \notin \tilde{\mathcal{V}}_L \\ \text{and } \tau_{nf} \neq 0\end{array} \\ \tilde{c} = 0, & \begin{array}{l}\text{if } \tau_{nf} \neq 0 \\ \text{and } f_{tf} = 0\end{array} \\ \tilde{c} \to \pm\infty, & \begin{array}{l}\text{if } \tau_{nf} = 0 \\ \text{and } f_{tf} \neq 0\end{array} \\ \tilde{c} \text{ undefined}, & \begin{array}{l}\text{if } \tau_{nf} = 0 \\ \text{and } f_{tf} = 0\end{array} \end{cases} \tag{2.80}$$

This algorithm provides the instantaneous CoR by using only a measure of the friction wrench and the parameter k, to which, as discussed in Section 2.3, the NLS has a very low sensitivity.

The CoR c (or equivalently $\tilde{c}$) will be used in Chapter 3 to present a dynamic model of the planar slider that describes the motion as a rotation about the CoR (with a 1DOF system), such a system will be used to estimate the angular velocity through a nonlinear observer. The CoR position and the slipping velocity will be used to do both slipping avoidance and in-hand manipulation.

2.6 Conclusions

This chapter presented the soft contact theory on which this thesis is built. The friction is described with the well-known Limit Surface theory. After a preliminary description of the LS framework, the chapter focuses on contacts that have an axisymmetric pressure distribution. Such a class of contacts covers a large set of scenarios involving soft fingertips.

After some preliminaries, an algorithm to solve the LS inverse problem has been provided. This algorithm is able to estimate the CoR position given a measure of the friction force and torque.

Finally, the LS theory is extended by adding the description of the viscous friction. With the viscous friction, the total friction wrench can be outside the LS, this permits to generalize the CoR estimation algorithm to such a case.

Chapter 3

Dynamic Modeling and Grasp Control

This chapter presents one of the major contributions of this thesis, namely, a novel dynamic model of a planar slider. A planar slider is a rigid body that can move only in a 2D space in which it can translate and rotate while it is subject to friction forces and torque by means of a fingertip that is in contact with it.

The dynamic model of the planar slider presented in this thesis merges the static friction description of the Limit Surface (Chapter 2) with the LuGre dynamic friction model (Canudas De Wit et al. 1995) and describes the motion as a pure rotation about the Center of Rotation. A complete stability analysis of the model is carried out.

This chapter will study also the observability of the dynamic model so as to propose a nonlinear observer able to estimate the relative slipping velocity using only the measures of the friction forces and torque at the fingertip.

The model presented in this chapter describes a generic contact between a soft fingertip and a planar slider. Such a model will be used to control the grasp force of a parallel gripper equipped with sensorized fingertips. The observer will be used to build up a control algorithm to both regulate the estimated velocity to zero (slipping avoidance) or to follow a desired velocity profile (slipping control).

The proposed approach is exploited to propose two in-hand manipulation maneuvers, the *object pivoting* and the *gripper pivoting*. These control modalities will be used in Chapter 4 to design various motion/manipulation planners able to automatically use such abilities.

The main contributions of this chapter have been published in (Cavallo et al. 2020; Costanzo, De Maria, and C. Natale 2020a,b).

Section 3.1 will briefly review the literature about dynamic friction mod-

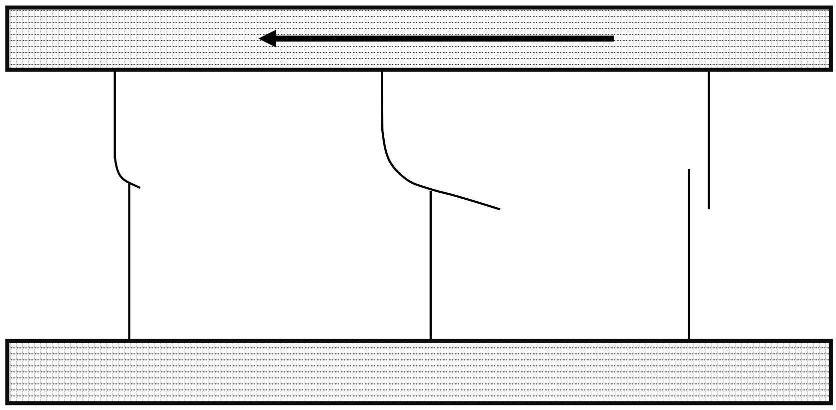

Figure 3.1: Friction Interaction between two bodies visualized with the bristle model.

eling. In particular, the focus will be on the LuGre friction model which is the starting point for the planar slider model of this thesis. Section 3.2 presents the planar slider model and Section 3.3 carries out a complete stability analysis. Section 3.4 presents the nonlinear observer aimed to estimate the relative slipping velocity. In Section 3.5 the observer is exploited to build up a velocity controller aimed to regulate the slipping velocity to zero. Finally, Section 3.6 and 3.7 presents in-hand manipulation strategies that exploit the planar slider dynamic model so as to change the relative orientation between a parallel gripper and a grasped object.

Various experiments have been carried out to demonstrate the effectiveness of the approach.

3.1 Dynamic Friction Modelling

This section is a brief overview of the friction modeling literature.

Friction is a phenomenon hard to model and not yet completely understood. The classical formulation is a static map between the slipping velocity and the friction force. An example is the Coulomb friction law and its generalization, the Limit Surface (Chapter 2).

In dynamic conditions, the variation rate of the sliding velocity does influence the actual friction force (Ruderman 2017). Studies, such as (Armstrong-Hélouvry 1991; Armstrong-Hélouvry, Dupont, and Canudas De Wit 1994), show that a dynamic friction model is necessary to accurately describe the friction phenomena.

One of the first dynamic models was proposed by Dahl (1968). While observing the behavior of ball bearings, he noted that very small input forces were reacted against by small elastic forces. From this observation, he developed his theory of solid friction in which he describes friction as the macroscopic result of quantum mechanical bonds between two contact surfaces. Inter-molecular bonds keep the surfaces together, but shear forces may cause them to break. Low forces are not able to break the mechanical bond and the corresponding behavior is elastic and spring-like. Hence, after removing the input force, the bonds return to their original state. If the load is larger, the bonds undergo permanent displacement analogous to plastic deformation, and, after the relaxation of the load, the bonds will not return to exactly their previous state. A commonly-used analogy to exemplify this concept is the bristle model (Fig. 3.1) that represents the friction as an interaction between micro elastic bristles. Initially, a low applied force will merely deform the bristles elastically. If the load is removed, the bristles will return to their original positions. However, when the load exceeds the maximum bristle deformation, the entire body moves. The stiffness of the bristle is equivalent to the elasticity of the contact surfaces. A simple version of the Dahl model is the following

$$F = F_c \left(1 - e^{-\sigma_0 |x| / F_c}\right) \operatorname{sign}\left(\frac{\mathrm{d}x}{\mathrm{d}t}\right), \tag{3.1}$$

where F is the friction force, x is the displacement at the contact, σ_0 is the stiffness of the bristles and F_c is the classical Coulomb friction force. The Dahl model is well understood theoretically, in fact, problems such as hysteresis effects and the existence and uniqueness of the solution were studied by Bliman (1992).

Another dynamic model is proposed by Armstrong-Hélouvry (1991) that, in practice, describes the phenomenon with two separate models, one for stiction and another for sliding friction.

The friction model proposed in this thesis is built directly on top of the LuGre friction model that was originally introduced by Canudas De Wit et al. (1995) and revised by Johanastrom and Canudas De Wit (2008). The name comes from the abbreviation of the Lund Institute of Technology and the INPG Grenoble, the two universities hosting the cooperating scientists. It is a dynamic friction model that combines the static behavior of the Dahl model with an arbitrary steady-state friction during the sliding. The LuGre model will be analyzed in detail in the next section.

3.1.1 LuGre Model

When two bodies are in contact, the friction forces that they exchange is a macroscopic effect of an interaction that happens at a microscopic scale. At the microscopic level, the surfaces are very irregular and two bodies are in contact at various asperities. As in the Dahl interpretation also in (Canudas De Wit et al. 1995) such interaction is described as two rigid bodies that make contact through elastic bristles (Fig. 3.1). In presence of a tangential force, the bristles deflect like springs giving rise to microscopic displacement (stick phase). In such a case, the elastic force represents the friction force. On the other hand, if the force becomes too large, the bristles deflect too much and the body slips. The friction force when the slip occurs is called break-away force. The LuGre model describes the average behavior of the bristles with a state variable ζ associated to the following nonlinear differential equation

$$\dot{\zeta} = v - \frac{|v|}{g(v)}\zeta \tag{3.2}$$

where v is the slipping velocity which, in general, could be another state variable associated with the motion of the object. $g(\cdot)$ is a positive function and represents the maximum dry friction force that the contact can generate. For example, in the case of classical Coulomb friction

$$g(v) = \mu f_n = \text{const.} \tag{3.3}$$

Canudas De Wit et al. (1995) propose a parametrization of $g(v)$ that catches the Stribeck effect (Armstrong-Hélouvry 1991).

The predicted friction force associated to the bending of the bristles is

$$f_f = \sigma_0\zeta + \sigma_1\dot{\zeta} + \sigma_2 v \tag{3.4}$$

where $\sigma_0\zeta$ and $\sigma_2 v$ represent the dry and viscous friction respectively, while the term $\sigma_1\dot{\zeta}$ is the micro damping effect associated to the motion of the bristles.

At constant non-zero velocity, the steady state friction force is

$$f_f = g(v)\,\mathrm{sign}(v) + \sigma_2 v \tag{3.5}$$

that corresponds to the sum of the maximum dry friction force and the viscous one.

Johanastrom and Canudas De Wit (2008) review the LuGre model studying the properties of zero-slip displacement, invariance, and passivity.

3.2 Planar Slider: Dynamic Model

This thesis presents a novel model of *planar slider* originally presented in (Costanzo, De Maria, and C. Natale 2020b) and (Cavallo et al. 2020).

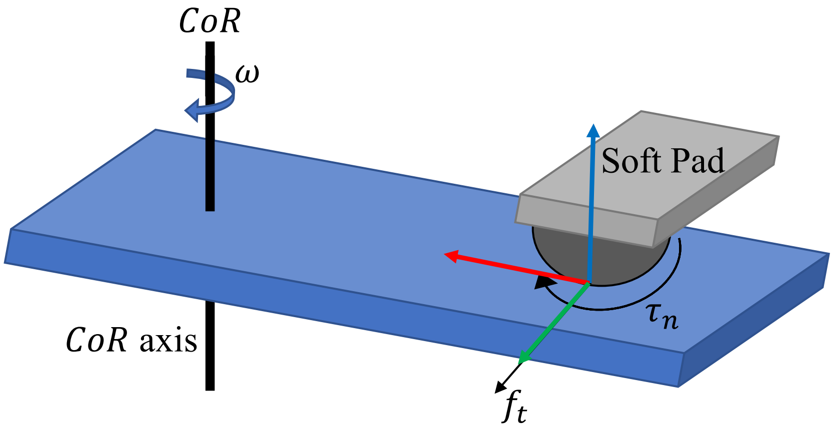

Figure 3.2: Representation of the planar slider.

With reference to Fig. 3.2, a planar slider is a rigid body subject to a motion in a 2D space in which it can translate and rotate. Thus, the motion can be instantaneously described as a pure rotation about the instantaneous Center of Rotation. A soft pad applies a friction wrench on the slider with components laying on a plane; the magnitude of the friction force can be controlled by acting on the force f_n normal to such a plane. The pressure distribution between the slider and the pad is assumed axisymmetric with the same expression of (2.23). Thus, we are in the same framework described in Chapter 2 and all the results on the Limit Surface and the instantaneous motion description holds.

In Section 2.2 it was useful to use a particular reference frame with the x-axis aligned to the CoR position. As a consequence, the tangential force resulted aligned to the y-axis. Orienting the axis with respect to the CoR position was a natural choice because the Limit Surface represents a map from the instantaneous motion (CoR position) to the corresponding friction wrench. The dynamic formulation is the dual one, we want to find a map form the forces to the instantaneous motion (i.e., the sliding velocity). Considering this, it is straightforward to adopt the dual equivalent choice for the reference frame. Thus, given the friction wrench, it is possible to define a contact frame with the z-axis normal to the contact surface in the direction of the normal load f_n, the y-axis along the direction of the tangential force f_t and the origin located in the Center of Pressure (CoP) of the contact area. Given the axisymmetric pressure distribution, this choice implies that the CoR lies on the x-axis and it can be represented with its x-coordinate c. Therefore, the friction load acting on the planar slider can be represented by the three-dimensional wrench

$$\boldsymbol{w} = \begin{bmatrix} 0 & f_t & \tau_n \end{bmatrix}^T \tag{3.6}$$

and the CoR has coordinates

$$\boldsymbol{p}_c = \begin{bmatrix} c & 0 & 0 \end{bmatrix}^T . \tag{3.7}$$

The dynamic model of the planar slider describes the motion as an instantaneous rotation about the CoR axis. It is a 1DOF system and all the forces and torques are suitably transferred to the CoR axis as a pure torque. Note that the angular velocity about the CoR axis corresponds to the same velocity ω around the z-axis. Such model is represented by the following set of nonlinear equations

$$\dot{\zeta} = \omega - \frac{\sigma_0}{g(f_n,\, c)} \zeta \, |\omega| \tag{3.8}$$

$$\dot{\omega} = \frac{1}{J}(-\sigma_0 \zeta - \sigma_1(f_n,\, c)\omega + u). \tag{3.9}$$

The first equation is a modified version of the LuGre friction model and ζ is the LuGre state variable, σ_0 is the so-called asperity stiffness, while $\sigma_1(f_n,\, c)$ is the viscous friction coefficient; the second equation represents the dynamics of the rotational velocity ω of the slider about the CoR axis with inertia moment J and subject to both static and viscous friction torques $\sigma_0 \zeta$ and $\sigma_1(f_n,\, c)\omega$ respectively. Thus, the slider is subject to a total friction torque $\sigma_0 \zeta + \sigma_1(f_n,\, c)\omega$. u is the external load seen as a pure torque about the CoR axis (as an example u may contain the gravitational load). $g(f_n,\, c)$ is the maximum static friction torque referred to the CoR axis, it depends on the normal force f_n and on the instantaneous CoR position c. To simplify the notation we will use the following symbols to denote the maximum static friction torque and the viscous friction coefficient

$$g(\cdot) = g(f_n,\, c) \tag{3.10}$$

$$\sigma_1(\cdot) = \sigma_1(f_n,\, c). \tag{3.11}$$

The maximum dry friction force and the viscous one can be obtained by transforming the wrenches in the contact frame to a pure torque around the CoR axis. The transformation can be easily obtained as

$$\tau^{CoR} = \tau^{CoP} - c f^{CoP} \tag{3.12}$$

where $\boldsymbol{w}^{CoP} = \begin{bmatrix} 0 & f^{CoP} & \tau^{CoP} \end{bmatrix}$ is a generic wrench in the contact frame and τ^{CoR} is the corresponding torque around the CoR axis.

Recalling the expressions of the viscous friction force and torque (2.67) – (2.68), and by using the transformation (3.12), the corresponding viscous torque around the CoR is

$$\sigma_1(\cdot)\omega = \tau_v^{CoR} = -\pi \rho^4 \beta_A \left(\tilde{c}^2 + \frac{1}{2} \right) \omega. \tag{3.13}$$

Thus, the viscous friction coefficient $\sigma_1(\cdot)$ is given by

$$\sigma_1(f_n,\, c) = \pi \rho^4 \beta_A \left(\tilde{c}^2 + \frac{1}{2} \right). \tag{3.14}$$

The maximum dry friction torque $g(\cdot)$ can be constructed by following the same argument used for $\sigma_1(\cdot)$. It is the Limit Surface point $(f_{tLS},\, \tau_{nLS})$ transformed to a pure torque about the CoR axis by using the transformation (3.12). It is important to consider that $g(\cdot)$, in the LuGre model, is always positive and represents the magnitude of the maximum dry friction, moreover, f_{tLS} and τ_{nLS} independently contribute to $g(\cdot)$. Thus, the maximum dry friction torque has expression

$$\begin{aligned} g(f_n, c) &= |\tau_{nLS}| + |c f_{tLS}| \\ &= \tilde{\tau}^*_{nLS}(\tilde{c})\tau_{n\max}(f_n) + \left| c \tilde{f}^*_{t\,LS}(\tilde{c}) \right| f_{t\max}(f_n). \end{aligned} \tag{3.15}$$

The functions $\tilde{\tau}^*_{nLS}(\tilde{c})$ and $\tilde{f}^*_{t\,LS}(\tilde{c})$ are described in Section 2.3, moreover $\tau_{n\max}$ and $f_{t\max}$ are the same of Section 2.2 but, here, they are explicitly written as functions of the normal load f_n. Computing $g(\cdot)$ in (3.15) requires computation of the CoR position c (or, equivalently, its normalized version $\tilde{c}$) that can be obtained using the algorithm described in Section 2.5.2 and synthesized in (2.80).

Now we will study some properties of the proposed dynamic model. Firstly, the input u is assumed piece-wise continuous and bounded, $u \in \mathcal{L}_\infty$. It is clear that the vector field in (3.8) – (3.9) is piece-wise continuous in t and is locally Lipschitz in $(\zeta,\, \omega)$. Thus, given any initial condition $(\zeta(t_0),\, \omega(t_0))$, a unique solution exists in $[t_0,\, t_0 + T)$ with a suitable $T > 0$. Such solution belongs to $C^0([t_0,\, T))$. We shall now show that this solution is forward complete, i.e., $T \to \infty$. To this aim it is sufficient to show that all solutions are bounded (Hartman 2002, Corollary 3.2 at p. 14). Preliminarily, for a vector $\boldsymbol{v}$, let $\|\boldsymbol{v}\|$ denote the Euclidean norm. For a given (invariant) set $\mathcal{Z}$ the distance from a point $\boldsymbol{z} \in \mathbb{R}^2$ and the set $\mathcal{Z}$ is $\|\boldsymbol{z}\|_{\mathcal{Z}} = \inf_{\boldsymbol{y} \in \mathcal{Z}} \|\boldsymbol{z} - \boldsymbol{y}\|$. Then the following boundedness property holds.

Proposition 3.1 (Boundedness)**.** *For any u such that $|u| < g(\cdot)$, the rectangle*

$$\mathcal{Z} = \left\{ (\zeta, \omega) \in \mathbb{R}^2 \,:\, |\zeta| \le \frac{g(\cdot)}{\sigma_0},\, |\omega| \le \frac{g(\cdot)}{\sigma_1(\cdot)} \right\} \tag{3.16}$$

is positively invariant (i.e., all the solutions starting in $\mathcal{Z}$ remain in $\mathcal{Z}$) and asymptotically attractive, i.e., $\lim_{t\to\infty} \left\| \begin{bmatrix} \zeta & \omega \end{bmatrix}^T \right\|_{\mathcal{Z}} = 0$, while for any bounded $|u| > g(\cdot)$ the rectangle

$$\mathcal{Z}_u = \left\{ (\zeta, \omega) \in \mathbb{R}^2 \,:\, |\zeta| \le \frac{|u|}{\sigma_0},\, |\omega| \le \frac{|u|}{\sigma_1(\cdot)} \right\} \tag{3.17}$$

is positively invariant.

Proof. See Appendix A.1. □

Moreover, in view of the Bendixson criterion (Yanqian, Sui-lin, and Chi Y 1986), the system (3.8) – (3.9) with $u = 0$ has no periodic orbits since the divergence of the vector field has a constant sign in $\mathbb{R}^2$.

The following Section will analyse the model (3.8) – (3.9) studying some stability properties.

3.3 Stability Analysis

In the study of the properties of the equilibrium points we will assume $u = \bar{u} = \text{const}$, and f_n and c constant such that $g(\cdot)$ and $\sigma_1(\cdot)$ are constant. The equilibrium points of the dynamic system (3.8) – (3.9) are the solutions of the nonlinear algebraic system

$$0 = \omega - \frac{\sigma_0}{g(\cdot)} \zeta \, |\omega| \tag{3.18}$$

$$0 = -\sigma_0 \zeta - \sigma_1(\cdot) \omega + \bar{u} \tag{3.19}$$

which can have multiple solutions depending on $\bar{u}$. If $|\bar{u}| < g(\cdot)$, then the only equilibrium point is

$$\begin{pmatrix} \bar{\zeta} \\ \bar{\omega} \end{pmatrix} = \begin{pmatrix} \frac{\bar{u}}{\sigma_0} \\ 0 \end{pmatrix}. \tag{3.20}$$

In fact, any other solution would imply $\sigma_0 \zeta = g(\cdot) \operatorname{sign}(\omega)$, resulting in $\operatorname{sign}(\omega) = \operatorname{sign}(\bar{u}/g(\cdot) - \operatorname{sign}(\omega))$, that is impossible when $|\bar{u}| / g(\cdot) < 1$.

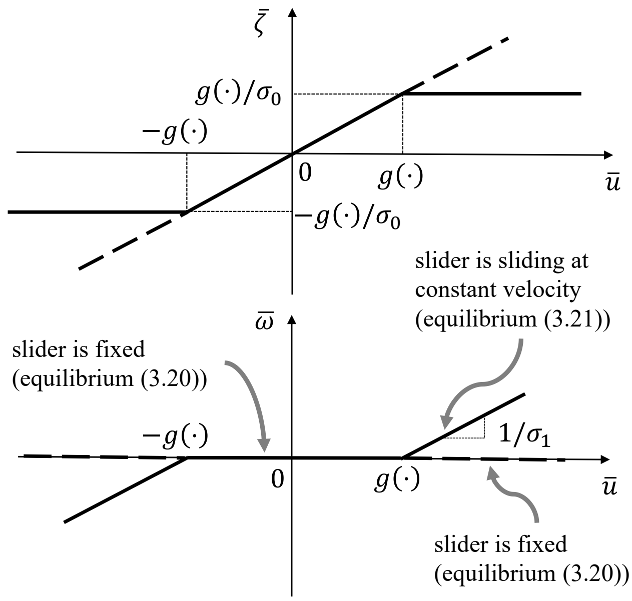

Figure 3.3: Bifurcation diagram of the equilibrium points for the first (top) and second (bottom) state variables. The solid lines refer to stable equilibria while the dashed lines refer to unstable ones.

If $\bar{u} \geq g(\cdot)$, the system has both the equilibrium point (3.20) and the following one

$$\begin{pmatrix} \bar{\zeta} \\ \bar{\omega} \end{pmatrix} = \begin{pmatrix} \frac{g(\cdot)}{\sigma_0} \\ \frac{\bar{u}-g(\cdot)}{\sigma_1(\cdot)} \end{pmatrix}. \tag{3.21}$$

If $\bar{u} \leq -g(\cdot)$, the equilibrium point (3.20) still holds, but, moreover, there is also the following one

$$\begin{pmatrix} \bar{\zeta} \\ \bar{\omega} \end{pmatrix} = \begin{pmatrix} -\frac{g(\cdot)}{\sigma_0} \\ \frac{\bar{u}+g(\cdot)}{\sigma_1(\cdot)} \end{pmatrix}. \tag{3.22}$$

This result can be summarized in the bifurcation diagram in Fig. 3.3, where the projections of the transcritical bifurcation (Drazin 2002) at the points where $|\bar{u}| = g(\cdot)$ on the planes $(\bar{u}, \bar{\zeta})$ and $(\bar{u}, \bar{\omega})$ are clearly visible. Note that the solid and dashed lines correspond to stable and unstable equilibria, respectively, as it will be proved hereafter.

Remark 3.1. The original LuGre model in (Canudas De Wit et al. 1995) did not show any bifurcation since the relative velocity was assumed a nonnull constant, while in the present model it is a state variable describing the motion of the slider. On one hand, assuming a constant velocity, it can accurately describe how the friction force counteracts the tangential load during the sliding phase, e.g, for friction compensation applications. On the other hand, the model under such assumption is not suitable to describe the friction forces in case the aim is to exploit the friction to control the sliding velocity of the slider, that is the main objective of this thesis.

In the presence of bifurcations, it is relevant to study the stability of the equilibria. The result in Proposition 3.1 is applied in the following theorem to prove the Global Asymptotic Stability (GAS) of the equilibrium point (3.20).

Theorem 3.1 (Global Asymptotic Stability of Equilibrium (3.20))**.** *Consider the system* (3.8) – (3.9) *and assume a constant input* $u = \bar{u}$ *such that* $|\bar{u}| < g(\cdot)$ *and a constant* $f_n > 0$ *and* c *such that the functions* $g(\cdot)$ *and* $\sigma(\cdot)$ *are constant. Then the solution of the system* (3.8) – (3.9) *converges globally asymptotically to* (3.20).

Proof. See Appendix A.2. □

The stability of the equilibrium point (3.20) just proved is important to establish if the slider under a sufficiently high normal load ($g(f_n, c) > |\bar{u}|$) such that it is fixed is able to absorb perturbations of such equilibrium. As an example, this might happen when the slider is an object grasped by a robotic gripper with a given grasping force, as in the case study discussed in the experiment sections of this chapter. An external disturbance might perturb the equilibrium position causing a slippage, and for the application it is important to know if the object will stop sliding after the perturbation or will continue its motion. Note that Theorem 3.1 requires that all the system inputs are constant. Unfortunately, this may be not true if the perturbation causes a change of the gravitational torque and, in turn, of u and c. Moreover, if the normal load is updated online, also f_n may be time-variant. In such cases, it is necessary to study the stability of the equilibrium trajectory. This is still an open issue and it will be object of future investigations.

On the other hand, if the normal load is so low that the external load overcomes the maximum friction then one would expect that a sliding velocity builds up. Actually, in a condition with $g(f_n, c) < |\bar{u}|$ the dynamic model (3.8) – (3.9) still has the equilibrium point (3.20), which means that the slider is fixed even with such a low grasp force. This behavior would not be physically coherent unless such equilibrium were unstable. This is proved by the following Proposition.

Proposition 3.2 (Instability of Equilibrium (3.20)). *Assuming a constant input* $u = \bar{u}$, *if* $|\bar{u}| > g(\cdot)$ *and if*

$$\sigma_0 > \frac{(\sigma_1(\cdot))^2}{4J\left(\frac{|\bar{u}|}{g(\cdot)} - 1\right)} \tag{3.23}$$

the equilibrium point (3.20) *of the system* (3.8) – (3.9) *is unstable.*

Proof. See Appendix A.3. □

Remark 3.2. The relevance of Proposition 3.2 can be understood with reference to the application case of a desired sliding rotation about the CoR. Suppose that the system is in the stable equilibrium (3.20) with $|\bar{u}| < g(\cdot)$ and an intentional rotation of the slider is required (object pivoting in-hand maneuver). This can be achieved by reducing the normal load f_n, and thus $g(f_n, c)$, such that $g(f_n, c) < |\bar{u}|$. If in the reality a relative speed builds up, the standard LuGre model does not capture such behavior because the state gets stuck to the point (3.20) that is an equilibrium for $|\bar{u}| > g(\cdot)$, even though unstable. Therefore, to capture the sliding motion starting from a stable equilibrium by reducing $g(f_n, c)$ it is necessary to perturb the state by introducing a modification of the equations. This is relevant only for simulation purposes.

It remains the analysis of the equilibrium states (3.21) and (3.22). Only the first one will be discussed for brevity because the discussion on the second one is analogous.

Proposition 3.3 (Stability of Equilibrium (3.21)). *Considering a constant* $u = \bar{u}$ *and a constant* $f_n > 0$ *and* c *such that the functions* $g(\cdot)$ *and* $\sigma(\cdot)$ *are constant, the point* (3.21) *is an asymptotically stable equilibrium state of the system* (3.8) – (3.9) *with* $\bar{u} > g(\cdot)$. *Moreover, for any given scalar* λ *let*

$$\omega_0 = \frac{\sigma_0 g(\cdot)}{4J\lambda^2 \sigma_1(\cdot)}. \tag{3.24}$$

Then an estimate of the domain of attraction is

$$\mathcal{D} = \left\{ (\zeta, \omega) \in \mathbb{R}^2 \, : \, \lambda^2 \left(\zeta - \frac{g(\cdot)}{\sigma_0} \right)^2 + (\omega - \bar{\omega})^2 < (\bar{\omega} - \omega_0)^2 \right\}. \tag{3.25}$$

Proof. See Appendix A.4. □

Remark 3.3. Note that any estimate of the domain of attraction cannot intersect the line $\omega = 0$ since this line contains the unstable equilibrium state (3.20) with $|u| > g(\cdot)$.

As the Theorem 3.1, Preposition 3.3 requires that all the system inputs are constant. Again, removing this hypothesis requires to study the equilibrium trajectory. This is even more interesting for the equilibrium (3.21) and (3.22) that varies as soon as the normal force or the external load changes since a possible application is to change the normal force so that to induce a desired slider motion. Even if, by means of numerical simulations, the equilibrium trajectory seems stable, the mathematical proof is still an open issue and it will be object of future investigations.

3.4 Estimation of the relative velocity

The aim of the slipping control is that of regulating the relative velocity between the slider and the fingertip pad to zero by acting on the grasp force. This can be trivially done if we would able to directly measure the relative sliding speed ω. Since this measurement is not available, the slipping control strategy is based on the estimation of the relative speed by using a nonlinear observer based on the dynamic model (3.8) – (3.9) whose inputs are the measured friction and normal load between the slider and the fingertip, by means of a six-axis force/torque sensor integrated into the fingertip soft pad.

The measured force and torque at the fingertip can be easily transformed to the pure torsional moment about the CoR axis by using (3.12). Thus, the total friction torque at the CoR is considered measurable and it is possible to add the following output equation to the system (3.8) – (3.9),

$$y = h(\zeta, \omega) = \sigma_0 \zeta + \sigma_1(\cdot)\omega, \tag{3.26}$$

which means that we can measure the superposition of the dry friction $\sigma_0\zeta$ and the viscous one $\sigma_1(\cdot)\omega$.

The first step is to study the observability of the dynamic model (3.8) – (3.9) with the output equation (3.26).

Proposition 3.4 (Observability). *Let*

$$\mathcal{M} = \left\{(\zeta,\, \omega) \in \mathbb{R}^2 \,:\, \omega > 0\right\}, \tag{3.27}$$

then the system (3.8) – (3.9) *with output equation* (3.26) *is locally weakly observable (Hermann and Krener 1977) at any initial state* $(\zeta(0),\, \omega(0)) \in \mathcal{M}$*. Moreover, the same holds in the domain*

$$\mathcal{M}' = \left\{(\zeta,\, \omega) \in \mathbb{R}^2 \,:\, \omega < 0\right\}. \tag{3.28}$$

Proof. See Appendix A.5. □

Given the observability, it is meaningful to propose the following nonlinear closed-loop observer to estimate the relative velocity ω, i.e.,

$$\dot{\widehat{\zeta}} = \widehat{\omega} - \frac{\sigma_0}{g(\cdot)}\widehat{\zeta}\,|\widehat{\omega}| \tag{3.29}$$

$$\dot{\widehat{\omega}} = \frac{1}{J}(-\sigma_0\widehat{\zeta} - \sigma_1(\cdot)\widehat{\omega} + y + le_y), \quad l > 0 \tag{3.30}$$

$$\widehat{y} = \sigma_0\widehat{\zeta} + \sigma_1(\cdot)\widehat{\omega} \tag{3.31}$$

being $e_y = y - \widehat{y}$, which can be re-written in a form formally identical to the one of the system equations (3.8) – (3.9), namely

$$\dot{\widehat{\zeta}} = \widehat{\omega} - \frac{\sigma_0}{g(\cdot)}\widehat{\zeta}\,|\widehat{\omega}| \tag{3.32}$$

$$\dot{\widehat{\omega}} = \frac{1+l}{J}\left(-\sigma_0\widehat{\zeta} - \sigma_1(\cdot)\widehat{\omega} + y\right), \tag{3.33}$$

where y plays the same role of the torsional load u and $\frac{J}{1+l}$ plays the role of the inertia moment J.

Such system has the same equilibrium states of the original system and all the results in Section 3.3 still hold for the system (3.32) – (3.33). The equilibria most relevant to the estimation of the sliding velocity are those related to an actual sliding motion that correspond to the case

$$|y| = |\bar{y}| > g(\cdot). \tag{3.34}$$

Without loss of generality, denote with $(\widehat{\zeta}_e,\, \widehat{\omega}_e)$ the equilibrium corresponding to the case $\bar{y} > g(\cdot)$ and considering a constant $y = \bar{y}$, it is

$$(\widehat{\zeta}_e,\, \widehat{\omega}_e) = \left(\frac{g(\cdot)}{\sigma_0},\, \frac{\bar{y} - g(\cdot)}{\sigma_1(\cdot)}\right). \tag{3.35}$$

The stability of the equilibrium state (3.21) of the planar slider model implies that as $t \to \infty$

$$\begin{aligned} \zeta(t) &\to \bar{\zeta} = g(\cdot)/\sigma_0 \\ \omega(t) &\to \bar{\omega} = (\bar{u} - g(\cdot))/\sigma_1(\cdot), \end{aligned} \tag{3.36}$$

then, in view of (3.21),

$$y(t) \to \bar{y} = \sigma_0 \bar{\zeta} + \sigma_1(\cdot)\bar{\omega} = \bar{u}. \tag{3.37}$$

Analogously, for the stability of the equilibrium point (3.35) of the observer, it is

$$\begin{aligned} \widehat{\zeta}(t) &\to \widehat{\zeta}_e = \bar{\zeta} \\ \widehat{\omega}(t) &\to \widehat{\omega}_e = \bar{\omega}, \end{aligned} \tag{3.38}$$

and, of course,

$$\widehat{y}(t) \to \bar{y} = \bar{u}. \tag{3.39}$$

With reference to (3.33), it is evident how

$$l \to \infty \implies y(t) - \widehat{y}(t) \to 0, \, \forall t > 0. \tag{3.40}$$

Now, observing that

$$y - \widehat{y} = \sigma_0(\zeta - \widehat{\zeta}) + \sigma_1(\cdot)(\omega - \widehat{\omega}) \tag{3.41}$$

and that both $\zeta(t)$ and $\widehat{\zeta}(t)$ tend to $g(\cdot)/\sigma_0$ with a dynamics the faster the larger is σ_0, it results

$$\omega(t) - \widehat{\omega}(t) \to 0, \, \forall t > 0 \text{ as } l \to \infty. \tag{3.42}$$

It must be remarked that this is true only assuming a perfect knowledge of the model parameters σ_0, $\sigma_1(\cdot)$ and those of the Limit Surface appearing in $g(f_n, c)$. In case of uncertain parameters the estimation error can be shown only bounded, i.e.,

$$\left| \widehat{\zeta}(t) - \bar{\zeta} \right| < \varepsilon_\zeta \tag{3.43}$$

$$|\widehat{\omega}(t) - \bar{\omega}| < \varepsilon_\omega, \tag{3.44}$$

with $0 < \varepsilon_\zeta < \infty$ and $0 < \varepsilon_\omega < \infty$ and the smaller the better the knowledge of model parameters.

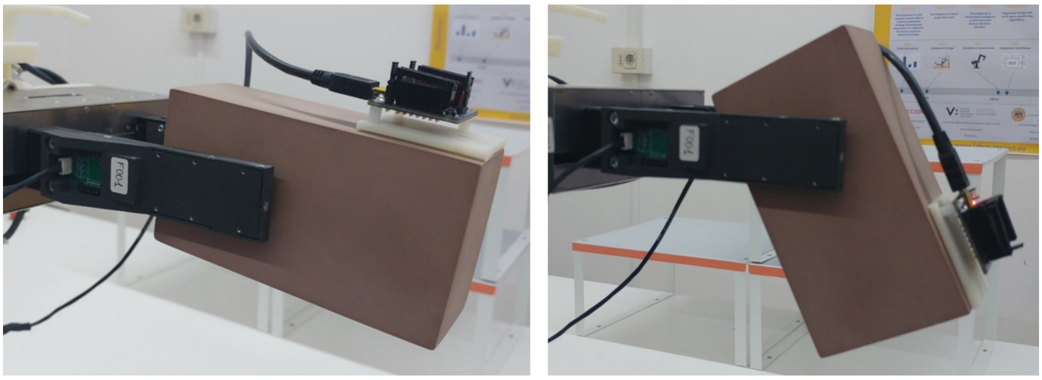

Figure 3.4: Setup of observer experiment: before sliding (left) and after sliding (right).

Remark 3.4 (Two fingers). Despite the formulation presented so far considered a single fingertip in contact with the planar slider, all the experiments will be carried out using a parallel gripper and two sensorized fingers. To apply the formulation presented so far to the case of a parallel gripper, we assume a perfect symmetry of the two contacts and we adopt the concept of the Grasp Limit Surface (GLS) by Shi, Woodruff, et al. (2017). This implies that the maximum static friction torque $g(f_n, c)$ is the double of the one of the single finger, where f_n is the normal force of either finger. Moreover the total friction load (f_{tf}, τ_{nf}) is computed as the sum of the external loads of the two fingers, equivalent to doubling the measured wrench of either finger (see Appendix B.3).

3.4.1 Demonstration of the model

This section presents an experiment aimed at showing the effectiveness of the velocity observer presented in Section 3.4. The experiment is carried out using an industrial gripper WSG-50 by Weiss Robotics equipped with the SUNTouch six-axis force/tactile sensors described in (Costanzo, De Maria, et al. 2019) and based on the technology originally proposed in (De Maria, C. Natale, and Pirozzi 2012). Appendix B reports some details of the sensorized fingers as well as the description of the calibration procedure and friction parameter estimation, while Appendix C describes the gripper and its control interface.

As shown in Fig. 3.4, the gripper is used to grasp a resin block far from its center of gravity (CoG) such that the gravity torsional moment is about 0.03 Nm. An ST iNemo Inertial Measurement Unit (IMU) is attached to the block to measure the actual angular velocity that will be used as ground truth. The experiment starts with a constant normal force of 9 N in total such that the block is firmly grasped. Then the normal force is reduced with a constant decay ratio of 3 N/s down to 6 N so as a rotational sliding motion takes place. The start and end conditions are reported in the left and right pictures in Fig. 3.4, respectively. During the experiment the observer algorithm in (3.32) – (3.33) is running with the parameters reported in Tab. 3.1 and with a feedback gain $l = 100$ tuned so as the estimated output follows the measured one as close as possible. In particular, the friction coefficient μ has been experimentally estimated with the procedure described in Appendix B that consists in rubbing the fingers along the surface of the block.

Parameter	Value
J	$1.1 \cdot 10^{-3}\,\mathrm{kgm}^2$
σ_0	$50\,\mathrm{Nm/rad}$
β_A	$4.4 \cdot 10^5\,\mathrm{Ns/m}^3$
μ	0.61
γ	0.2545
δ	$0.004824\,\mathrm{m/N}^\gamma$

Table 3.1: System parameters used in the observer.

The slider is considered as a rigid body, this implies that the parameters δ and γ of the radius model (2.24) depend only on the sensor pad and not on the object, their estimation is described in Appendix B. An accurate value of the inertia moment with respect to the CoR is not needed owing to the robustness provided by the high feedback gain l of the observer. Thus we used the inertia moment with respect to the CoG. The asperity stiffness σ_0 has only low relevance, it is simply set to a sufficiently high value such that $\zeta(t)$ rapidly converges to $u(t)/\sigma_0$, while the viscous friction coefficient per area unit β_A has been tuned to obtain a low estimation error between $\omega(t)$ and $\widehat{\omega}(t)$.

Figure 3.5 reports the results of the experiment. The first plot clearly shows how the observer is able to capture the velocity peak measured by the IMU. The second plot shows the estimated and actual angular positions, $\widehat{\theta}$ and θ respectively, that are computed as integral of the velocities. Despite it is not observable, the mere integral of the angular velocity provides a good estimation of the angular position. The third plot shows the input signal f_n and the friction torque measured by the sensor τ_{nf} that goes towards lower values during the experiment. Finally, the last plot shows how the static friction $\sigma_0\widehat{\zeta}(t)$ follows $y(t)$ as long as the maximum static friction $g(\cdot)$ is large enough. As soon as the static friction equals the maximum one (this

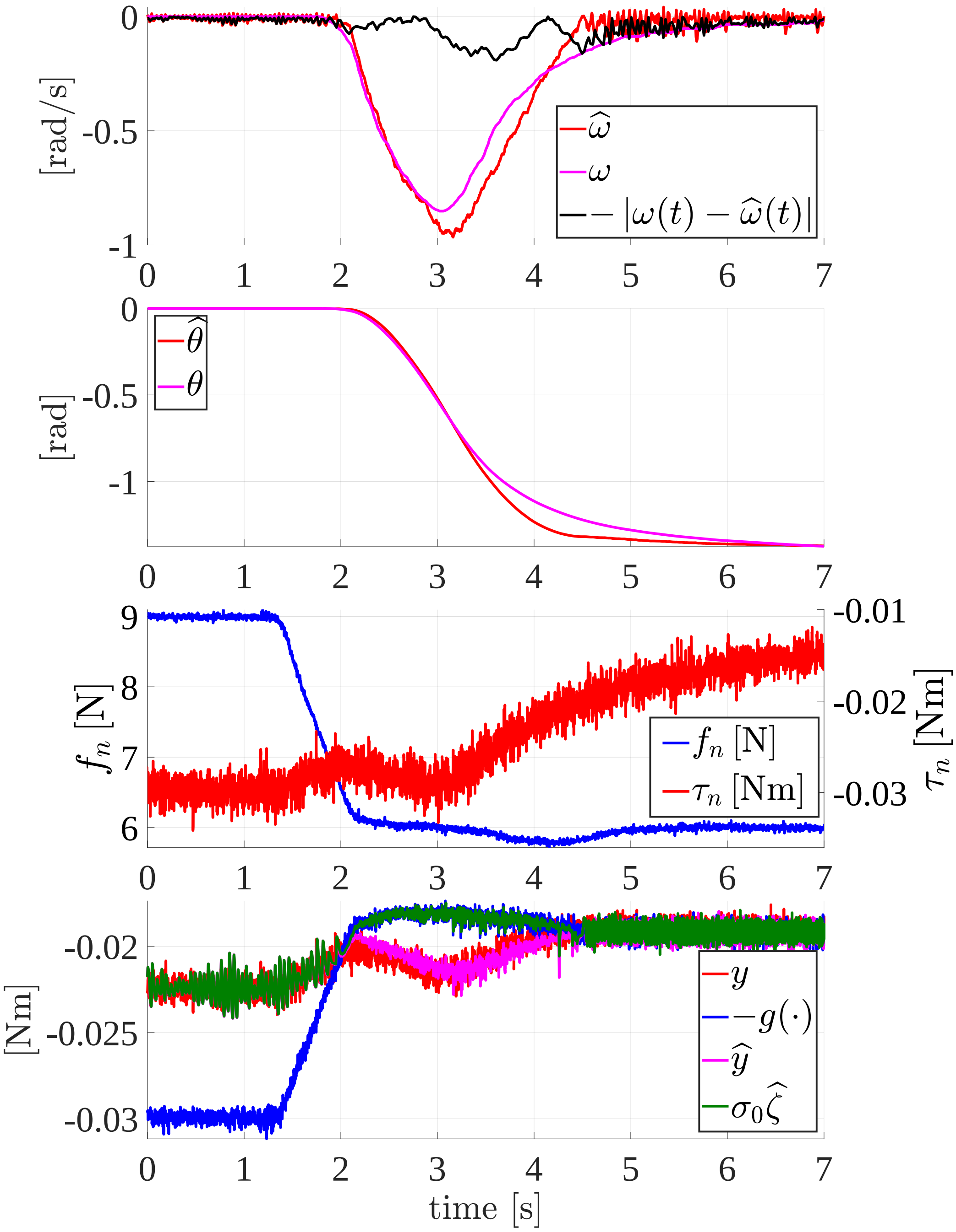

Figure 3.5: Observer Experiment. First figure: measured and estimated slipping velocity and estimation error $|\omega(t) - \widehat{\omega}(t)|$; Second figure: angular positions; Third figure: control input f_n (left-axis), measured friction torque (right-axis); Fourth figure: relation between the maximum dry friction torque $g(\cdot)$ and the generalized measure y.

happens at about 2 s) it starts following $g(\cdot)$ (see the boundedness property in Proposition 3.1) and a relative velocity builds up. As soon as the rotational motion stops because the load is high enough to generate a dry friction torque able to balance the torsional load (at about 4.5 s), the static friction follows the measured output again. Note that $y(t)$ is very close to $\widehat{y}(t)$ owing to the high gain l.

3.5 Grasp Controller: Slipping Avoidance

The objective of the control law is to apply the lowest normal load f_n to keep the slider fixed, i.e., such that $\omega = 0$. If the slider is subject only to constant torsional loads u, then the Limit Surface theory (Chapter 2) implies that the smallest normal force to avoid any slippage in static conditions is f_{nLS}, namely, with reference to Fig. 2.7a, the one that brings the point P on the point P_{LS}. Given the friction load (f_{tf}, τ_{nf}) measured by a force sensor, this value can be easily computed with two alternative algorithms, which will be both presented since each one has its advantages and disadvantages. In view of the definition of the normalized LS and by definition of f_{nLS}, the condition $P \equiv P_{LS}$ is

$$\begin{pmatrix} \tilde{f}_{tf} \\ \tilde{\tau}_{nf} \end{pmatrix} = \begin{pmatrix} \tilde{f}_{tLS} \\ \tilde{\tau}_{nLS} \end{pmatrix}. \tag{3.45}$$

Such condition must be true also in absolute value, i.e.,

$$\begin{pmatrix} \left|\tilde{f}_{tf}\right| \\ \left|\tilde{\tau}_{nf}\right| \end{pmatrix} = \begin{pmatrix} \left|\tilde{f}^*_{tLS}(\tilde{c})\right| \\ \tilde{\tau}^*_{nLS}(\tilde{c}) \end{pmatrix}. \tag{3.46}$$

Recalling the definition of the normalization equations in (2.32), follow that $\tilde{f}_{tf} = f_{tf}/(\mu f_{nLS})$, thus the first entry of the vector relation above yields

$$f_{nLS} = \frac{f_{tf}/\mu}{\left|\tilde{f}^*_{tLS}(\tilde{c})\right|}. \tag{3.47}$$

Note how, in the case of a pure translation ($\tilde{c} \to \infty$ and thus $\left|\tilde{f}^*_{tLS}(\tilde{c})\right| \to 1$, see Fig. 2.6), (3.47) reduces to the adoption of the classical Coulomb friction model $f_{nLS} = \left|f_{tf}\right|/\mu$.

The second algorithm to compute f_{nLS} starts from the second entry of the vector relation (3.46), which, analogously, implies

$$f_{nLS} = \sqrt[\gamma+1]{\frac{\left|\tau_{nf}\right|/(2\mu\xi_k\nu_k\delta)}{\tilde{\tau}^*_{nLS}(\tilde{c})}} \tag{3.48}$$

Note that (3.47) and (3.48) are equivalent, but singular when $\tilde{c} \to 0$ (pure rotation) and $\tilde{c} \to \infty$ (pure translation), respectively. Hence, it is convenient to use the more numerically robust equation depending on the value of $\tilde{c}$.

A direct application of a normal load equal to f_{nLS} cannot ensure slippage avoidance since it corresponds to the limit case of the point P on the LS. Therefore, the actual control load should be computed as

$$f_n(t) = k_s f_{nLS}, \tag{3.49}$$

where $k_s > 1$ is a safety gain slightly larger than 1 to keep the point P inside the LS. Note that this gain provides also a certain degree of robustness to uncertainties affecting the friction parameters. However, it avoids the slider slippage only in static or quasi-static conditions. In fact, it is well-known that when the load is time-varying, the actual friction that a soft contact can withstand decreases as the rate of variation of the load increases. This is because the break-away torsional moment is lower than the static one, as shown by Johannes, Green, and Brockley (1973) and Richardson and Nolle (1976) for the case of linear motion. Such effect is not described by the LS method but it is captured by the LuGre model integrated with the LS as explained in Section 3.2 (Canudas De Wit et al. 1995). Moreover, with rapidly time-varying loads the inertial torques can be significant and a purely static control law is not able to counteract them. The relevance of such effect is shown by Cirillo et al. (2017) where slipping control experiments are carried out in the case of time-varying loads.

To solve this problem, the slipping avoidance control law in (3.49) is modified as follows

$$f_n(t) = k_s f_{nLS}(t) + f_{n_d}(t), \tag{3.50}$$

where $k_s f_{nLS}(t)$ is called static contribution, while the dynamic contribution $f_{n_d}(t)$ is computed based on the estimated relative velocity $\widehat{\omega}(t)$ as

$$f_{n_d}(t) = |C_d \widehat{\omega}(t)| \tag{3.51}$$

where C_d is a suitable linear differential operator and the absolute value is needed to ensure that $f_{n_d} \geq 0$. The linear controller C_d can be represented also with a transfer function

$$C_d(s) = k_d \frac{s + z_d}{s + p_d}, \tag{3.52}$$

where the gain $k_d > 0$ is selected to obtain a quick reaction to any relative velocity and the real zero $-z_d$ and the real pole $-p_d$ are selected so as to reduce the high-frequency gain (thus, $z_d > p_d > 0$), in turn reducing the control sensitivity to the high-frequency noise affecting the measured wrench and thus the estimated velocity in (3.51). Note how $f_{n_d} = 0$ as soon as $\widehat{\omega} = 0$ and only the static control action (3.49) remains when the external load is constant.

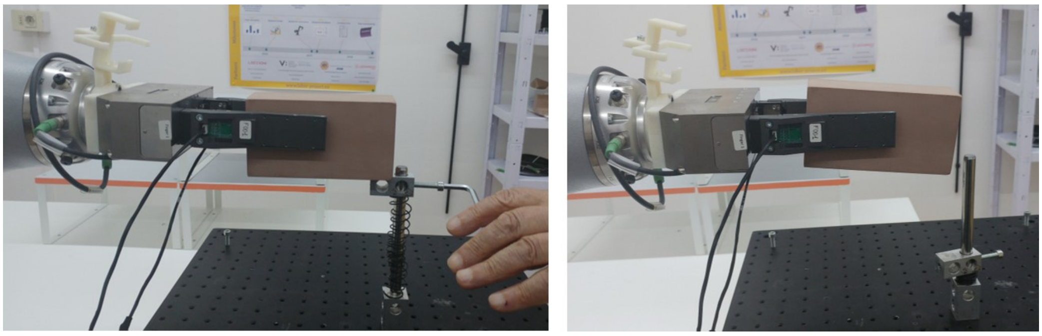

Figure 3.6: Setup of the zero velocity regulation experiment: initial condition (left) and final condition (right).

Remark 3.5. Note that stability of the closed-loop system is ensured by a sufficient $k_d > 0$ since the equilibrium point (3.20) is stable for any $g(\cdot) > |u|$ as proved by Theorem 3.1. In the case of an increase of the load torque such that $g(\cdot) < |u|$, the effect of the controller is simply to increase $g(\cdot)$ so that the condition $g(\cdot) > |u|$ is restored. A simple approach to this issue is to use an integral action ($p_d = 0$). However, this choice could result in excessive normal forces at steady-state, due to the concurrent presence of the static control action f_{nLS}. For this reason, a band-limited integrator has been preferred. The parameters are selected experimentally based on the worst case of a step-wise load change as detailed in the next experiment section.

3.5.1 Demonstration of the slipping avoidance algorithm

This section presents an experiment aimed at showing the effectiveness of the slipping avoidance control strategy in (3.50). The same hardware of the experiment in Section 3.4.1 is adopted. The setup is depicted in Fig. 3.6. The same resin block of the experiment in Section 3.4.1 is grasped far from the CoG but initially with a low normal force (about 7 N) automatically computed by the control law (3.50), because the block is partially supported by a mechanical constraint (left picture).

The parameters of the controller $C_d(s)$ in (3.52) have been tuned in a worst case scenario to the values $k_d = 10$, $p_d = 7$, $z_d = 250$.

The experiment is performed in the following way. The constraint is suddenly removed by acting on the Allen key so that the gravity load is applied with a high rate of variation. Fig. 3.7 presents the results. The first plot shows how the control algorithm reacts to the velocity peaks estimated by the observer by computing a dynamic force according to the control law (3.51). Note that the sole static force is increasing but it would not be sufficient to keep the object fixed since the actual maximum friction torque is lower than the static one foreseen by the LS due to the decrease of the break-away torsional moment. The normal force computed by the control algorithm is reported in the second plot (red line) together with the actual normal force (blue line) measured by the sensor, which is slightly different due to the limited bandwidth of the low-level force control of the gripper. The regulation error is mainly due to the lag caused by the control interface of the gripper (Appendix C). Nevertheless, the actual normal force is sufficient to hold the object with a negligible rotation as demonstrated by the measured torsional load shown in the third plot that reaches a significant steady-state value and by the picture taken at the end of the experiment reported in Fig. 3.6-right.

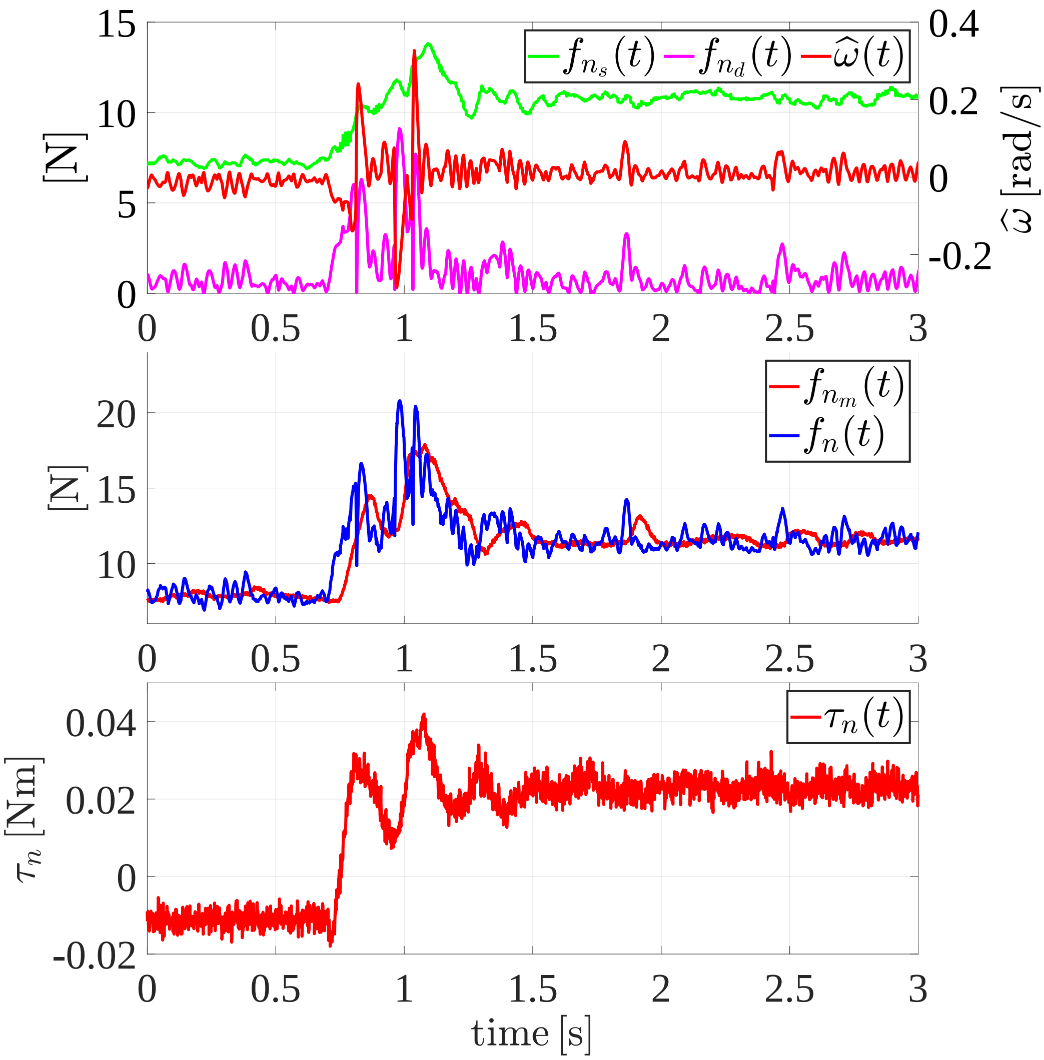

Figure 3.7: Zero velocity regulation experiment. First plot: static control action (green line-left axis), dynamic control action (magenta line-left axis) and estimated relative velocity (red line-right axis). Second plot: computed normal force (blue line) and actual normal force (red line). Third plot: measured torsional moment.

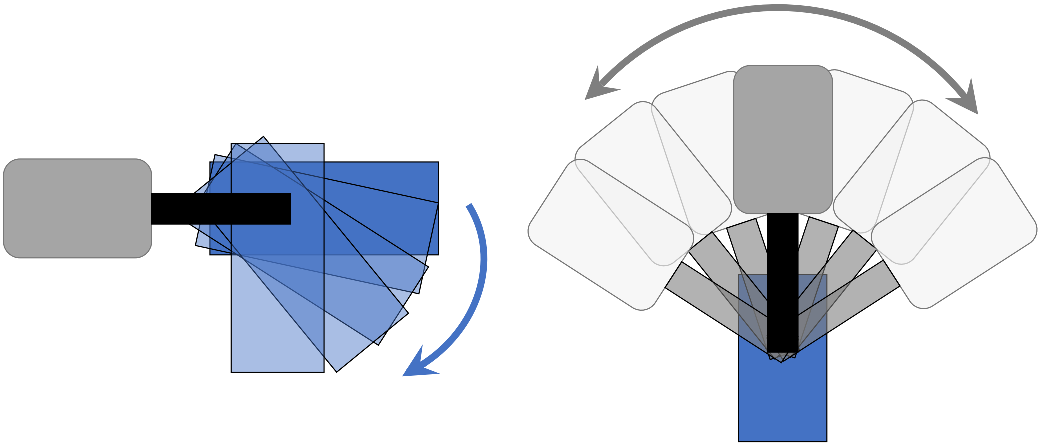

Figure 3.8: Sketch of object pivoting (left) and gripper pivoting (right) maneuvers.

3.6 Grasp Controller: In-Hand Manipulation

The general control law presented so far can be exploited not only to avoid slippage, but it can also be usefully exploited to perform in-hand manipulation tasks such as *object pivoting* and *gripper pivoting*.

Object pivoting consists in keeping the gripper (and in turn the fingers) fixed into the space while changing the orientation of the object as it is represented in Fig. 3.8-left. This is possible by regulating the grasp force so that let the object rotationally slide in hand.

Gripper pivoting is the dual maneuver, it consists in keeping the object orientation fixed in the space while changing the orientation of the gripper by a rotation about the axis of the actuation direction, so as to change the grasp configuration (Fig. 3.8-right). This is possible by regulating the grasp force to the minimum possible value that avoids the translational slippage of the object while allowing the rotational one.

For both tasks, it is important to check the task feasibility through the analysis of the estimated CoR position.

3.6.1 Object Pivoting

The object pivoting is feasible if a reduction of the grasp force will cause a rotation rather than a translation. Physically this means that the external torque at the grasp point must be sufficiently high compared to the external force. But these two quantities are not homogeneous and can not be compared directly. The feasibility can be checked by using the concept of Virtual

CoR (Definition 2.1), in fact, the CoR which would result by reducing the grasp force can be used as a measure of the resulting motion. In particular, if the CoR position is close enough to the grasp axis, the corresponding motion can be considered as a pure rotation. A fair threshold that can be used is the radius of the contact area, thus if $|\tilde{c}| < 1$ the gripper pivoting will be considered feasible with a negligible translation.

To set a desired pivoting angle, an estimation of the angular rotation is needed. The angular position can be obtained by adding an extra state equation to the planar slider model (3.8) – (3.9), i.e.,

$$\dot{\theta} = \omega, \tag{3.53}$$

where the angular position θ is trivially the integral of the angular velocity. Unfortunately the augmented system (3.8) – (3.9),(3.53) with output equation (3.26) is not observable thus it is not possible to build an observer for the angular position θ. Nevertheless, by exploiting the velocity observer of Section 3.4, it is possible to do an object pivoting with a desired velocity profile. This concept will be detailed in Section 3.7.

However, it is still possible to execute a reliable object pivoting to a desired angular position. This can be done by limiting the task to a *vertical object pivoting*, i.e., an object pivoting with a desired angular position such that the line connecting the grasp point and the object's CoG is aligned with the gravity. In other words, the final position will be the one that nullifies the gravity torsional torque, i.e., the stable equilibrium point of a pendulum-like system. This can be achieved by reducing the grasp force from its current value to the value

$$f_{nP} = k_s \; f_{nLS}|_{\tilde{c}\to\infty} = k_s \frac{f_{tf}}{\mu} \tag{3.54}$$

which is the static grasp force contribution (3.49) computed in the case of pure translation that corresponds to the grasp force just needed to counteract the translational sliding but not the rotational one. The reduction of the grasp force is done with an exponential decay characterized by a given time constant. As soon as the grasp force reaches the desired value, the complete slipping avoidance control action can be activated to quickly stop the object rotation, hence avoiding undesirable object oscillation.

3.6.2 Gripper Pivoting

The gripper pivoting is feasible if the initial state is the one at the end of the vertical object pivoting, i.e., if the gravitational torque about the grasp axis is zero. Otherwise, a reduction of the grasp force would make the object

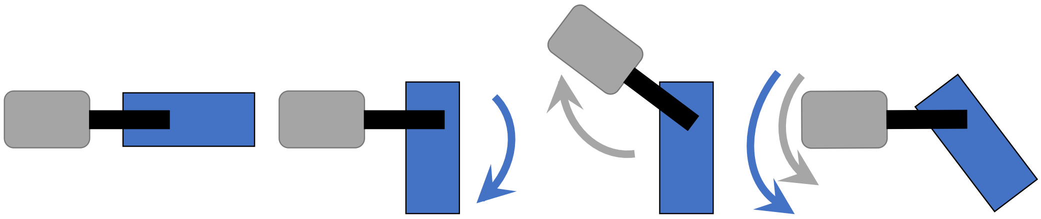

Figure 3.9: Sequence of control modalities that reproduce an arbitrary object pivoting. From left to right: (1) Initial object configuration; (2) vertical object pivoting; (3) gripper pivoting; (4) rotation in slipping avoidance mode.

rotate subject to the gravitational torque. Thus, it is sufficient to check the magnitude of the measured friction torque, it should be below a suitable threshold that depends on the measurement noise. In such a case, it is sufficient to keep the grasp force at the value f_{nP} (3.54) while moving the gripper with a pure rotation about the gripper actuation axis. The applied grasp force is not able to generate any friction torsional moment between the gripper and the object, as a result, the object remains in the pendulum-like stable equilibrium point with a zero-friction torque.

Note that the torque used at the end of the vertical object pivoting is the same required by the gripper pivoting. Thus, it is possible to combine the two manipulation maneuvers, namely, rotating the object to a vertical orientation and then changing the grasp configuration by rotating the gripper in gripper pivoting mode.

As soon as the rotation is completed, the complete slipping avoidance control can be activated to counteract any possible disturbance.

Figure 3.9 shows how, by combining vertical object pivoting, gripper pivoting, and slipping avoidance, it is possible to reproduce an object pivoting at a desired angle. It is sufficient to bring the object to a vertical orientation (vertical object pivoting), then change the relative angle between the gripper and the object to the desired one (gripper pivoting), and, finally, reorient the object to the desired absolute orientation. This consideration will be exploited in Section 4.2 that presents a motion/manipulation planner that is able to automatically choose the sequence of control modalities to complete a desired task.

3.7 Grasp Controller: Velocity Control

This section presents a control law aimed at regulating the grasp force applied to the planar slider (3.8) – (3.9) so as to follow a given sliding velocity profile while avoiding the fall of the manipulated object at the same time. The resulting motion is an object pivoting (Section 3.6.1) but with a target velocity instead of a target orientation.

The design is based on the dynamic model presented in Section 3.2. Assuming that the object has been grasped in a configuration such as the external torque u has constant sign, let denote this sign as s_u. We know from Section 3.3 that during the sliding the LuGre state variable is constant with a sign that depend on the sign of u, namely,

$$\zeta = \frac{g(\cdot)}{\sigma_0} s_u. \tag{3.55}$$

Hence, substituting it in the second system equation (3.9) yields

$$\dot{\omega} = \frac{1}{J}(-g(\cdot)s_u - \sigma_1(\cdot)\omega + u) \tag{3.56}$$

where both $g(\cdot)$ and $\sigma_1(\cdot)$ depend on the CoR position and on the control input f_n through equations (3.15) and (3.14), respectively.

The pivoting must be feasible, thus the CoR must be close to the grasp point, i.e., $|\tilde{c}| << 1$. This implies that

$$g(f_n, c) \simeq \tau_{n\max} = 2\mu\xi_k\nu_k\delta f_n^{\gamma+1} \tag{3.57}$$

$$\sigma_1(f_n, c) \simeq \frac{\pi}{2}\beta_A\delta^4 f_n^{4\gamma} \tag{3.58}$$

The first order dynamics (3.56) is then linearized considering a new control input Δf_n defined as the variation with respect to a constant normal force $\bar{f}_n$ which is the static contribution (3.49) computed before the pivoting execution.

Indicating with f_ω the right-hand side of (3.56), with a slight abuse of notation, the linearized dynamics is

$$\dot{\omega} = \left.\frac{\partial f_\omega}{\partial \omega}\right|_{f_n=\bar{f}_n} \omega + \left.\frac{\partial f_\omega}{\partial f_n}\right|_{f_n=\bar{f}_n} \Delta f_n + \frac{1}{J}u, \tag{3.59}$$

where $\frac{\partial f_\omega}{\partial \omega}$ and $\frac{\partial f_\omega}{\partial f_n}$ are the Jacobians of the function f_ω.

The design of the control algorithm has to take into account also some implementation details, such as some limitation in the gripper control interface used in the experiments (Appendix C). Then a simple loop shaping method is adopted to obtain good stability margins. The resulting algorithm is a simple PID-like, i.e., the transfer function,

$$C_\omega(s) = \frac{k_c}{s}\frac{1+sT_{11}}{1+sT_{12}}\frac{1+sT_{21}}{1+sT_{22}}. \tag{3.60}$$

Note that the sign of the desired velocity has to be the same as the sign of the external torque u otherwise the required motion is unfeasible. In conclusion, assuming a negative desired velocity (case $s_u = -1$), the normal force is computed as

$$f_n = \bar{f}_n + C_\omega(\omega_d - \widehat{\omega}), \tag{3.61}$$

where C_ω is the integro-differential operator corresponding to the transfer function in (3.60) and $\widehat{\omega}$ is the estimated velocity by the observer (3.32) – (3.33). Note that if a positive desired velocity is set (case $s_u = +1$), k_c should be negative.

3.7.1 Experimental demonstration

This section describes an experiment carried out to show the effectiveness of the control law. The experimental setup is the same as the one in Section 3.4.1.

The gripper is used to grasp the same resin block far from its CoG such that the gravity torque is about 0.015 Nm while the IMU measures the actual angular velocity ω. The objective is to let the object rotate in-hand so as to follow a reference velocity. To do that, a trapezoidal velocity profile is used as reference velocity ω_d for the control law (3.61). The model parameters are the same used in Section 3.4.1, while the control parameters are shown in Tab. 3.2.

Control Parameter	Value
k_c	20 N/rad
T_{11}	2.639 s
T_{12}	8.681 s
T_{21}	$5.081 \cdot 10^{-1}$ s
T_{22}	$7.53 \cdot 10^{-2}$ s

Table 3.2: Control parameters used in the experiment.

Figure 3.10 shows the result. The first plot shows the reference trajectory ω_d and the real and estimated velocity ω and $\widehat{\omega}$, respectively.

The second plot shows the angular positions (computed as integral of the velocities). The steady-state difference between the $\widehat{\theta}$ and θ is normal because the angular position is not observable; nevertheless, the error is low. Also the steady-state error between θ_d and $\widehat{\theta}$ is reasonable because the control loop is closed on the angular velocity and not on the angular position.

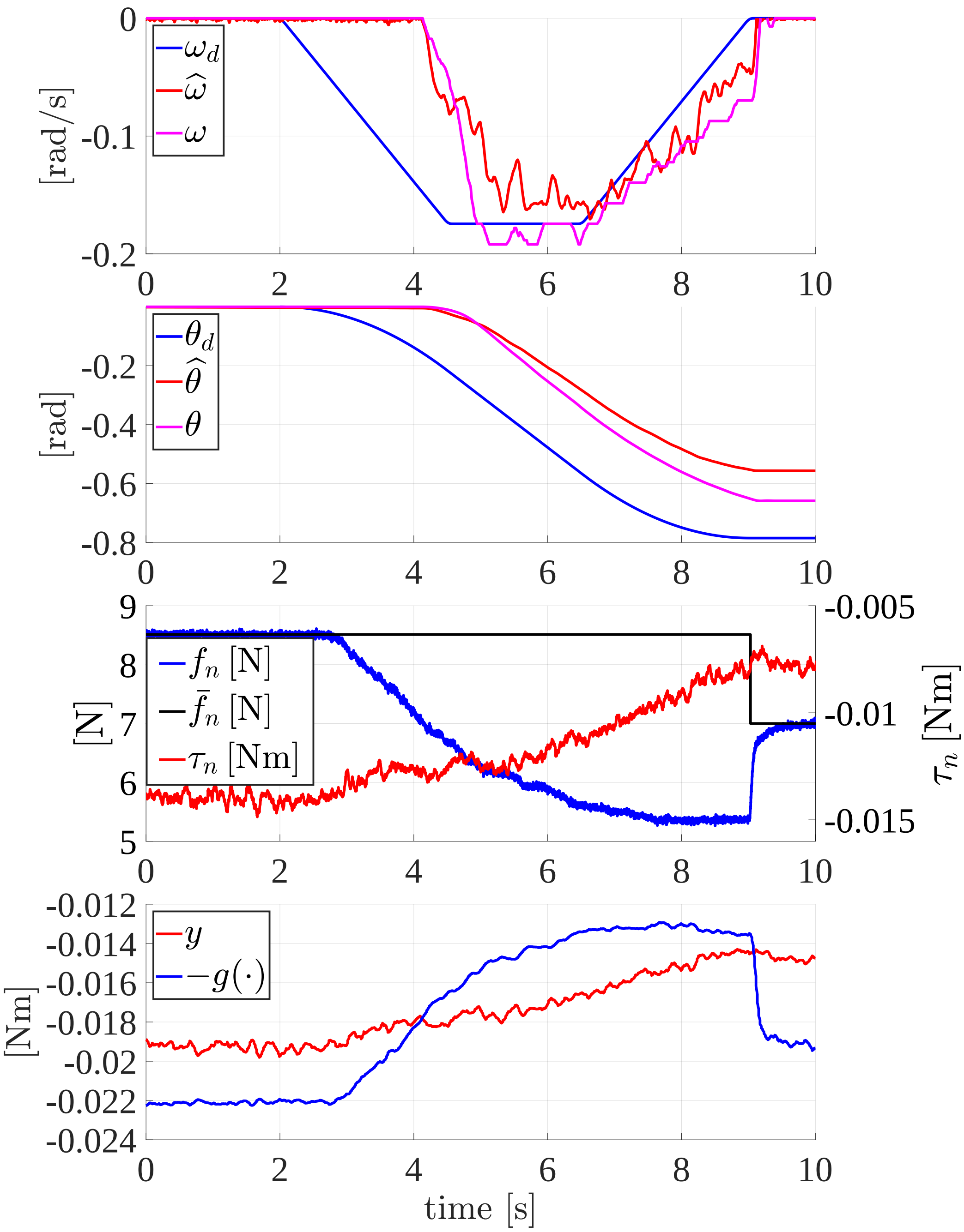

Figure 3.10: Velocity Control Experiment. First figure: desired, measured and estimated velocities; Second figure: angular positions; Third figure: control input f_n (left-axis), measured friction torque (right-axis); Fourth figure: relation between the maximum dry friction torque $g(\cdot)$ and the generalized measure y.

The third plot shows the control signal f_n, the force component $\bar{f}_n$, and the friction torque measured by the sensor τ_{nf} that goes towards lower values during the experiment. $\bar{f}_n$ is kept constant during the pivoting maneuver and it is updated when the reference ω_d goes to zero. The experiment shows again how the observer is able to capture the velocity measured by the IMU. The large initial tracking error is caused by the 5 mm/s threshold of the low-level gripper velocity control loop (see Appendix C).

The fourth plot shows the relation between the maximum dry friction torque $g(\cdot)$ and the generalized measure y defined in (3.26). When $g(\cdot)$ is greater than y (in terms of absolute value), no velocity is generated by the observer because the dry friction can counteract the external torque. Instead, between 4 and 9 seconds, $g(\cdot)$ is lower than y, thus the observer generates the estimated velocity shown in the first plot.

3.8 Conclusions

In this chapter, the Limit Surface theory presented in Chapter 2 has been coupled with the LuGre dynamic friction model to build up a planar slider dynamic model. The model describes the motion as a pure rotation about the CoR, thus, it is necessary to estimate the CoR position by using the algorithm presented in the previous chapter. The equilibrium points stability of the system subject to constant inputs has been theoretically analyzed, but, the case of time-varying input and the stability of the equilibrium trajectory is still an open issue. Finally, after the study of the observability property, this chapter proposed a nonlinear observer able to estimate the slipping velocity. The structure of the observer is identical to the structure of the system, this implies that all the stability properties hold also for the observer. A demonstration showed the observer performance by comparing the estimated velocity with the direct measure given by an IMU.

This chapter presented also the slipping control algorithms. The first modality is the slipping avoidance that provides the normal force as the superposition of a static and a dynamic contribution. The static contribution is computed by using only the LS theory and represents a generalization to the rototranslational case of the Coulomb law. The dynamic contribution is a control action aimed to regulate the estimated slipping velocity to zero. The slipping control algorithm is able to avoid slippage also if the external load rapidly varies as has been shown in an experimental demonstration.

The second control modality concerns the in-hand manipulation abilities. This chapter identified two in-hand manipulation maneuvers, the gripper and object pivoting. The first can be executed by applying the normal force that avoids the translational slippage but not the rotational one. The object pivoting, instead, can be executed in two ways, the vertical object pivoting is easier and requires to gradually apply the same normal force needed for the gripper pivoting. Instead, the generic object pivoting can be performed by controlling the friction torque to a desired value, but this would require to know the initial object orientation.

Finally, this chapter showed how it is possible to perform a controlled object pivoting by using a target velocity profile. This is done by suitably controlling the estimated slipping velocity. Experimental evaluations showed the feasibility of the approach.

From the analysis carried out in this chapter, we learned that in-hand manipulation is possible with very simple hands, i.e., parallel-jaw grippers. The controlled sliding maneuver can potentially enlarge the robot workspace by enabling additional degrees of freedom inside the fingers. In this chapter we showed that it is possible to control the in-hand sliding motion, but, to effectively use such abilities in a real task, we need strategies to choose "when" and "how" use them. The next chapter will be devoted to proposing planning strategies that are able to choose both the arm and the in-hand motion.

Chapter 4

Manipulation Planning and Execution

The in-hand manipulation abilities described in Section 3.6 can be used to enlarge the robot workspace. An example is depicted in Fig. 4.1. Suppose that the robot has to pick the red object in the center of the table and to place it in the middle shelf layer in the goal pose as on the right side of the drawing. Clearly, there is not a fixed grasp which makes both the pick and place poses reachable and collision-free. Nevertheless, exploiting the gravity by means of the pivoting ability in Section 3.6 the task becomes feasible. However, the *gripper* and *object pivoting* abilities, on their own, are not enough. To use this new potential with a higher degree of autonomy, it has to be combined with a motion planner that has the ability to exploit it.

The pivoting abilities can be kinematically represented as an additional *virtual* revolute joint in the robot kinematic chain, located between the fingers, that is able to reproduce the motion in Fig. 3.8. Such joint can not be treated as the others because it cannot move in any direction, it is actuated by the gravity torque and the control input (the grasp force) acts as a brake.

This Chapter presents two different approaches that solve the planning problem with the pivoting abilities presented in the previous chapter.

The first strategy is presented in Section 4.1 and it has been published in (Costanzo, Stelter, et al. 2020). It uses the gripper pivoting in all the planned trajectories to keep the grasped object in a vertical orientation. The slipping avoidance is used to ensure a robust grasp when the pivoting is not needed.

The second strategy is an enhanced version of the algorithm published in (Costanzo, De Maria, Lettera, et al. 2020) and it is presented in Section 4.2. This strategy uses both gripper and object pivoting and it generates a sequence of trajectories each one characterized by a control modality.

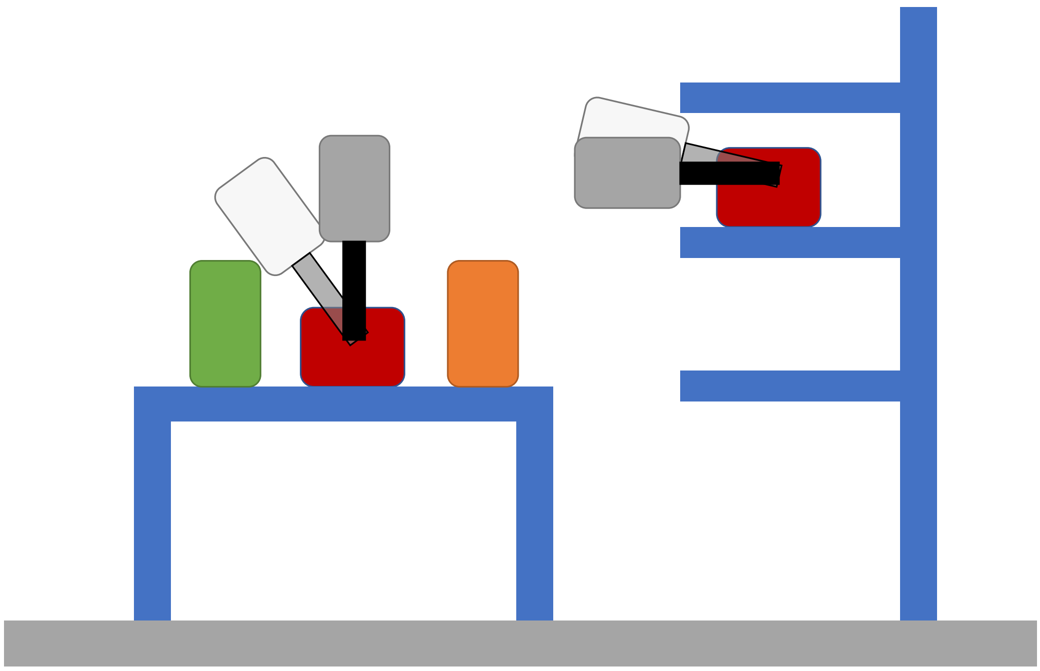

Figure 4.1: Schematic situation where gripper pivoting is mandatory to achieve the goal: reachable collision-free pick poses range between the two gripper poses on the left, while collision-free goal poses range between the two gripper poses on the right - no common fixed grasp exist.

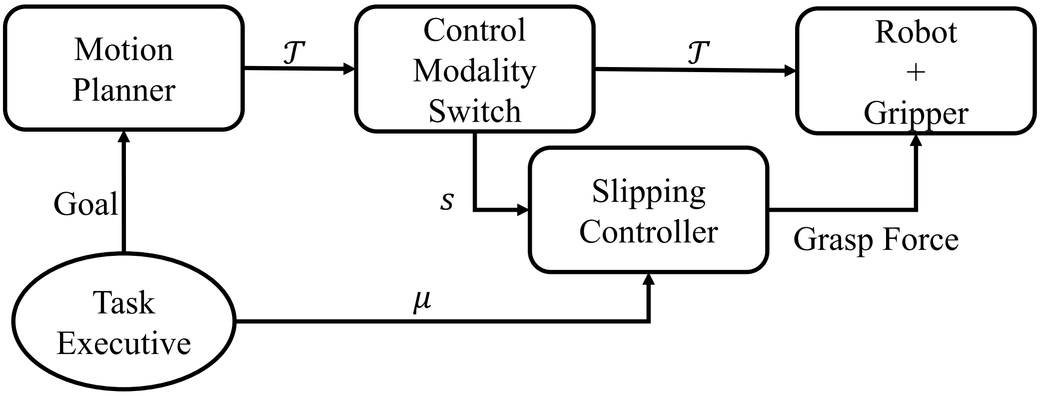

Figure 4.2: Block scheme of the gripper pivoting planner.

The two planners introduced before are simultaneously motion and manipulation planners because they simultaneously plan both the full arm motion and the in-hand manipulation maneuver.

Finally, Section 4.3 presents a higher-level task planner that solves complex pick-and-place problems by automatically choosing the pick grasp pose by using the motion/manipulation planner of Section 4.2.

4.1 Gripper Pivoting Planner

This section presents a motion/manipulation planning strategy that uses the *gripper pivoting* ability. Figure 4.2 shows the architecture of the integrated system.

The task executive sends goals to the motion planner, that are needed to accomplish the task (such as shelf replenishment in a supermarket scenario). As explained in Chapter 3 the only object-dependent parameter is the friction coefficient μ, thus this module has to access a knowledge base to fetch and set the friction coefficient for the slipping control module, given the object to handle.

The motion planner generates a joint space trajectory $\mathcal{T}$ that achieves the given goal utilizing the pivoting ability.

The control modality switch module post-processes the trajectory before sending it to the robot. While the trajectory is executed, the module sends commands s to the slipping controller to switch between the two control modalities, namely, *gripper pivoting* or *slipping avoidance*.

Slipping Controller Module

The Slipping controller module has been detailed in Chapter 3. In particular, the planner described in this section uses the slipping avoidance modality of Section 3.5 and the gripper pivoting modality of Section 3.6. Each modality corresponds to a particular algorithm that computes the desired grasp force, in particular, the slipping avoidance uses (3.50) and the gripper pivoting uses (3.54). To better distinguish the two modalities in this section, let call f_{nSA} and f_{nGP} the normal force computed by the slipping avoidance and gripper pivoting algorithms, respectively.

Motion Planner Module

The pivoting functionality is modeled by attaching the grasped object to the robot via a constrained virtual joint. A constraint sampling-based planner (Berenson et al. 2009) or trajectory optimization (Dragan, Ratliff, and Srinivasa 2011; Toussaint 2009) are standard choices. However, these approaches do not scale well with constraints that are too restricting. The motion planner used in (Fang, Bartels, and Beetz 2016) is well suited for this scenario, because, generally, only the number of constraints influences the run time. With this framework, motions are specified as a composition of constraints on joint velocities. The planner generates joint trajectories $\mathcal{T}$ for the robot which are executed in open loop.

The additional virtual pivoting joint adds an additional degree of freedom. During the planning, the pivoting is simulated by adding a high priority constraint to all goals that minimizes the angle between the gravity vector $\boldsymbol{g}$ and the vector pointing from the grasp point to the center of mass of the object $\boldsymbol{p}_g$

$$\cos^{-1}\left(\frac{\boldsymbol{p}_g^T\boldsymbol{g}}{\|\boldsymbol{p}_g\|\,\|\boldsymbol{g}\|}\right). \tag{4.1}$$

As a result, the grasped object is always vertical during the planning process. If the planner receives Cartesian goals for the grasped object, it will change the angle between the object and gripper to avoid collisions, while keeping the object vertical. In this way, the planner will automatically choose the relative grasp angle between the gripper and the object. Nevertheless, if a specific relative angle is required at the beginning or at the end of the trajectory, it is possible to add an additional constraint on the joint position of the virtual joint.

The motion planner avoids self and external collisions for all robot links, grasped object, and known environmental objects. For comparison, these motion planning problems have about 100 constraints. Most of them are

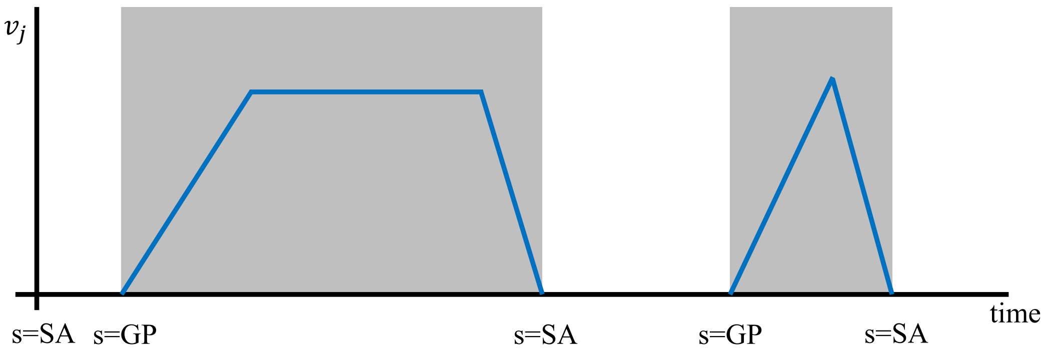

Figure 4.3: Example of timestamp selection for the modality switching. SA and GP represent the activation time of slipping avoidance and gripper pivoting respectively.

used for collision avoidance and the exact number depends on how many objects are close to the robot. To model the gripper pivoting, we need an additional free variable for the new joint as well as one constraint to enforce the vertical object orientation.

Control Modality Switch Module

When the gripper pivoting is active, the grasp force is low, just above the minimum grasp force that does not let the translational slip of the object, and the dynamic control action (3.51) is not active. To improve robustness, the gripper pivoting mode should only be active when needed. Thus, the control modality switch is a module that switches to slipping avoidance when the virtual joint is not used.

The module checks the velocity of the virtual joint against a threshold of 0.01 rad/s, selected to avoid switches due to numerical noise, and stores switching events with timestamps in a vector. A velocity below the threshold requires slipping avoidance, otherwise, the gripper pivoting is needed. The threshold generates a pivoting angle error smaller than the error due to the CoG position estimation; however, this error is recovered as soon as a new pivoting is triggered. The trajectory is then sent to the robot and the control modality switch starts listening to the joint state to synchronize itself with the actual robot motion. At each modality switch event, the module sends the corresponding command s to the slipping controller.

Figure 4.3 shows a conceptual example, v_j is the planned velocity of the virtual joint, SA and GP indicate the activation timestamps of the slipping avoidance and gripper pivoting respectively. In every plot of this section, a gray area indicates the time interval when the gripper pivoting mode is

Figure 4.4: Mobile manipulator used in the experiments.

active.

4.1.1 Experiments

The architecture described in this section is tested in a supermarket scenario for a shelf replenishment task. The robots need a large skill set to execute a fetch-and-place task in this environment because they have to operate in tight spaces and handle a variety of objects.

The experiments are carried out with a mobile manipulator, a Universal Robot UR5 mounted on a mobile omnidirectional base (see Fig. 4.4). The end effector is the same used in the experiments of Chapter 3, i.e., a WSG50 gripper equipped with the SUNTouch force/tactile sensor (Appendix B).

Four sets of experiments are described with the objects of Fig. 4.5. The first set evaluates the angle of the object during the pivoting; the second set evaluates the feasibility of a simple pick-and-place task with and without the pivoting; the third set is a complete pick-and-place experiment with different objects and obstacles; the fourth set is a sensitivity experiment with respect to the object-dependent friction parameter, μ.

Figure 4.5: Objects used in the experiments.

Reliability Experiment

The first experiment investigates the reliability of both slipping avoidance and gripper pivoting algorithms by performing motions while an object is being grasped. For the tests, we used object E placed into the gripper by hand. The initial angle between the object and the fingers was measured using a manual digital inclinometer. The angle ranged from -0.028 rad to 0.060 rad. The robot was then commanded to execute simple motions along and about the three axes of the tool frame. During all experiments, the modality switch is active. This means that the gripper pivoting mode is automatically activated only during the rotation about the pivot axis; all other motions are executed in the slipping avoidance mode.

The experiment was repeated 12 times, six with low acceleration, and six with high acceleration. Afterward, the final angle was measured again.

The robot motions (especially the fast ones) cause a reduction of the break-away force and torque. This experiment tests the reliability of the slipping control algorithm in such a situation.

Results are shown in Table 4.1. The robot never dropped the item, showing both that the modality switch occurs at the right time and that the slipping avoidance is effective. Deviations lower than 0.2 rad are acceptable for a large class of objects, while they are critical for objects that easily fall over when released (e.g., thin and tall ones).

Desk Experiment

This experiment tests the interplay between the motion planner and modality switch in simple pick-and-place tasks using fixed and non-fixed start/goal angles. The task consists of placing the object E of Fig. 4.5 on a desk by picking it from the floor with a given angle between the finger approach axis and the vertical direction. The experiment is first executed in a simulated environment using different desk heights and then on the real robot using a 0.72 m high desk.

Table 4.2 shows the results for a 0.2 m desk height in the simulated environment. Various experiments have been carried out with different start and goal angles between gripper and object. The values inside the table show the planning time measured in seconds. No value indicates that the motion planner was not able to find a solution. The last row and the last column are special cases: the start and/or goal angle is not specified and the planner is free to choose the angle, the value inside the parentheses is the angle chosen by the planner. Note that the values in the gray cells correspond to not using the gripper pivoting functionality because the start and goal angles are the same. The planner fails to find a solution in the first and the fifth rows because the robot is not able to grasp the object on the floor with these initial angles. The same happens in the case of the fifth column, because the robot is not able to place the object on the desk with that angle. From the difference between the gray and non gray cells, we can see that the added constraint and new free variable do not significantly increase the planning time. Instead, there is a high correlation between the planning time and length of the final trajectory. This explains why the cases where both angles are chosen by the motion planner are among the fastest.

Table 4.3 shows the results for a 1.31 m desk height in the simulated environment. In this case, no solution with fixed angles exists. The planner was able to find a solution only for a free goal angle (last column). No solution was found in the first and the fifth elements of the last column for the same reason as in the previous case.

The experiment is finally executed on the real robot with a 0.72 m desk

	Slow Motion	Fast Motion
Mean Deviation	0.104 rad	0.112 rad
Maximum Deviation	0.181 rad	0.194 rad

Table 4.1: Mean and maximum deviations for 12 repetitions of the reliability experiment.

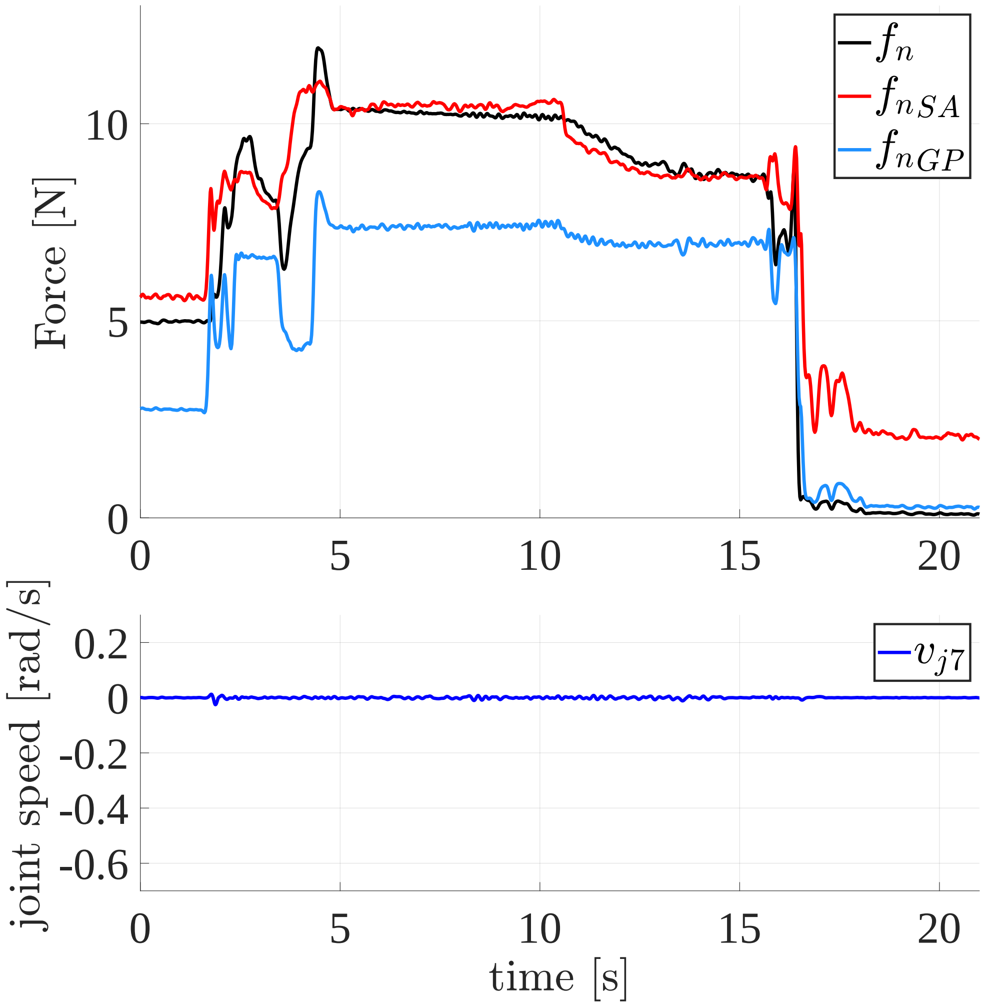

Figure 4.6: Desk experiment. The desired start and goal angles are both equal to $-\pi/4$. The top plot shows the actual grasp force (black), the slipping avoidance grasp force (red) and the grasp force needed for gripper pivoting (light blue). The bottom plot reports the joint velocity of the virtual joint.

α_s \ α_g	$-\pi/2$	$-\pi/4$	0.0	$\pi/4$	$\pi/2$	(-0.78)
$-\pi/2$	-	-	-	-	-	-
$-\pi/4$	14.3	12	11.1	12.4	-	11.9
0.0	11.8	10.4	9.1	10.4	-	10.1
$\pi/4$	13.8	12.5	10.4	11.8	-	12.2
$\pi/2$	-	-	-	-	-	-
(0.35)	12.1	9.9	9.3	10	-	9.9

Table 4.2: Planning times (in seconds) of the desk experiment in simulation: table height 0.2 m. Start (α_s) and goal (α_g) angles (radian) in parentheses are automatically chosen by the planner while the others are specified by the user. An angle of 0 corresponds to a vertical gripper orientation. Missing table entries correspond to planning requests failed due to collisions. Gray cells are options that are possible without the gripper pivoting since they correspond to equal start and goal angles.

height. The results are shown in Tab. 4.4. Figure 4.6 shows a case in which the start and goal angles are the same, thus no pivoting is needed. The top plot shows the grasp force computed by the slipping avoidance algorithm f_{nSA}, the grasp force needed for the gripper pivoting f_{nGP}, and the actuated measured grasp force f_n. The bottom plot shows the velocity of the virtual joint v_{j7}. Note that in this case no gripper pivoting is needed because the velocity is almost zero, thus f_n follows f_{nSA} and not f_{nGP}. In the last part of the plot, around 16 s, the forces drop because the object is released.

Figure 4.7 shows the case in which the planner automatically chose the start and goal angles. In this case, the velocity of the virtual joint is different from zero and the pivoting is needed. The gray area highlights the time interval when the gripper pivoting is active, and in this case, f_n follows f_{nGP}.

Shelf Experiment

The third experiment tests the whole algorithm in a complex real case scenario where the gripper pivoting ability may be mandatory due to obstacle positions.

We consider a shelf replenishment task: objects A-D, depicted in Fig. 4.5, were chosen for their variety in weight and surface properties and are picked up from the floor and placed on different layers on a shelf system. The experiment is first executed in simulation. The same combinations of start

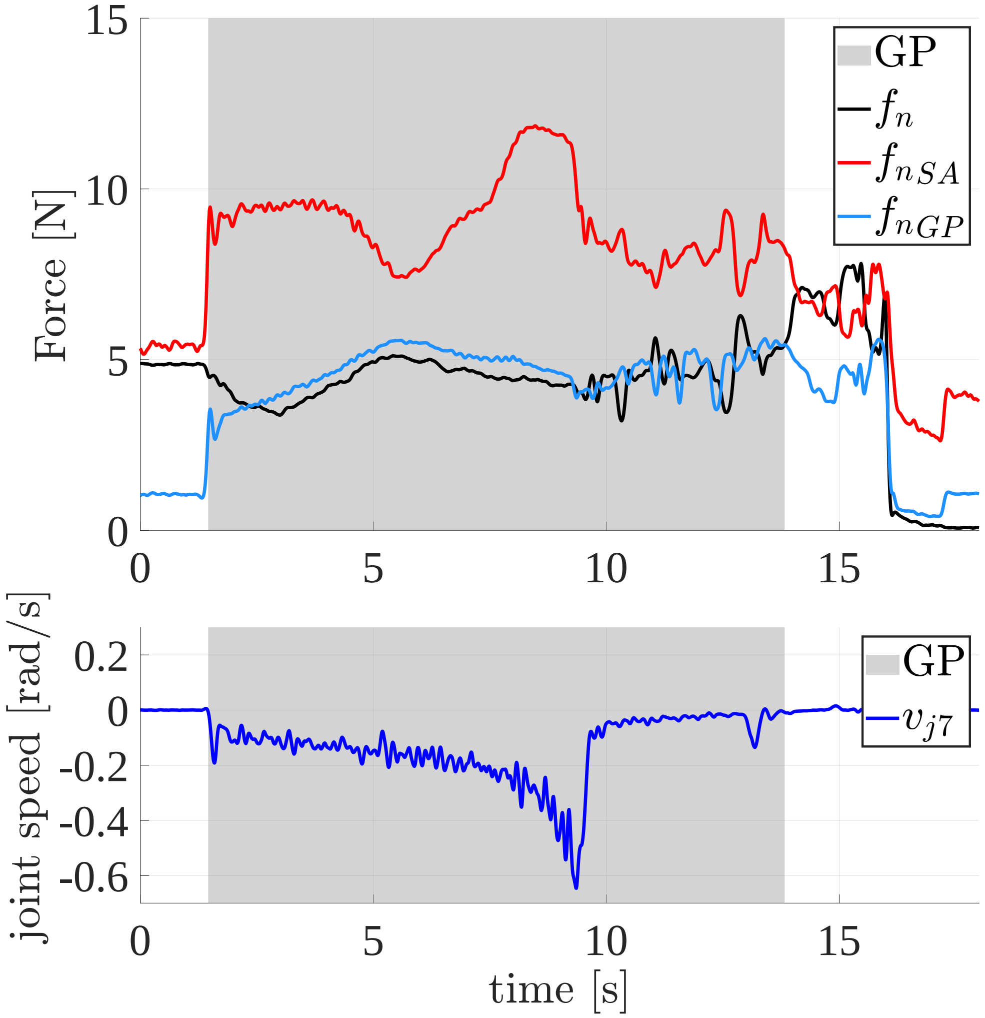

Figure 4.7: Desk experiment. Both the initial and final angles are chosen by the planner and are 0.35 rad and −1.38 rad respectively. The gray area represents the time interval where the gripper pivoting is active.

α_s \ α_g	$-\pi/2$	$-\pi/4$	0.0	$\pi/4$	$\pi/2$	(-1.76)
$-\pi/2$	-	-	-	-	-	-
$-\pi/4$	-	-	-	-	-	17.9
0.0	-	-	-	-	-	16.7
$\pi/4$	-	-	-	-	-	18.1
$\pi/2$	-	-	-	-	-	-
(0.35)	-	-	-	-	-	17

Table 4.3: Planning times (in seconds) of the desk experiment in simulation for different start and goal angle combinations: table height of 1.31 m.

α_s \ α_g	$-\pi/2$	$-\pi/4$	0.0	$\pi/4$	$\pi/2$	(-1.38)
$-\pi/2$	-	-	-	-	-	-
$-\pi/4$	12.8	13.5	14	-	-	13.5
0.0	11	11.8	12.6	-	-	12
$\pi/4$	13.9	14.2	13.9	-	-	13.6
$\pi/2$	-	-	-	-	-	-
(0.35)	11.3	11.7	12.1	-	-	11.6

Table 4.4: Planning times (in seconds) of the desk experiment for different start and goal angle combinations.

and goal angles as in the previous experiment are tested, but the proximity of shelves greatly decreases the number of possible goal angles. The results are shown in Table 4.5. Rows and columns that failed for all shelves are omitted to save space. The gripper pivoting proved very useful in this scenario, because the planner only found solutions for fixed angles on two shelves and only for one angle. On the shelf at height 0.6 m, the shelf above is too close and the shelf at 1.31 m is too high for that configuration.

The experiment is executed with the real robot for the case of free start and goal angles and can be seen in the accompanying video (Appendix D.1). Fig. 4.8 shows the shelf filled at the end of the experiment. Fig. 4.9 shows a plot of the forces and virtual joint speed when object A is placed on the bottom shelf. The start and goal angles chosen by the planner are 0.16 rad and -0.95 rad respectively. In the figure as well as the video it is clear that the pivoting is activated in two phases, after the lift to reach the shelf and inside the shelf to avoid collisions.

α_s \ α_g	shelf at 0.2 m			shelf at 0.6 m		
	$-\pi/2$	$-\pi/4$	(-0.95)	$-\pi/2$	$-\pi/4$	(-1.38)
$-\pi/4$	20.5	18.3	22.1	17.7	-	18.9
0.0	23.5	19	21.1	18.5	-	17.9
(0.16)	23.2	19.7	22.3	17.1	-	18.7
α_s \ α_g	shelf at 0.93 m			shelf at 1.31 m		
	$-\pi/2$	$-\pi/4$	(-1.58)	$-\pi/2$	$-\pi/4$	(-1.82)
$-\pi/4$	-	22.5	21.5	-	-	25.5
0.0	20.8	21.7	19.9	-	-	24.1
(0.16)	20.2	21.7	21.1	-	-	25.5

Table 4.5: Planning times (in seconds) of the shelf experiment for different start and goal angle combinations.

Figure 4.8: Shelf filled with objects at the end of the experiment. See the accompanying video in Appendix D.1

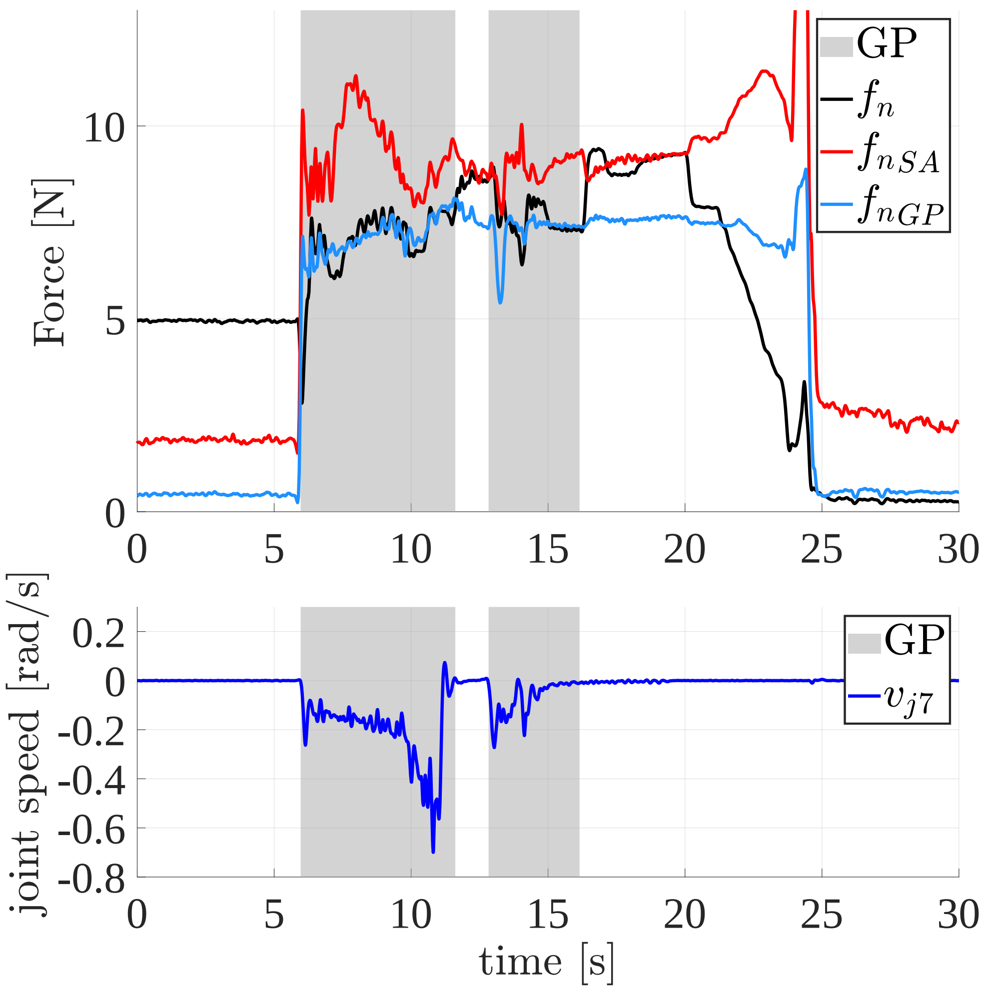

Figure 4.9: Shelf experiment. In this case the object A is placed on the bottom shelf. Note the gray areas where the planner activates the gripper pivoting mode. See the accompanying video in Appendix D.1

Sensitivity Experiment

To assess the sensitivity of the algorithm to the friction coefficient, the last experiment has been repeated with different values of μ. In particular, for object B, instead of the estimated value 0.9, an underestimated one has been used, i.e., 0.25 (that means about 72% of underestimation). The result is a failure of the task because the gripper pivoting was not executed properly, such that the object did not rotate and fell over. Values higher than 0.25 did not result in a failure. That means that the pivoting algorithm is quite robust against underestimated values for μ, at least when the effect of the torsional moment dominates the effect of the tangential force, i.e., when the grasp point is far from the CoG, as for object B. Finally, the placing of object D was repeated with 0.85. That equals to a 18% overestimation with respect to 0.72, which was estimated for that object. This resulted in a grasping force that was too low, making the object slip out of the fingers. This can be deduced by Fig. 4.10, where the grasp force suddenly goes to zero at about 13 s. Both failures are reported in the accompanying video (Appendix D.1).

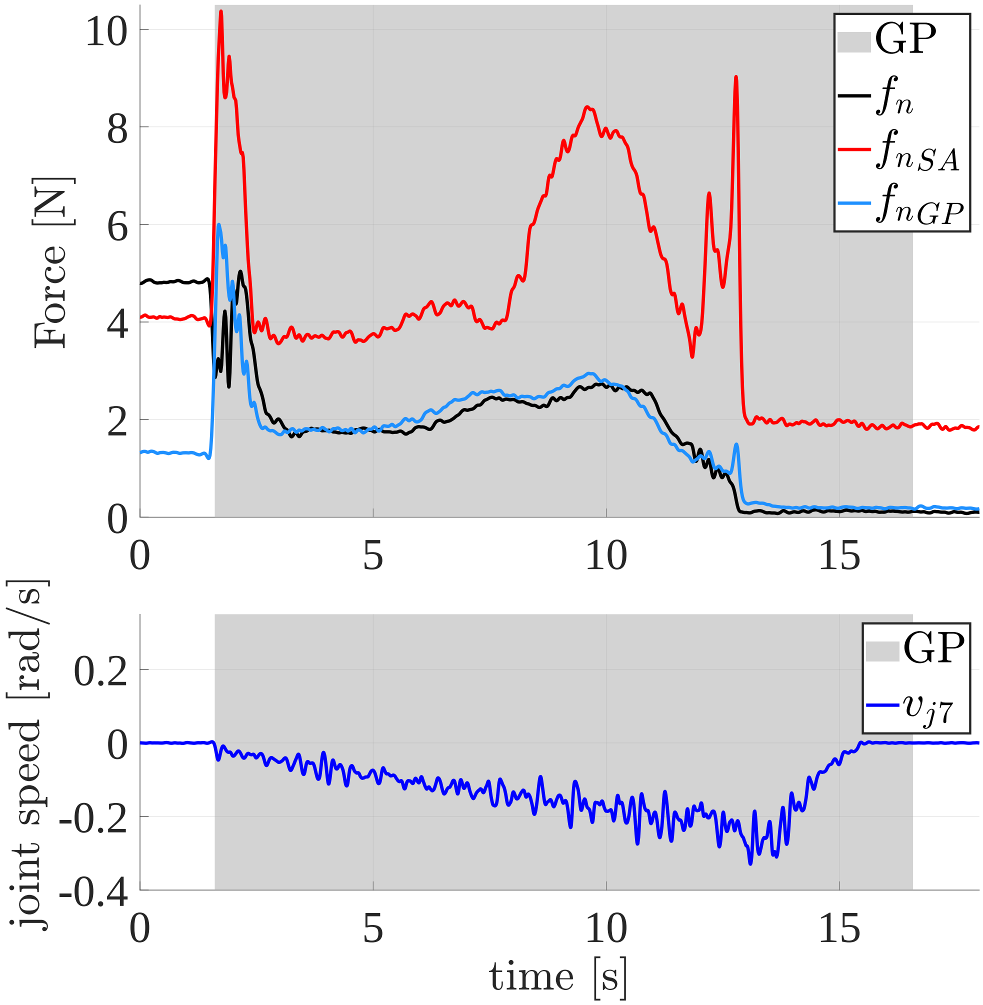

Figure 4.10: Shelf experiment. The pick and place of object D is repeated with an overestimated friction coefficient.

4.2 Manipulation Planner

The approach in the previous section is feasible only if the final object orientation is vertical because such constraint is active in the whole trajectory. This section presents an alternative motion/manipulation planning strategy. It has been designed to automatically choose the slipping control modality in specific segments of the planned trajectory. Moreover, this strategy allows us to execute the *object pivoting* maneuver by combining vertical object pivoting and gripper pivoting, as explained in Section 3.6.2 and depicted in Fig. 3.9. Nevertheless, this approach is not able to generate the same trajectories of Section 4.1 because, during the pivoting, the robot is constrained to not translationally move the end effector but just rotate it, moreover, the pivoting cannot take place during end effector translations.

The considered scenario is similar to the one depicted in Fig. 4.11. With reference to the top-left image, suppose that for some reason the robot had to pick the object with that grasp configuration (e.g., to avoid collisions or to reach the object location inside its workspace) and it has to place it on the lower shelf layer with the same orientation. It is obvious that with a fixed grasp the planner cannot find any feasible solution due to the collision with the top layer. The availability of changing the gripper orientation without changing the object pose (gripper pivoting) allows the motion planner to find the solution whose final configuration is depicted in the top right picture. Similarly, with reference to the image on the middle left, suppose the robot has to pick the bottle placed horizontally on the table and has to place it vertically on the top layer as shown in the middle right image. Again, a fixed grasp solution is unfeasible while an object pivoting maneuver allows the robot to accomplish the task. In the last scenario of the bottom pictures, the robot has again to pick the bottle horizontally placed on the table to place it in between two bottles already placed on the same shelf layer on two adjacent facings. To avoid collisions with such objects the bottle has to be placed with a given angle with respect to the vertical direction. Thus, the planner has to execute an object pivoting to re-orient the object with respect to the gripper again exploiting the controlled sliding feature of the grasp control, the object pivoting is decomposed as the sequence of robot motions depicted in Fig. 3.9.

The proposed motion/manipulation planner is built directly on top of the MoveIt! framework (Chitta, Sucan, and Cousins 2012), which uses the Open Motion Planning Library (OMPL) (Kingston, Moll, and Kavraki 2017; Sucan, Moll, and Kavraki 2012) that implements randomized motion planners. The default Kinematics and Dynamics Library (KDL) (Nilsson 2009) kinematic solver has been replaced with Trac-IK (Beeson and Ames 2015), which

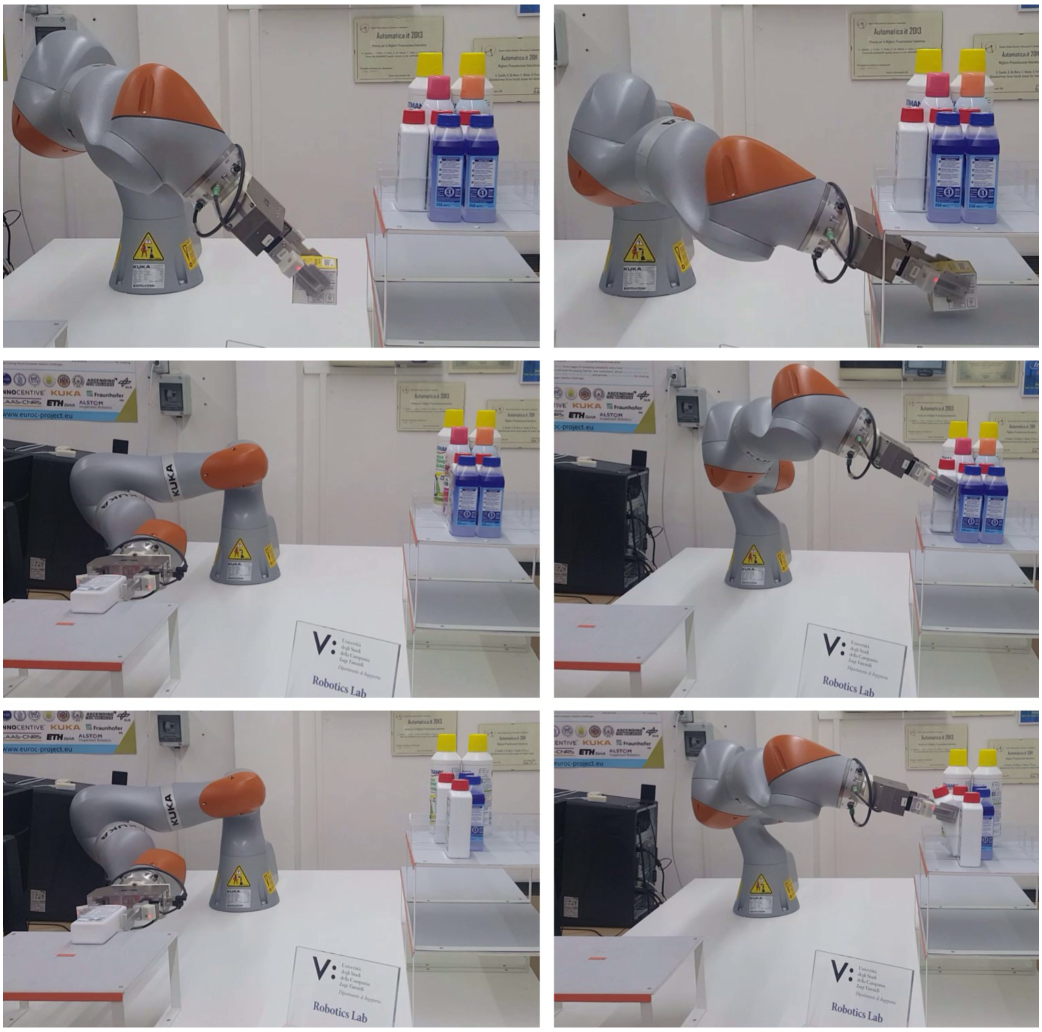

Figure 4.11: Three sample scenarios: grasping configurations before (left) and after (right) controlled sliding maneuvers necessary to achieve the goal object pose without collisions.

merges a simple extension to KDL's Newton-based convergence algorithm with an efficient Sequential Quadratic Programming (SQP) constrained non-linear optimization approach.

Also in this approach, the pivoting is modeled as an additional rotational joint along the grasp axis between the last end-effector link and the grasped object. Two robot kinematic models are defined, r_s is the standard one, and r_v is the augmented kinematic model that includes the virtual pivoting joint.

At every planning request, the motion planner tries to plan without using the additional joint (i.e., using the standard kinematic model r_s) and only if the request cannot be satisfied (e.g., in presence of collisions) it attempts to find a solution with the virtual joint (using the augmented kinematic model r_v), i.e., executing a pivoting maneuver. The latter solution allows the planner to change the angle between object and gripper in complex scenarios, e.g., when the object has to be inserted in narrow spaces and/or when a specific place angle is required.

Obviously, using r_v makes sense only if an object is actually grasped. If the object is not attached to the gripper (e.g., in the pre-grasp phase), there is no reason to plan using the augmented kinematic model. Moreover, the pivoting maneuver must be possible, i.e., the object must be grasped far enough the CoG (the choice of the grasp pose will be faced in Section 4.3).

The input of the algorithm is the initial robot configuration $\boldsymbol{q}_0$, the desired object pose $\boldsymbol{T}_d^b$ with reference to the base frame $\{b\}$, the robot standard kinematic model r_s and the augmented one r_v, optionally it is possible to provide path constraints c_t.

The output of the algorithm is a sequence of motion trajectories

$$\mathcal{Q}_r = \{\boldsymbol{q}_{r_1}(t),\, \dots,\, \boldsymbol{q}_{r_N}(t)\} \tag{4.2}$$

with $\boldsymbol{q}_{r_i}(t) \in \mathbb{R}^n$ being n the number of robot joints, and a vector of gripper control modalities

$$\mathcal{M}_r = (m_{r_1},\, \dots,\, m_{r_N}), \tag{4.3}$$

where $m_{r_i} = 0$ means that the slipping avoidance control should be active (fixed grasp) and $m_{r_i} = 1$ corresponds to the controlled sliding modality (pivoting). The length $N \in \{1, 2\}$ is automatically selected by the algorithm depending on the scene as will be explained below.

The pivoting is intended as a combination of *vertical object pivoting* (Section 3.6.1) and *gripper pivoting* (Section 3.6.2) that brings and keeps the object in a vertical orientation. In fact, as explained in Section 3.6.2, at the end of the vertical pivoting maneuver the applied force and the object orientation are the same required for the gripper pivoting, thus it is possible to combine the two maneuvers in the same slipping control modality. If the robot does not move, the motion will correspond to a vertical object pivoting; if the object is already vertical, it will correspond to a gripper pivoting; otherwise, the motion will be a combination of the two maneuvers. In any case, the slipping control algorithm will be the same, i.e., reducing the grasp force from its current value to the value in (3.54).

Algorithm 1: PivotingPlan

Input: $\boldsymbol{q}_0$, $\boldsymbol{T}_d^b$, r_s, r_v, c_t
Output: $\mathcal{Q}_r = \{\boldsymbol{q}_{r_1}(t), \dots, \boldsymbol{q}_{r_N}(t)\}$ and $\mathcal{M}_r = (m_{r_1}, \dots, m_{r_N})$
Function `PivotingPlan(`$\boldsymbol{q}_0, \boldsymbol{T}_d^b, r_s, r_v, c_t$`)`**:**
  initialization;
  n = $\boldsymbol{q}_0$`.size()`;
  $\tilde{\boldsymbol{q}}_0 = \left[\boldsymbol{q}_0^T, 0\right]^T$;
  [$\boldsymbol{q}_p(t)$, success] = `plan(`$\tilde{\boldsymbol{q}}_0$, $\boldsymbol{T}_d^b$, `'obj'`, c_t, r_s`)`;
  if *success* **then**
    N=1; $\boldsymbol{q}_{r_1}(t) = \boldsymbol{q}_p(t)$; $m_{r_1} = 0$;
    return;
  end
  $\tilde{\boldsymbol{q}}_0$`.end()` = `vertical_object_pivoting(`$\cdot$`)`;
  [$\boldsymbol{q}_p(t)$, success] = `plan(`$\tilde{\boldsymbol{q}}_0$, $\boldsymbol{T}_d^b$, `'obj'`, c_t, r_s`)`;
  if *success* **then**
    N=2; $\boldsymbol{q}_{r_1}(t) = \boldsymbol{q}_0$; $m_{r_1} = 1$; $\boldsymbol{q}_{r_2}(t) = \boldsymbol{q}_p(t)$; $m_{r_1} = 0$;
    return;
  end
  N=2;
  $\boldsymbol{q}_p(t)$ = `plan(`$\tilde{\boldsymbol{q}}_0$, $\boldsymbol{T}_d^b$, `'obj'`, c_t, r_v`)`;
  $\boldsymbol{q}_v = \boldsymbol{q}_p(t)$`.end()`;
  c_p = `add_piv_constraint(`c_t`)`;
  T_g^b = `combine_orientations(`$\tilde{\boldsymbol{q}}_0$, $\boldsymbol{q}_v$`)`;
  $\boldsymbol{q}_{r_1}(t)$ = `plan(`$\tilde{\boldsymbol{q}}_0$, $\boldsymbol{T}_g^b$, `'grip'`, c_p, r_s`)`;
  $m_{r_1} = 1$; $\tilde{\boldsymbol{q}}_0$`.slice(`*0*,*n*`)` = $\boldsymbol{q}_{r_1}(t)$`.end()`;
  $\boldsymbol{q}_{r_2}(t)$ = `plan(`$\tilde{\boldsymbol{q}}_0$, $\boldsymbol{T}_d^b$, `'obj'`, c_t, r_s`)`;
  $m_{r_2} = 0$;
  return;

Algorithm 1 shows a C++ like pseudo-code of the pivoting planning algorithm. All the algorithm is executed offline in a simulated environment and then the resulting robot trajectory is executed in open-loop. Note that the input is $\boldsymbol{q}_0 \in \mathbb{R}^n$, but the state of the augmented model has $n+1$ joints. The first thing to do is to define an augmented initial configuration as $\tilde{\boldsymbol{q}}_0 = \left[\boldsymbol{q}_0^T, 0\right]^T \in \mathbb{R}^{n+1}$ that is the $\boldsymbol{q}_0$ vector with an extra 0 at the end, this represents the initial value of the pivoting joint (line 4).

In the algorithm, the function `plan` internally calls the low-level planner (MoveIt!) and the represented interface takes as input the full initial configuration of the augmented kinematic model (i.e., $n+1$ joints), the desired pose, a string that can be `'obj'` or `'grip'` if the desired pose is the target pose of the object or the gripper respectively, the path constraints (that may be possibly void) and the kinematic model to use during the planning. The full initial configuration is needed to describe the initial state of all the manipulator (including the pivoting joint), but the virtual pivoting joint is effectively used during the plan only if the augmented kinematic model r_v is passed as input, otherwise, the pivoting joint is kept fixed during the plan. The output of `plan` is the planned joint trajectory and a success flag that indicates if the plan was successful or not. To simplify the notation, a missing output success flag means that the whole pivoting planning algorithm is aborted in case of no success of the `plan` function.

The planner first tries to execute a standard plan (without the pivoting joint), if the plan is successful (line 6), the number of the output trajectories is $N = 1$, the unique trajectory $\boldsymbol{q}_{r_1}(t)$ is the result of the standard plan and the corresponding slipping control modality is slipping avoidance ($m_{r_1} = 0$).

If the standard plan fails, the pivoting modality is activated. On the real robot, the pivoting activation will result in a vertical object pivoting, thus, in this phase, the planning algorithm simulates the pivoting by setting the pivoting joint to a value such that the object in the simulated environment is vertical, this is done by the function `vertical_object_pivoting` (line 10). After the simulated pivoting, the planner tries again the standard plan (using r_s). This time the plan may be successful because the initial augmented configuration $\tilde{\boldsymbol{q}}_0$ has changed and now the object is in a vertical orientation. If the plan is successful, the number of the output trajectories is $N = 2$, the first trajectory just requires to keep the robot in the initial configuration ($\boldsymbol{q}_{r_1}(t) = q_0$) while the vertical object pivoting is executed, the corresponding slipping control modality is pivoting ($m_{r_1} = 1$). The execution of this trajectory results in a vertical object pivoting. The second trajectory $\boldsymbol{q}_{r_2}(t)$ is a slipping avoidance one ($m_{r_2} = 0$) corresponding to the last planning result.

If also the last attempt fails, a further change of the relative angle between the gripper and the object is needed. This can be achieved with a gripper pivoting. The first step is to find a feasible relative orientation between the gripper and the object; to do that a trajectory with target $\boldsymbol{T}_d^b$ is planned by using the augmented kinematic model r_v (line 17), note that this trajectory cannot be executed on the real robot because there is no constraint on the feasibility of the pivoting joint motion. The last trajectory point of the last plan contains the information about the feasible relative angle, thus it is stored as $\boldsymbol{q}_v$ (line 18). The gripper pivoting that is about to be performed has an additional constraint, the grasp point absolute position has to remain fixed, thus, the pivoting constraint c_p is defined by adding this condition to the input constraints c_t (line 19). The next objective is to achieve the feasible relative angle between gripper and object found in the plan at line 17 and encoded in the configuration $\boldsymbol{q}_v$. To do so, the function `combine_orientations` at line 20 computes a desired absolute gripper pose $\boldsymbol{T}_g^b$ that has the same initial position and an orientation such that the relative angle between the gripper and the object is the feasible one. This target orientation $\boldsymbol{R}_g^b$ is computed by combining the object orientation in $\tilde{\boldsymbol{q}}_0$ (namely, $\boldsymbol{R}_o^b(\tilde{\boldsymbol{q}}_0)$) and the relative gripper/object orientation in $\boldsymbol{q}_v$ (namely, $\boldsymbol{R}_g^o(\boldsymbol{q}_v)$)

$$\boldsymbol{R}_g^b = \boldsymbol{R}_o^b(\tilde{\boldsymbol{q}}_0)\boldsymbol{R}_g^o(\boldsymbol{q}_v). \tag{4.4}$$

$\boldsymbol{q}_{r_1}(t)$ (line 21) is the trajectory that brings the gripper in the pose $\boldsymbol{T}_g^b$ and it corresponds to a gripper pivoting mode (note that $\boldsymbol{T}_g^b$ is a gripper target pose, thus, `plan` in the pseudo-code is called with the `'grip'` argument). Finally, with a feasible relative angle between gripper and object, it is possible to execute a standard plan in a fixed grasp mode to bring the object to the desired pose $\boldsymbol{T}_d^b$.

To execute a complete pick and place task, the presented pivoting planner has to be called several times to execute various motion segments, e.g., pre-grasp, grasp, lift, pre-place, place, retrait. The goal of each segment as well as the grasp pose should be decided by the programmer or by a higher-level planner. The choice of the grasp pose will be faced in Section 4.3. Note that, the presented pivoting planner makes sense only if an object is actually grasped, thus, in all the motion segments before the grasp and after the place, the standard plan should be used (in other words the algorithm should abort if no solution is found at line 5).

4.2.1 Experiments

The algorithm is tested in an in-store logistic scenario with situations similar to those depicted in Fig. 4.11, where a solution with a fixed grasp does not exist. Note that, as already stated, a complete pick and place task requires a higher level planner that decides the complete motion sequence, e.g., pick → lift → pre-place → place. Section 4.3 will propose a task planner to solve this issue that uses the manipulation planner of this section as lower-level planner and Section 4.4 will present a set of experiments that proves

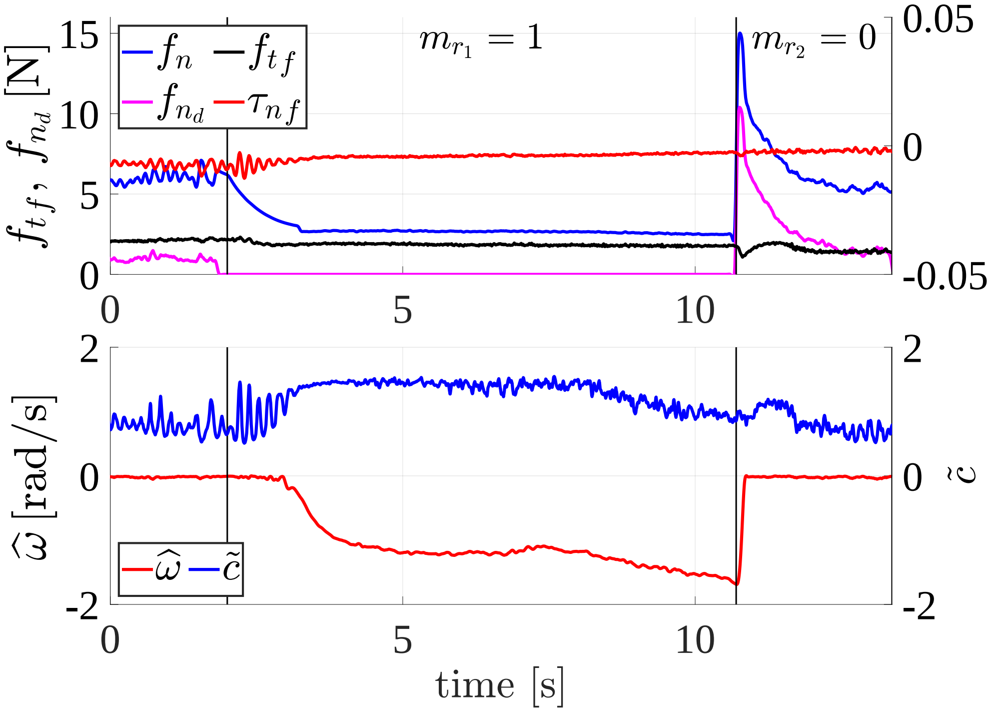

Figure 4.12: Experiment that tests the manipulation planner. The top plot shows, on the right axis, the friction torque (red), and, on the left axis, the tangential friction force (black); the dynamic contribution of the slipping avoidance algorithm (magenta); the commanded normal force (blue). The bottom plot shows the estimated normalized center of rotation (blue line right axis) and the slipping velocity about the CoR estimated by the observer (red line left axis).

the effectiveness of both task and manipulation planners. To avoid useless repetition, this experiment section presents just the iconic case depicted in Fig. 4.11-top where the object is already grasped as in the left figure and the robot has to place it in the narrow space between two shelves. The reader will find in Section 4.4 a more exhaustive set of experiments.

As in the other experiments of this thesis, the robot knows just the object friction coefficient μ and not its weight. In this case the algorithm plans two trajectories ($N = 2$), the first one $\boldsymbol{q}_{r_1}(t)$ is a gripper pivoting maneuver ($m_{r_1} = 1$) that changes the relative orientation between the gripper and the object, and the second one $\boldsymbol{q}_{r_2}(t)$ is a simple motion to the place pose with a fixed grasp in slipping avoidance mode ($m_{r_2} = 0$).

This is evident in Fig. 4.12 that shows the execution phase. The top plot shows the measured tangential friction force and torque, f_{tf} and τ_{nf} respectively; the dynamic contribution f_{n_d} of the slipping avoidance algorithm computed as explained in Section 3.5; and the total commanded normal force f_n. Recall that, in the slipping avoidance mode ($m_{r_i} = 0$), f_n is the superposition of static and dynamic contributions (Section 3.5), instead, in the pivoting mode, it gradually goes towards the value in (3.54) described in Section 3.6. The bottom plot shows the angular slipping velocity $\widehat{\omega}$ about the CoR axis estimated by the observer in Section 3.4 and the normalized CoR position $\tilde{c}$ computed by the algorithm in (2.80).

At the beginning, the robot is in a configuration similar to the one in Fig. 4.11-top-left. The initial control modality is the slipping avoidance one, thus, the dynamic contribution is activated and the observed velocity is almost zero.

At about 2 s the first trajectory $\boldsymbol{q}_{r_1}(t)$ is executed in pivoting mode ($m_{r_1} = 1$) and the relative orientation between the gripper and the object changes. This can be noticed in the estimated velocity $\widehat{\omega}$ in Fig. 4.12-bottom.

At about 10.5 s the second trajectory $\boldsymbol{q}_{r_2}(t)$ is executed in slipping avoidance mode ($m_{r_2} = 0$). The dynamic contribution is reactivated and it generates a peak that brings the observed velocity to zero and stops the sliding. At this moment the relative angular position between the gripper and the object has changed and the robot can take the object to the final pose.

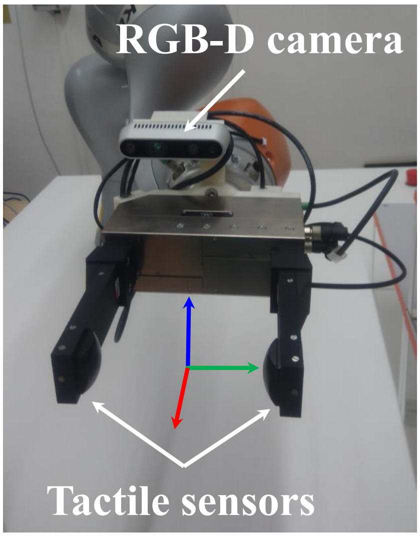

Figure 4.13: Robot end effector equipped with Intel D435i RGB-D camera and WSG-50 gripper with the SUNTouch tactile sensors installed. The grasp frame is depicted with the RGB labeling convention.

4.3 Task and Grasp Planner

This section presents a task and grasp planner built on top of the pivoting planner presented in Section 4.2. The scenario is similar to the one in Section 4.2, but now the task/grasp planner uses the pivoting planner to automatically choose the motion segments and the grasp pose by picking them from a given set stored in a database. The robot has to pick the object from a picking tray and automatically place it on its dedicated facing slot. Moreover, it is available only a rough estimation of the initial object pose with some uncertainty. The estimated object pose is adjusted online during the execution (in the pre-grasp phase) by a visual servoing algorithm that exploits an eye in-hand camera mounted on the robot end effector (see Fig. 4.13).

A database stores the information about the objects. For each object in the given set, a set of possible grasp poses referred to a frame fixed to the object is defined. For each grasp pose, a pre-grasp pose is defined that will be the target of the visual servoing algorithm.

Figure 4.14 shows the architecture of the whole system. The task/grasp planner calls various times the motion planner module of Section 4.2 and receives various planning results $\mathcal{R}_i$ that contains both the planned trajectory and the slipping control modality. Basing on the motion planner results, the task planner decides the whole pick-and-place motion (and thus also

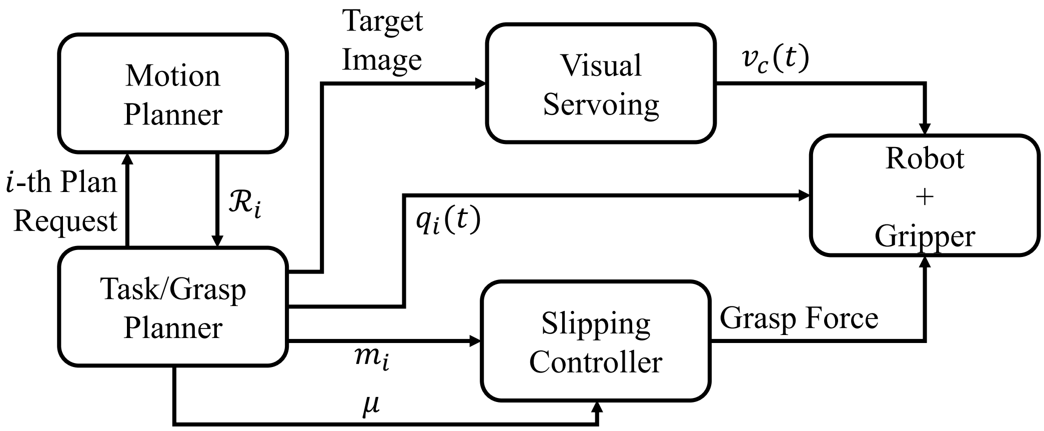

Figure 4.14: Block scheme of the whole system.

the grasp pose). During the execution phase, the task planner sends the correct control modality command m_i to the slipping controller algorithm of Chapter 3 and, at the same time, sends the trajectory commands to the robot driver. When needed, the visual servoing module is activated with a target image; the output of the visual servoing algorithm is a velocity command in the Cartesian space.

To describe the whole planning pipeline, the following reference frames, defined through the corresponding homogeneous transformation matrix, are introduced:

- $\boldsymbol{T}_j^b$ is the true pose of the frame fixed to object j with respect to the base frame while $\widehat{\boldsymbol{T}}_j^b$ is its available estimation.

- $\boldsymbol{T}_{g_i}^j$ is the pose of the ith grasp frame with $i = 1, \ldots, k_j$, i.e., a possible grasp frame referred to the frame fixed to object j; note that such frames are selected by the programmer and stored in the object database beforehand based on the maximum grasping force that the gripper can exert.

- $\boldsymbol{T}_{v_l}^j$ is the pose of the lth pre-grasp frame with $l = 1, \ldots, h_j$ with respect to the frame fixed to object j; these frames are the poses where the robot end effector, carrying the camera, should go before approaching the object and they are selected at a distance from the object compatible with the field of view of the camera (see Fig. 4.13). In fact, these poses are selected so that the object is clearly visible from the eye-in-hand camera used for the visual servoing control loop (see also Section 4.3.1).

- $\boldsymbol{T}_l^b$ is the pose of the end effector after the lifting phase, which is a translation of the pose $\widehat{\boldsymbol{T}}_{g_j}^b$ along the z axis of the base frame upward, so as to lift the grasped object far from the picking tray.
- $\boldsymbol{T}_{t_j}^b$ is the pose of the target frame where the object j has to be placed;
- $\boldsymbol{T}_{pt_j}^b$ is the pose of the pre-target frame of object j defined as a simple translation along the negative direction of the z and y axes of the grasp frame of a certain offset from the target frame.

Note that a pre-grasp frame $\boldsymbol{T}_{v_l}^j$ is associated with each grasp frame $\boldsymbol{T}_{g_i}^j$ but not vice versa, and a desired object j image is associated to each pre-grasp frame, that is the reference image for the image-based visual servoing controller described in Section 4.3.1.

Given one grasp pose $\boldsymbol{T}_{g_i}^j$ in the grasp pose set of object j, the sequence of planning requests sent to the pivoting planner is the following

$$\boldsymbol{q}_0 \xrightarrow{\mathcal{R}_1} \widehat{\boldsymbol{T}}_j^b \boldsymbol{T}_{v_l}^j \xrightarrow{\mathcal{R}_2} \widehat{\boldsymbol{T}}_j^b \boldsymbol{T}_{g_i}^j \xrightarrow{\mathcal{R}_3} \boldsymbol{T}_l^b \xrightarrow{\mathcal{R}_4} \boldsymbol{T}_{pt_j}^b \xrightarrow{\mathcal{R}_5} \boldsymbol{T}_{t_j}^b \tag{4.5}$$

The result $\mathcal{R}_i$ of the generic planning request contains both a sequence of joint space trajectory $\{\boldsymbol{q}_{i_1}(t), ..., \boldsymbol{q}_{i_N}(t)\}$ that satisfies all constraints (mainly absence of collisions) and the corresponding control modality flag sequence $\{m_{i_1}, ..., m_{i_N}\}$ for the slipping control module. N can be either 1 or 2 if the planning result is a standard or a pivoting maneuver, respectively (see Section 4.2). It is important to recall that the sequence $\{\mathcal{R}_1, ..., \mathcal{R}_5\}$ is simply a plan that will not be executed as it is. In fact, the plan uses the rough object pose $\widehat{\boldsymbol{T}}_j^b$ that may differ from the real one. The actual execution phase is described in Section 4.3.2.

The planning result $\mathcal{R}_1$ simply generates the motion trajectory to bring the robot from the initial configuration $\boldsymbol{q}_0$ to the rough pre-grasp pose $\widehat{\boldsymbol{T}}_j^b \boldsymbol{T}_{v_l}^j$ and the control modality is a pure position control. Note that the pre-grasp pose is the one associated with the selected grasp pose $\boldsymbol{T}_{g_i}^j$.

The result $\mathcal{R}_2$ brings the robot to the rough grasp pose $\widehat{\boldsymbol{T}}_j^b \boldsymbol{T}_{g_i}^j$.

The result $\mathcal{R}_3$ lifts the object taking it far from the picking tray in the upward direction in the pose $\boldsymbol{T}_l^b$. It is the first motion segment with the object effectively grasped, so it could be possibly executed with the pivoting planner in Section 4.2. Nevertheless, this motion is forced to be planned in slipping avoidance mode. This is because the uncertainly on the rough object pose $\widehat{\boldsymbol{T}}_j^b$ does not permit to execute $\mathcal{R}_3$ as it is, this will be clearer in Section 4.3.2.

The planning results $\mathcal{R}_4$ and $\mathcal{R}_5$ bring the object to the pre-place and place pose, respectively. They exploit the full pivoting planner presented in Section 4.2.

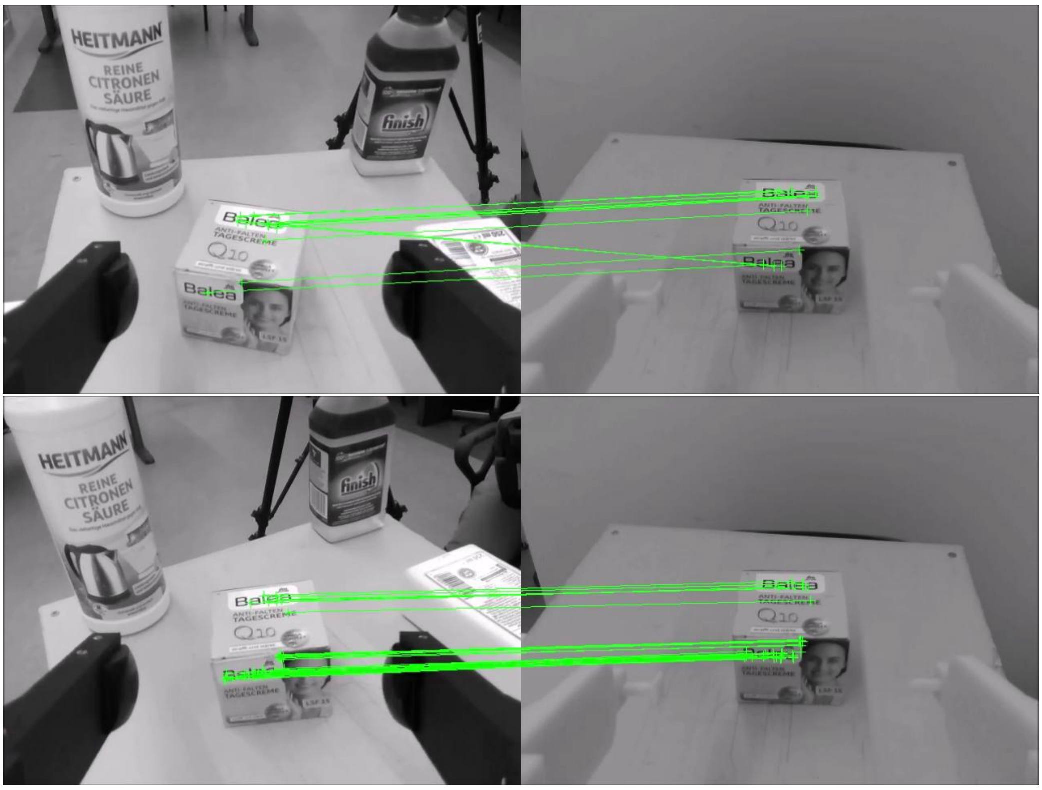

Figure 4.15: Example of matched keypoints (green crosses and lines). Current image from the eye-in-hand camera (left). Target image (right). The top and bottom figures show the keypoints matched during the first and second execution, respectively.

Note that, the plan can fail in every planning request. The planning pipeline (4.5) is executed with all the possible grasp poses $\boldsymbol{T}_{g_i}^{j}$ associated to the object j. The actual plan to use during the execution phase (and the corresponding grasp pose) can be selected among the ones that yield a success of all planning requests. In this thesis, the first feasible plan is picked, but it is easy to choose a different metric, e.g., the shortest path. Note that, each attempt made with a grasp pose is independent, thus it is possible to parallelize the computation.

4.3.1 Visual Servoing Controller

As highlighted by (4.5), the object pose $\widehat{\boldsymbol{T}}_{j}^{b}$ is uncertain and thus the grasp can likely fail, even if one used any state-of-the-art 6D localization algorithms based on RGB-D cameras. In fact, their typical accuracy of 1 cm is too bad compared to the grasping tolerance of most of the objects and the accuracy of the grasping location required to perform the pivoting maneuvers. We solve this issue by using a reactive visual controller that exploits the RGB-D data coming from the eye-in-hand camera to achieve the correct pre-grasp pose $\boldsymbol{T}_{v_l}^{b}$.

The visual servoing is activated after the execution of $\mathcal{R}_1$ when the robot has reached the rough pre-grasp pose $\widehat{\boldsymbol{T}}_{v_l}^{b} = \widehat{\boldsymbol{T}}_{j}^{b}\boldsymbol{T}_{v_l}^{j}$. The visual servoing locally adjusts this pose to reach the correct one.

The visual servoing module is based on the ViSP library (Marchand, Spindler, and Chaumette 2005). It uses data acquired from the RGB-D camera to control the movement of the robot in real time. A RealSense D435i depth camera has been arranged in a eye-in-hand configuration (Fig. 4.13). The Image-based Visual Servoing (IBVS) controls the robot motion by minimizing the error between a set of previously learned features $\boldsymbol{s}^*$ and those identified in the current frame image, $\boldsymbol{s}$:

$$\boldsymbol{e}(t) = \boldsymbol{s}(I(t)) - \boldsymbol{s}^*(I_{v_l}) \tag{4.6}$$

where $I(t)$ is the current image frame and I_{v_l} is the target image of the visual servoing controller, purposefully acquired and stored in the object database.

In a common IBVS, the image features are vectors of 2D matching points, which the algorithm aligns in the camera image plane. The proposed approach, instead, uses the 3D feature points of the ViSP library: s points are obtained by projecting the current RGB-D image plane into the 3D space; s^* points are obtained from a nominal RGB-D image acquired offline by bringing by hand the robot in the desired pregrasp pose. The visual servo module acquires in real time the current RGB-D image and tries to align $\boldsymbol{s}$ to $\boldsymbol{s}^*$ by moving the camera with the velocity

$$\boldsymbol{v}_c(t) = -\lambda \boldsymbol{L}\boldsymbol{e}(t), \tag{4.7}$$

where $\boldsymbol{L}$ is a model or an approximation of the so-called interaction matrix and λ is the control gain that yields the exponential convergence of the error (Marchand, Spindler, and Chaumette 2005).

The ViSP library provides five object tracking algorithms suitable for different kinds of scenarios. The one adopted in this thesis is the keypoint tracker, which recognizes useful points and tracks them in subsequent images.

To improve the reliability of the algorithm, the visual servoing controller is executed three times in a row. This is because, if the initial view pose is too far from the desired one, the ViSP library may find too few keypoints and the final error may be too high. Anyway, the first execution brings the robot to a closer view from which the ViSP library is able to match more keypoints. This is showed by Fig. 4.15, which shows the current image on the left and the desired one on the right; the green crosses and lines represent the matched keypoints. The top figure shows the situation at the end of the first run, the ViSP keypoint matcher found only few keypoints and the final error between the two images is still high. Instead, at the end of the second run (bottom figure) more keypoints are found and the final image is closer to the desired one.

After this phase, the relative pose between the camera and the object is known, thus, the absolute object pose is known as well. It is important to recall that, during the visual servoing phase, the robot configuration goes away from the planned trajectory. Thus the plan can not be executed as it is. A trivial solution may be to plan again using the true object pose. Nevertheless, the plan already computed is still valid and a complete replan can be avoided. The next section proposes a strategy to reconnect the planned trajectory to the actual one under mild assumptions.

4.3.2 Execution Phase

This section presents how the plan (4.5) is actually executed on the real robot.

The motion segment planned with the first result $\mathcal{R}_1$ is executed directly to bring the robot in the estimated pre-grasp pose $\hat{\boldsymbol{T}}^b_{v_l} = \hat{\boldsymbol{T}}^b_j \boldsymbol{T}^j_{v_l}$ from the initial configuration.

Then, the visual servoing loop (Section 4.3.1) adjusts the end-effector pose such that the final pose is very close to the real pre-grasp frame $\boldsymbol{T}^b_{v_l}$.

The joint configuration after the visual servoing algorithm is not on the planned path anymore, thus, the motion from the pre-grasp to the grasp pose cannot be executed by following the plan $\mathcal{R}_2$. It is executed as a simple interpolation (linear in translation and quaternion rotation) from the current pre-grasp pose to the grasp pose

$$\boldsymbol{T}^b_{g_i} = \boldsymbol{T}^b_{v_l} \boldsymbol{T}^{v_l}_{g_i} = \boldsymbol{T}^b_{v_l} (\boldsymbol{T}^j_{v_l})^{-1} \boldsymbol{T}^j_{g_i}. \tag{4.8}$$

We assume that during this short motion segment no collision can occur because we assume that the visual servoing introduces only slight modifications of the robot configuration.

Analogously, the displacement from the grasp pose to the lift pose $\boldsymbol{T}^b_l$ is executed by interpolating the grasp pose to the desired lift pose. It is important to underline that at the end of this motion, the configuration of the robot is not the same as that at the end of the planning result $\mathcal{R}_3$ due to the visual servoing action that adjusts the uncertain pre-pick pose.

Therefore, the plan $\mathcal{R}_4$ cannot be executed exactly as planned, therefore a simple exponential connection to the planned trajectory is implemented to asymptotically take the actual robot desired motion $\boldsymbol{q}_4(t)$ to the planned one $\hat{\boldsymbol{q}}_4(t)$

$$\boldsymbol{q}_4(t) = (\boldsymbol{q}_l - \hat{\boldsymbol{q}}_4(t))e^{-\alpha(t-t_0)} + \hat{\boldsymbol{q}}_4(t), \tag{4.9}$$

where α is a parameter that establishes the convergence rate and $\boldsymbol{q}_l$ is the joint configuration at the end of the lift phase.

The last motion segment in the result $\mathcal{R}_5$ can be directly executed as it is because the actual robot trajectory has reached the planned one. As a recall, we are assuming that during the exponential connection (4.9) no collision can occur since we assume that adjustments introduced by the visual servoing with respect to the plan are not so significant compared to the distance between the robot and the environment after the lift.

4.4 Pick-and-Place Experiments

This section presents the final set of experiment of this thesis. The whole combination of slipping controller, manipulation planner and task planner is tested in a lab-simulated in-store logistic scenario with pick and place tasks. Figure 4.16 shows the setup, an LBR iiwa 7 is equipped with the same end effector used in the rest of the thesis, i.e., a WSG50 gripper equipped with the SUNTouch force/tactile sensors (Appendix B). Moreover, a RGB-D camera Intel D435i is mounted on the last link of the robot. The object are initially located on the pick tray in front of the robot and have to be placed in the proper facing on one of the side shelves. The two objects considered for this demonstration are reported in Fig. 4.17 and are labeled as P_A and P_B. The

Object	μ	β_A
P_A	0.68	$2.5 \cdot 10^5$ Ns/m^3
P_B	0.82	$4.4 \cdot 10^5$ Ns/m^3

Table 4.6: Friction parameters for objects P_A and P_B.

objects physical parameters used by the slipping controller are reported in Tab. 4.6 while the finger dependent parameters are obviously the same used in the experimental sections of Chapter 3.

Four experiments have been carried out. In the first experiment the object P_A has to be placed in the narrow space between the two shelves on the right side of Fig. 4.16. A pivoting maneuver will be necessary to place the object without collisions. The remaining three experiments involve

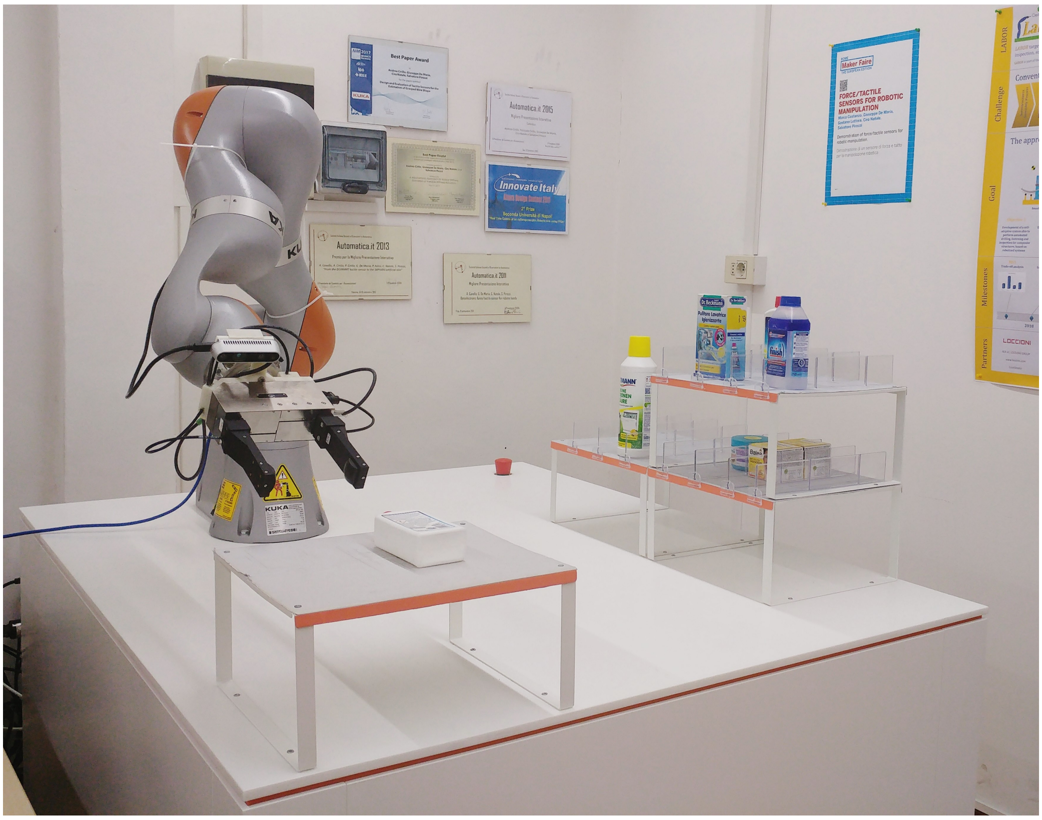

Figure 4.16: Experimental setup: robot Kuka LBR iiwa, gripper WSG50, tactile fingers SUNTouch , camera Intel D435i, pick tray and shelves to be refilled with three facings each.

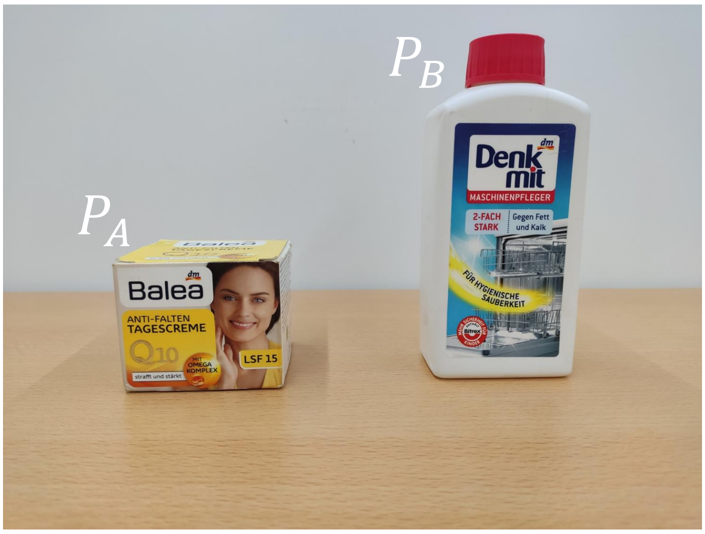

Figure 4.17: Objects handled during the experiments.

the object P_B in different initial orientations. Some of them will require the object pivoting abilities to correctly place the object because of limitations in the robot workspace. All the experiments are reported in the accompanying video (Appendix D.2).

4.4.1 Experiment 1

The Experiment 1 consists in picking the object P_A from the picking tray and place it on the central facing of the bottom right shelf of Fig. 4.16. The given object rough pose $\widehat{\boldsymbol{T}}_j^b$ is exactly at the center of the pick-tray with the frontal face towards the robot. The actual object pose is different because the object has been placed by hand. Nevertheless, the visual servoing algorithm has to deal with this uncertainty.

Fig. 4.18 shows a sequence of snapshots taken from the accompanying video (Appendix D.2) and Fig. 4.19 reports the planned and executed joint trajectories.

Firstly, the motion planner plans the whole motion and returns the sequence of results $\mathcal{R}_i$ with $i = 1, ..., 5$. Each result is a sequence of joint trajectory segments $\boldsymbol{q}_{i_j}(t)$ and the corresponding control modalities m_{i_j}, with $j = 1$ or $j \in \{1, 2\}$. If $\mathcal{R}_i$ is a standard motion in slipping avoidance mode, the corresponding j will assume only value 1, only one trajectory segment is contained in $\mathcal{R}_i$ and the control modality is $m_{i_1} = 0$. Otherwise, if $\mathcal{R}_i$ requires the pivoting ability, it will contain a sequence of two trajectory segments $\boldsymbol{q}_{i_1}(t)$ and $\boldsymbol{q}_{i_2}(t)$, the first in pivoting mode ($m_{i_1} = 1$) and the second in slipping avoidance mode ($m_{i_2} = 0$) (see Section 4.2).

$\mathcal{R}_1$ takes the robot in the rough pre-pick pose as shown by the first snapshot of Fig. 4.18 ($t = 3\,\mathrm{s}$).

At this time instant, the visual servoing is activated to reach the actual pre-pick pose. The feature error trend is reported in Fig. 4.20 together with the corresponding camera velocity. As stated in Section 4.3.1, the controller is activated three times in a row to match again the keypoints and improve the accuracy. At about 24 s the first reactivation is clearly visible in Fig. 4.20, the keypoints are matched again and the error is recomputed by using the new keypoints (see Fig. 4.15 to appreciate the keypoints tracked before and after this time instant). The second reactivation is not visible on the plot because, after the second run, the visual controller reached an error below the chosen threshold, namely, 0.001 m. Fig. 4.19 shows how, in the visual servoing phase, the executed joint trajectory goes away from the plan, thus, it is not possible to execute the plan result $\mathcal{R}_2$ because the initial joint configuration is not the planned one. The second snapshot of Fig. 4.18 ($t = 29\,\mathrm{s}$) shows the situation at the end of the visual servoing phase.

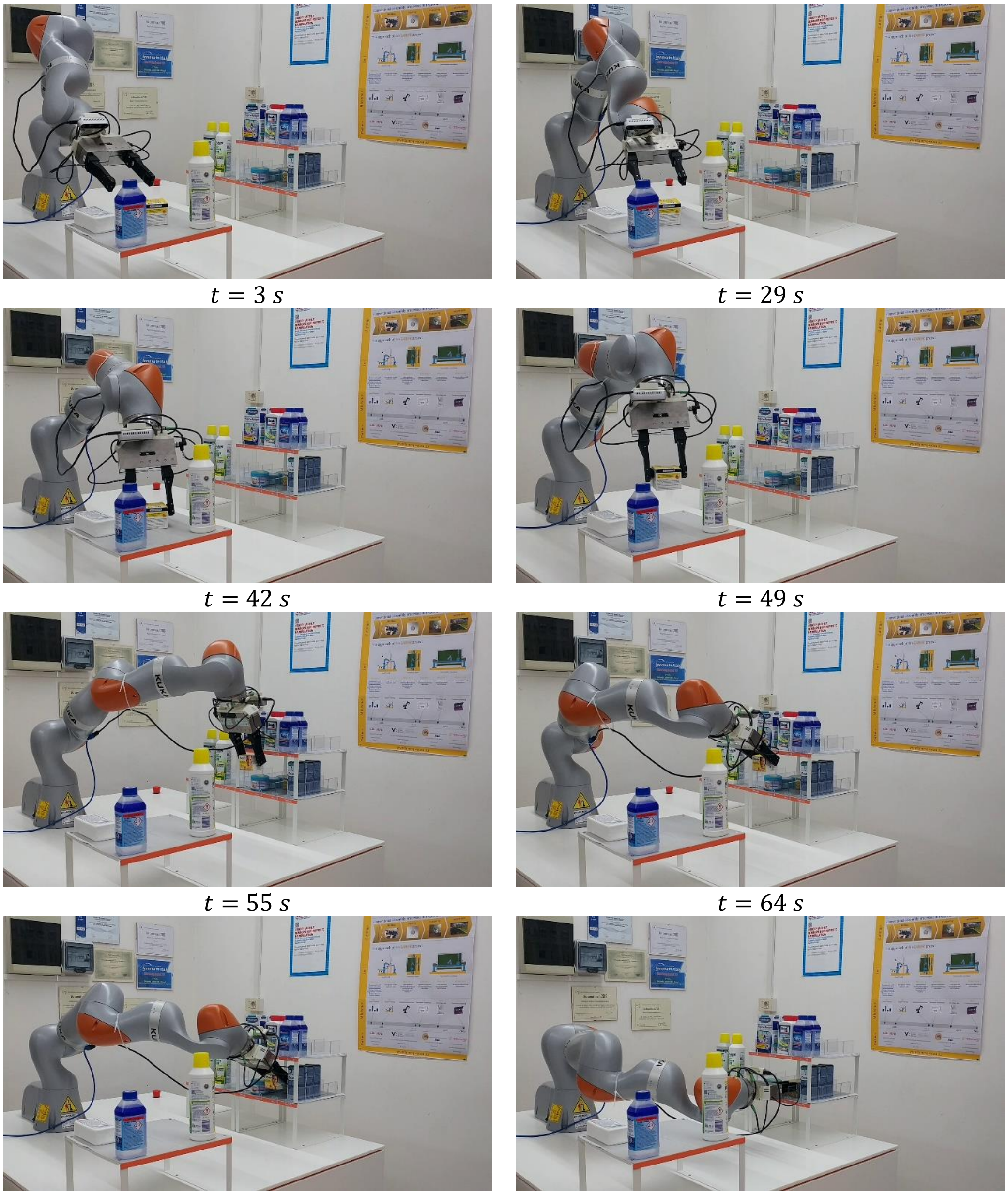

$t = 3\ s$ | $t = 29\ s$

$t = 42\ s$ | $t = 49\ s$

$t = 55\ s$ | $t = 64\ s$

$t = 67\ s$ | Object pushing

Figure 4.18: Experiment 1: Snapshots of the task execution, $t = 3\,\mathrm{s}$ corresponds to the robot in the rough pre-grasp pose $\widehat{\boldsymbol{T}}^b_{v_l}$. The last snapshot refers to the end of the object pushing phase. See the accompanying video (Appendix D.2).

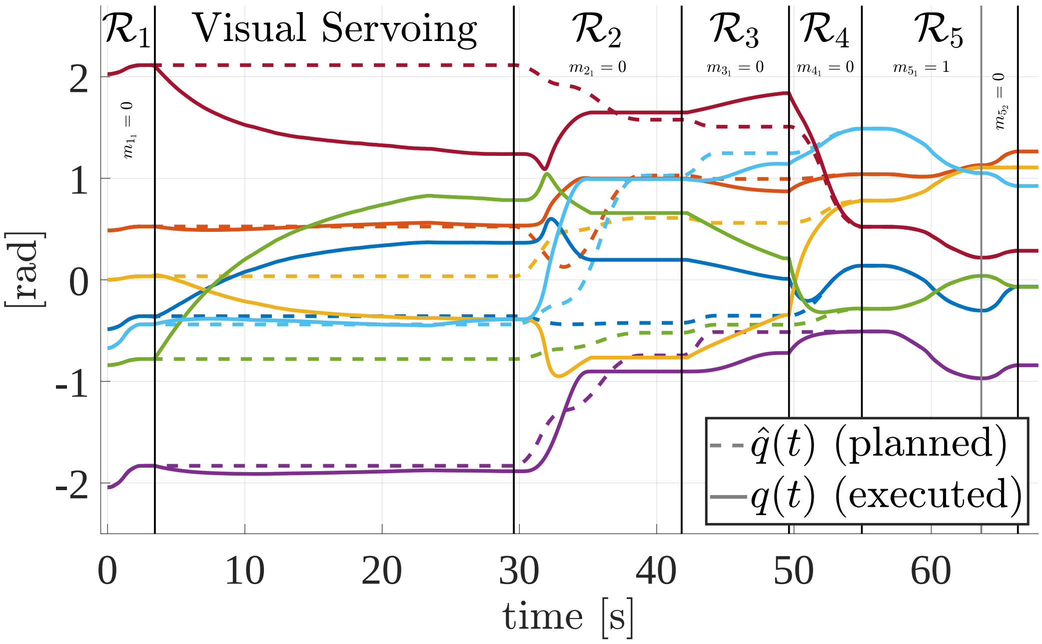

Figure 4.19: Experiment 1: Planned (dashed) and commanded (solid) joint trajectory. See the accompanying video (Appendix D.2).

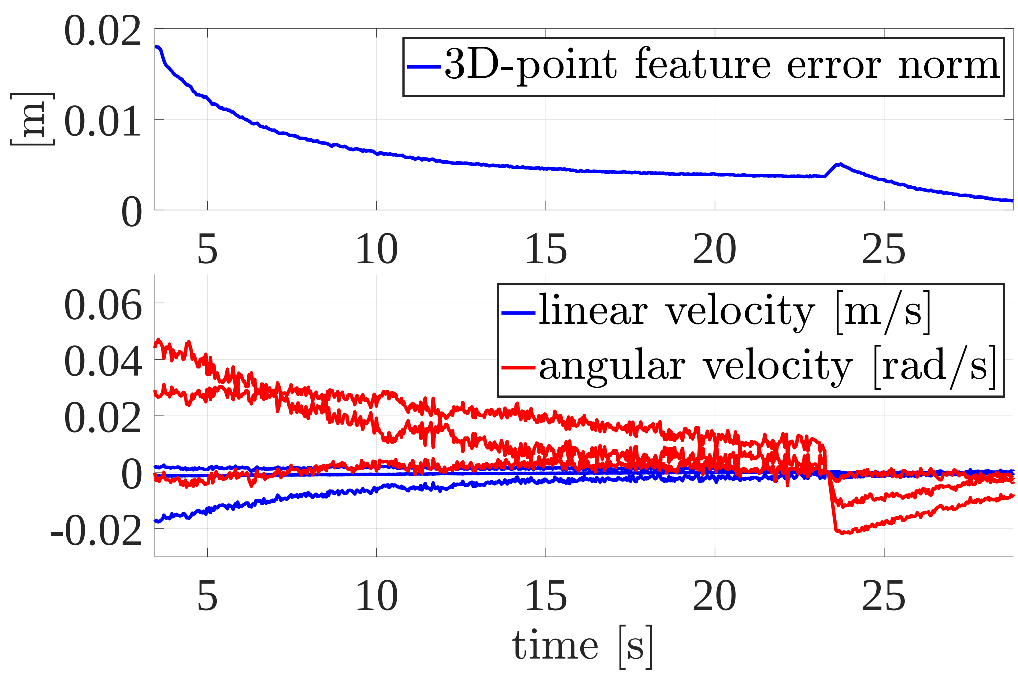

Figure 4.20: Experiment 1: ViSP 3D-point feature error norm (top) and the corresponding camera twist control output (bottom). See the accompanying video (Appendix D.2).

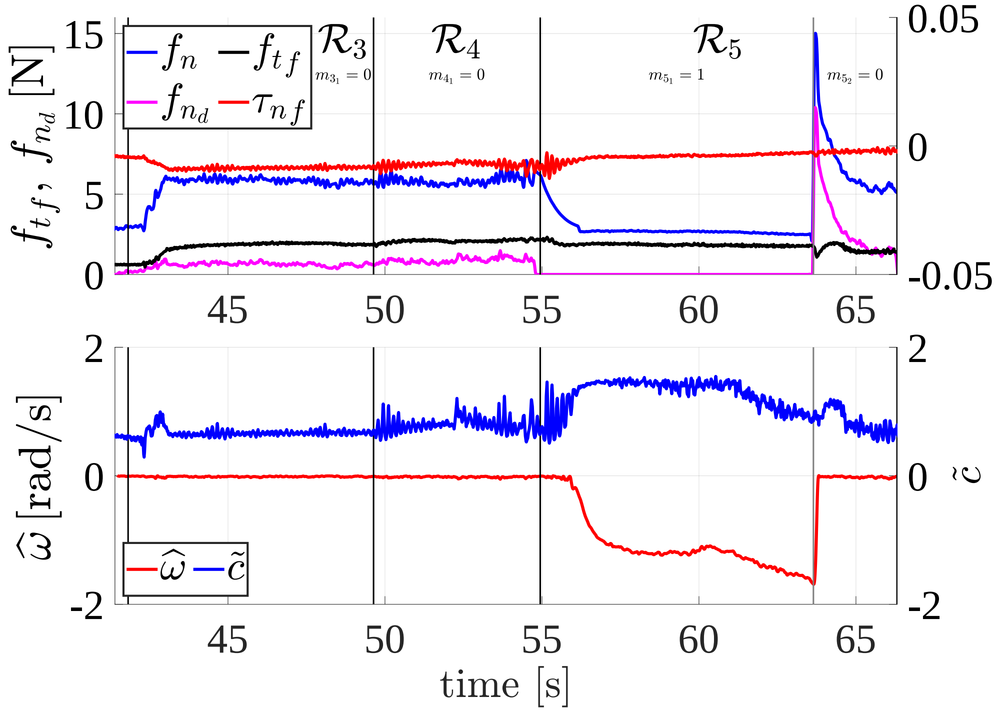

Figure 4.21: Experiment 1. Top plot (right axis): friction torque τ_{nf}. Top plot (left axis): tangential friction force f_{tf}; dynamic contribution of the slipping avoidance algorithm f_{n_d}; commanded normal force f_n. Bottom plot (right axis): estimated normalized center of rotation $\tilde{c}$; Bottom plot (left axis): slipping velocity about the CoR estimated by the observer $\widehat{\omega}$. See See the accompanying video (Appendix D.2).

At this point, a blind motion towards the grasp frame takes place ($t = 42\,\mathrm{s}$). Note that this corresponds to the plan result $\mathcal{R}_2$, but it is not executed, since it is assumed that in this short blind linear motion no collision can occur.

The same applies for the short upward linear motion executed to move away from the tray (until $t = 49\,\mathrm{s}$) corresponding to the planning result $\mathcal{R}_3$. At the beginning of this segment, the gripper is asked to grasp the object and the grasp controller automatically computes the grasp force by using the slipping avoidance mode of Section 3.5. This can be appreciated in Fig. 4.21-top, where, at about 42 s, the grasp force increases and the object is lifted without any significant slippage. This is confirmed by the measured tangential friction force f_{tf} due to the object weight.

At $t = 49\,\mathrm{s}$ the robot should follow the motion planned in $\mathcal{R}_4$ but the original plan cannot be executed since the actual initial configuration of the robot is different from the planned one. As explained in Section 4.3.2, to avoid re-planning, the simple exponential connection in (4.9) is actually commanded to the robot. It is clearly shown in Fig.4.19, where the solid lines exponentially converge to the dashed ones while keeping continuity of position, velocity, and acceleration. For this motion segment, the manipulation planner plans a slipping avoidance modality ($m_{4_1} = 0$).

The last planning result $\mathcal{R}_5$ is composed by two motion segments, the first one is a gripper pivoting maneuver ($m_{5_1} = 1$) that allows the gripper to change its orientation with respect to the object by allowing a controlled rotational sliding. This is evident from the slipping velocity about the CoR $\widehat{\omega}$ estimated by the observer and reported in Fig. 4.21-bottom. The configurations before and after the pivoting are reported in Fig. 4.18 at $t = 55\,\mathrm{s}$ and $t = 64\,\mathrm{s}$ respectively. In the second motion segment of $\mathcal{R}_5$, the slipping controller is again asked to avoid slippage ($m_{5_2} = 0$) to safely place the object inside the shelf facing ($t = 67\,\mathrm{s}$).

In these experiments, there is also a last blind pre-programmed maneuver that pushes a bit the object inside the facing to leave enough room for a further one to be placed. This corresponds to the last snapshot of Fig 4.18 and is visible in the video (Appendix D.2).

4.4.2 Experiment 2

The Experiment 2 is aimed to show a simple case where no special manipulation ability is required.

The object P_B, staying vertical on the pick tray (Fig. 4.22, $t = 5\,\mathrm{s}$), has to be placed on the top shelf on the right.

The planner finds a solution with fixed grasp modality in all the plan results $\mathcal{R}_i$. Thus, all the motion is executed in slipping avoidance mode and no virtual joint is needed to achieve the place pose.

Figure 4.23 shows the executed and planned joint trajectories. Again, as in Experiment 1, the visual servoing algorithm (Fig. 4.24) introduces a modification, due to uncertainty of the pose of the object P_B, in the joint trajectory that is recovered by the exponential connection in the phase $\mathcal{R}_4$. This time, $\mathcal{R}_5$ is composed of a unique motion segment in slipping avoidance mode ($m_{5_1} = 0$).

With reference to Fig 4.25, during the lift phase (about 35 s) the observer estimates a peak in the slipping velocity $\widehat{\omega}$, this causes a peak in the dynamic contribution f_{n_d} and, in turn, in the normal load f_n. This permits to safely lift the object. Note that such effect was not appreciable in the previous experiment because the object P_A is lighter.

It is worth noticing that during the phase $\mathcal{R}_4$ the torque magnitude increases, this is due to the robot motion. This causes a reduction of the estimated normalized CoR position $\tilde{c}$. This is an expected behavior because a higher friction torque means that the object is more prone to rotate than translate if the normal load is reduced. At the beginning of the phase $\mathcal{R}_5$ ($t = 48\,\mathrm{s}$), the object assumes again a vertical orientation, the torque goes towards zero and $\tilde{c}$ rises again.

It is evident that in the last phase $\tilde{c}$ has large oscillations. This is because we are in a singular situation, the torque is almost zero and it crosses the zero line various times because of elastic oscillations caused by the arm motion and the elastic nature of the fingertip. In this situation $\tilde{c}$ can be either $\pm\infty$ depending on the sign of τ_{nf} (see Chapter 2). This is solved by using a small torque lower threshold in the algorithm instead of zero that causes a saturation-like behavior in the signal $\tilde{c}$. When the oscillations on the torque are greater than the threshold, $\tilde{c}$ changes sign and the result is the one in the right part of the plot. These torque oscillations are related to the inertial torque that the dynamic controller counteracts with normal force peaks to avoid slippage.

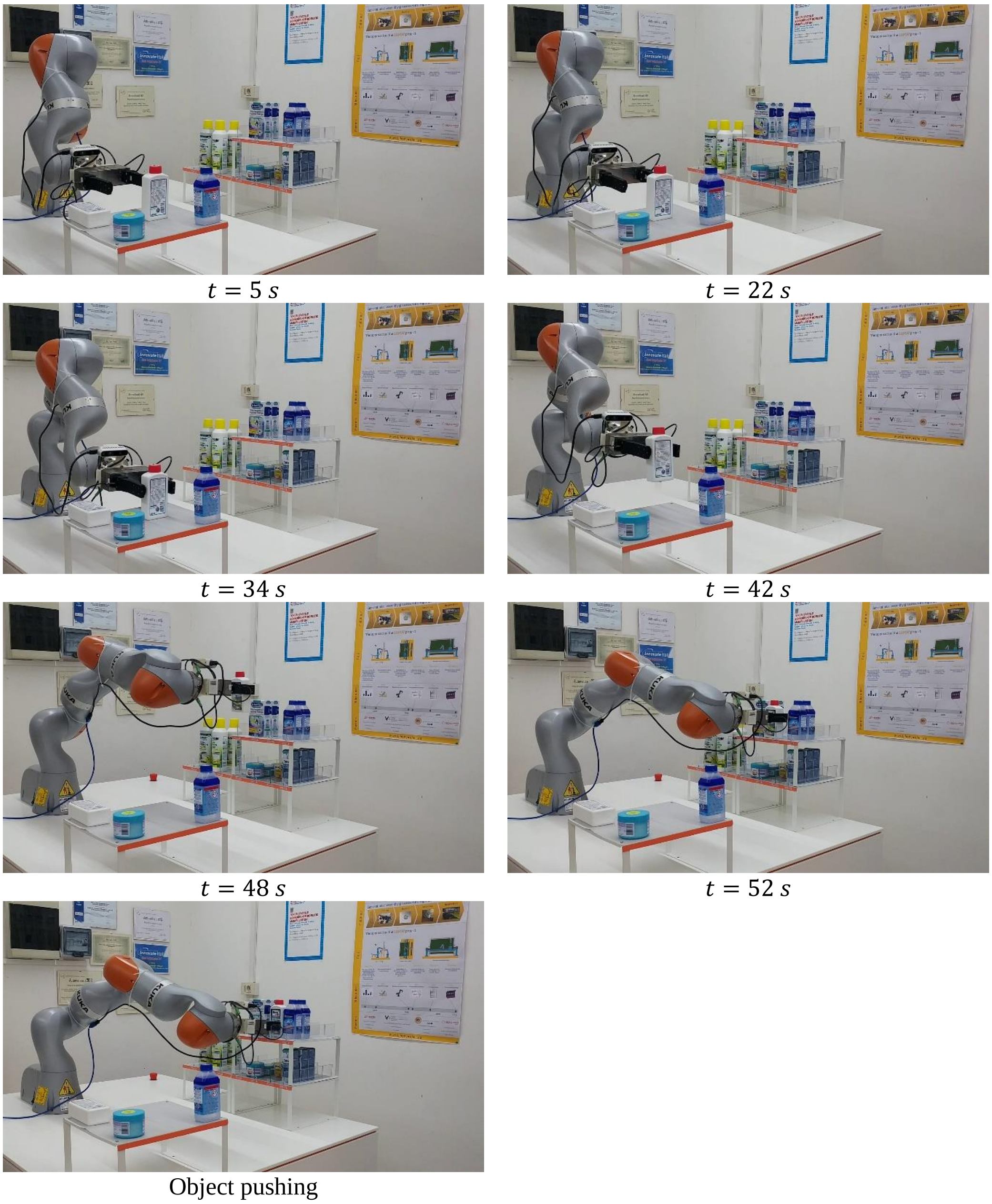

Figure 4.22: Experiment 2: Snapshots of the task execution, $t = 5\,\mathrm{s}$ corresponds to the robot in the rough pre-grasp pose $\widehat{\boldsymbol{T}}^{b}_{v_l}$. The last snapshot refers to the end of the object pushing phase. See the accompanying video (Appendix D.2).

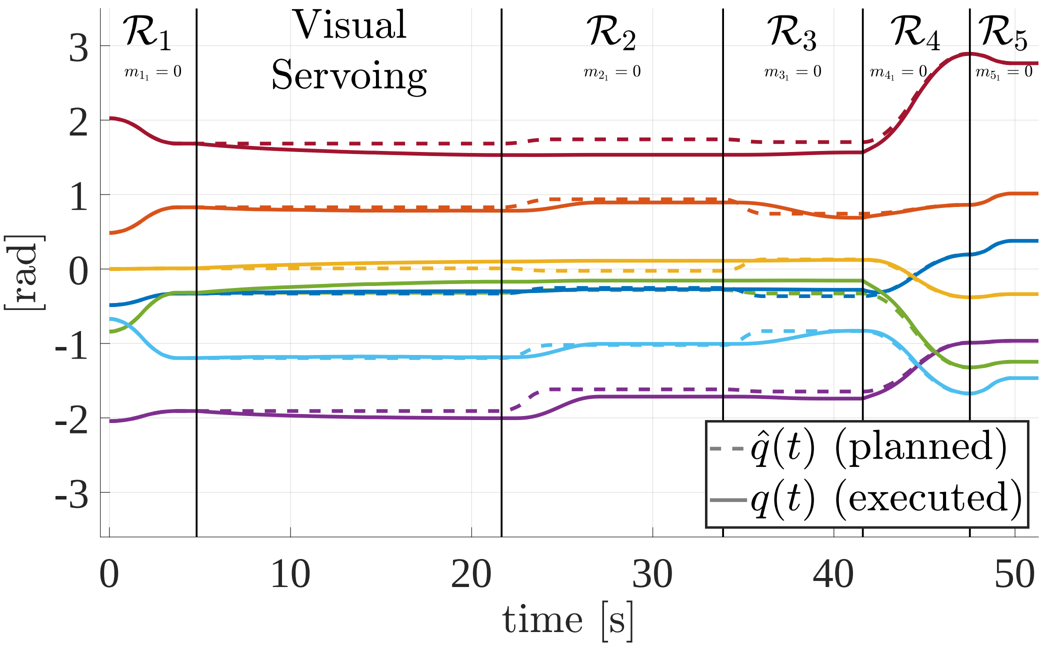

Figure 4.23: Experiment 2: Planned (dashed) and commanded (solid) joint trajectory. See the accompanying video (Appendix D.2).

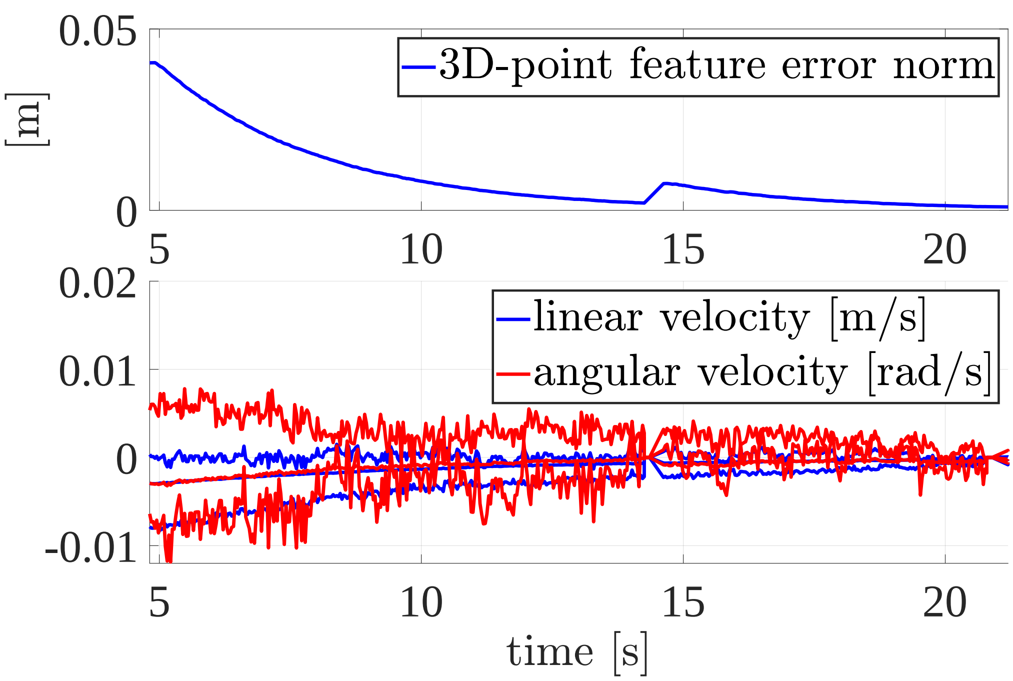

Figure 4.24: Experiment 2: ViSP 3D-point feature error norm (top) and the corresponding camera twist control output (bottom). See the accompanying video (Appendix D.2).

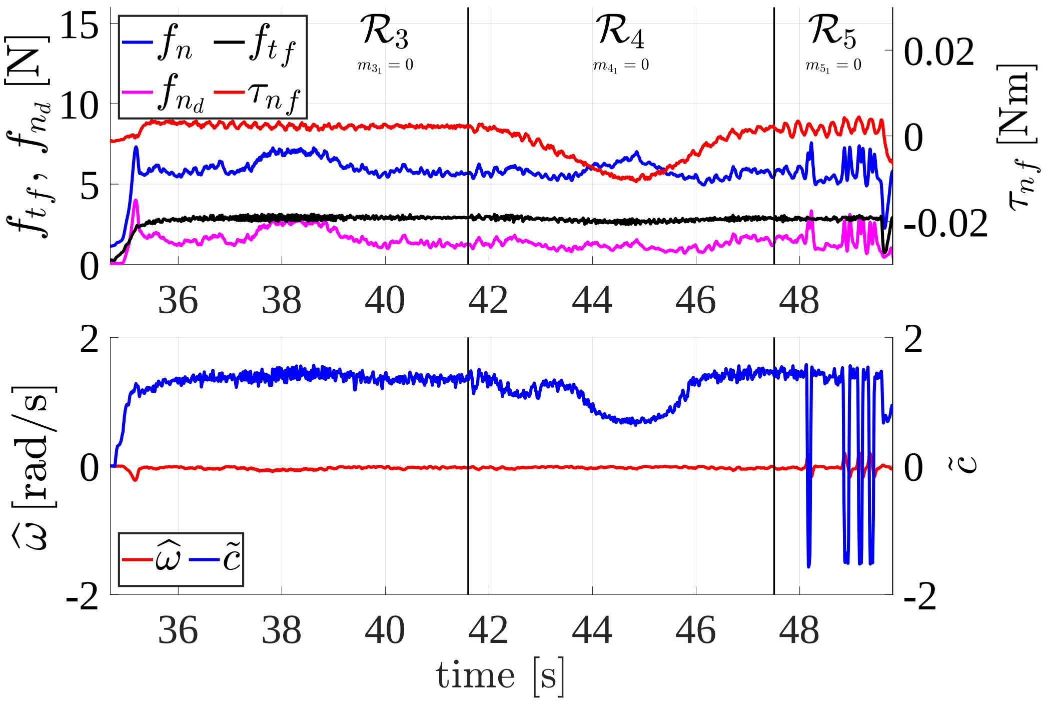

Figure 4.25: Experiment 2. Top plot (right axis): friction torque τ_{nf}. Top plot (left axis): tangential friction force f_{tf}; dynamic contribution of the slipping avoidance algorithm f_{n_d}; commanded normal force f_n. Bottom plot (right axis): estimated normalized center of rotation $\tilde{c}$; Bottom plot (left axis): slipping velocity about the CoR estimated by the observer $\widehat{\omega}$. See the accompanying video (Appendix D.2).

4.4.3 Experiment 3

Experiment 3 shows how the robot is able to correctly pick the knocked over object P_B from the pick-tray and place it on the top right shelf with the two adjacent facings already occupied by other products. In this case, the object can not be placed vertically because the fingers would collide with the objects already present on the shelf. For this reason, a slightly tilted final orientation is commanded. Note that the final object pose is an input of the motion planner and, in this case, the programmer chooses it by hand. In a real case scenario, to fully automate the process, a higher level module (like a Store Management System) should choose the final object orientation by using the current shelf state and some semantic rules.

The initial object pose is shown in Fig. 4.26 ($t = 8\,\mathrm{s}$), it lies horizontally on the pick-tray with the frontal object face pointing downward. Of course, the rough object pose $\widehat{\boldsymbol{T}}_j^b$ cannot be the vertical one (as in Experiment 2) but has to be horizontal. This can be achieved by using a state-of-art object localization algorithm, such as RANSAC (Papazov and Burschka 2011) and ICP (Rusinkiewicz and Levoy 2001), that is able to automatically estimate the rough object pose $\widehat{\boldsymbol{T}}_j^b$ by using the camera information. The accuracy of the localization can be even quite rough owing to the adoption of the visual servoing reactive controller.

This time the successful grasp pose selected by the planning algorithm is the one reported in Fig. 4.26($t = 35\,\mathrm{s}$) and the solution contains an object pivoting maneuver.

As in the previous experiments, the visual servoing algorithm adjusts the robot pose and the exponential connection takes the trajectory again on the plan (see Fig. 4.27 and Fig. 4.28).

At about $t = 36\,\mathrm{s}$ the lift phase begins. The object pose is now horizontal and the torque is not negligible. Figure 4.29 clearly shows a significant peak in f_{n_d} during the lift phase. At the same time the friction torque magnitude increases and the object is lifted keeping the horizontal orientation as shown in Fig. 4.26($t = 43\,\mathrm{s}$). Note that the normal force needed to lift the object in this situation is significantly greater as forecasted by the Limit Surface theory because it has to counteract also the effects of the gravitational torque. The slipping avoidance controller is able to automatically adapt the normal force to avoid both rotational and translational slippage.

At $t = 49\,\mathrm{s}$ the object is held in front of the place shelf in the pre-place pose with the configuration reported in Fig. 4.26. The planning result $\mathcal{R}_5$ consists in two trajectory segments. The first one $\boldsymbol{q}_{5_1}(t)$ is a constant trajectory that keeps the robot in the current configuration while the pivoting ability is activated ($m_{5_1} = 1$). At the end of $\boldsymbol{q}_{5_1}(t)$ the object reaches a

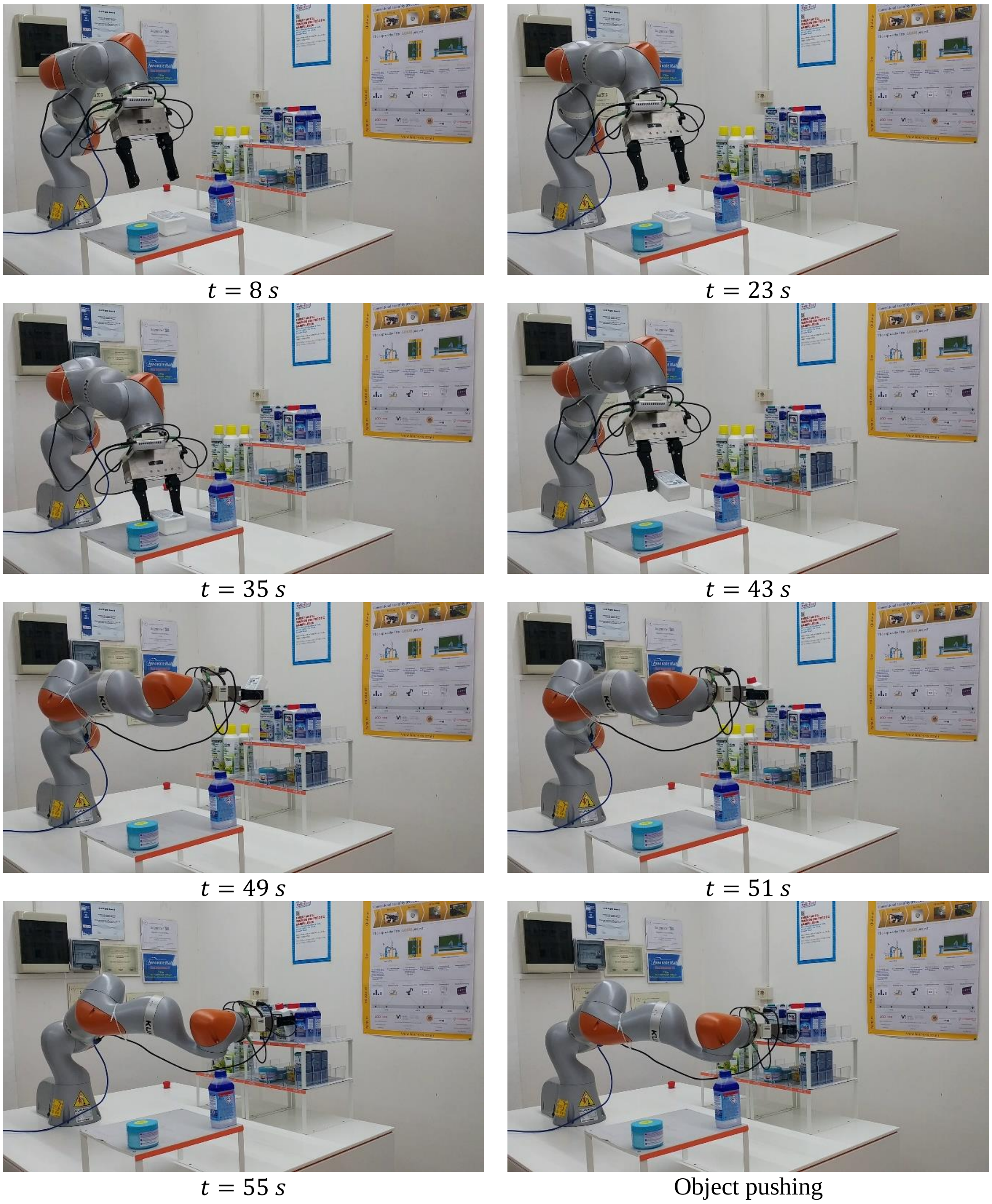

Figure 4.26: Experiment 3: Snapshots of the task execution, $t = 8\,\mathrm{s}$ corresponds to the robot in the rough pre-grasp pose $\widehat{\boldsymbol{T}}^{b}_{v_l}$. The last snapshot refers to the end of the object pushing phase. See the accompanying video (Appendix D.2).

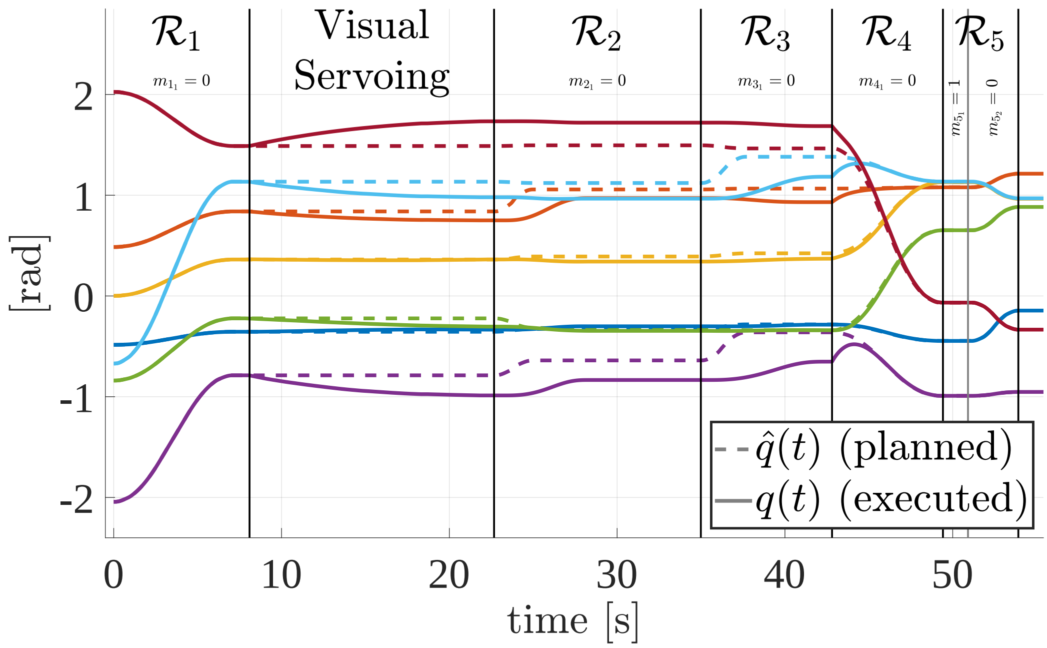

Figure 4.27: Experiment 3: Planned (dashed) and commanded (solid) joint trajectory. See the accompanying video (Appendix D.2).

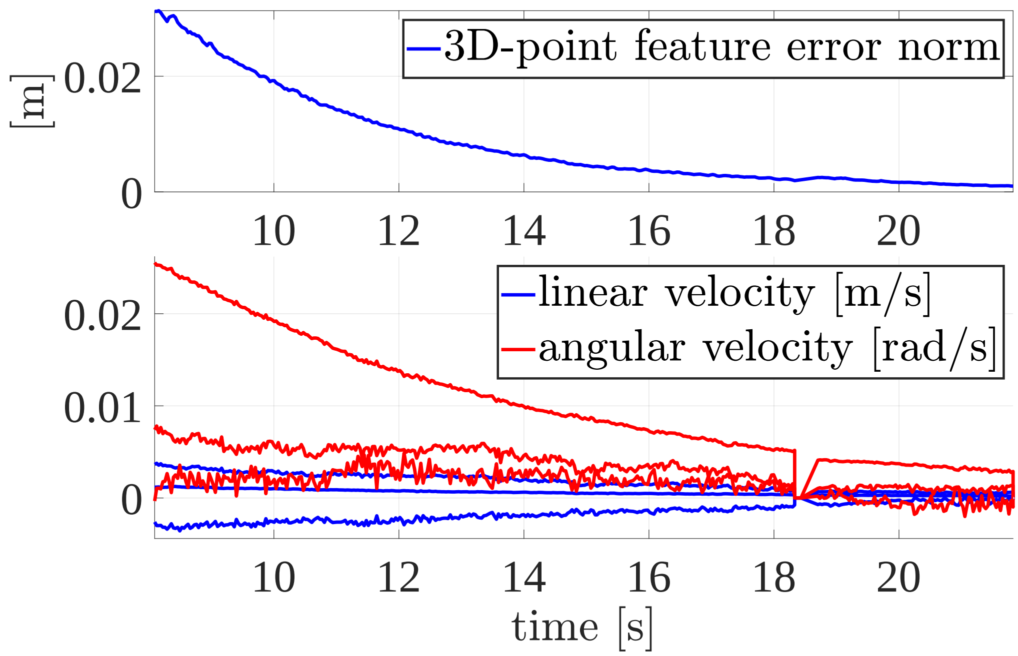

Figure 4.28: Experiment 3: ViSP 3D-point feature error norm (top) and the corresponding camera twist control output (bottom). See the accompanying video (Appendix D.2).

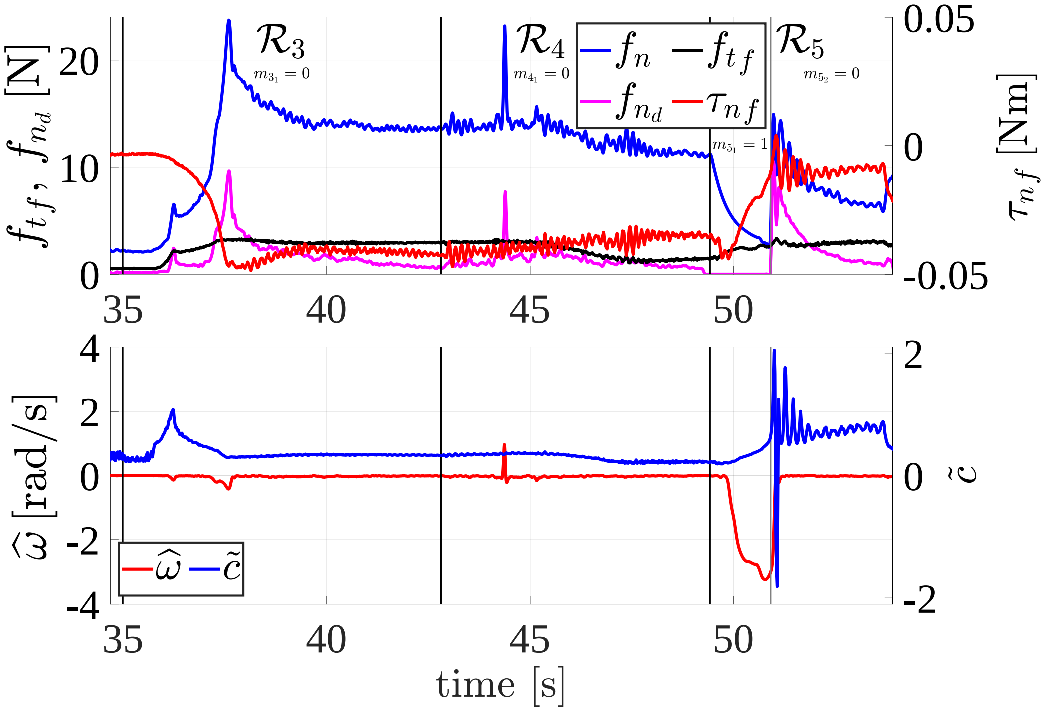

Figure 4.29: Experiment 3. Top plot (right axis): friction torque τ_{nf}. Top plot (left axis): tangential friction force f_{tf}; dynamic contribution of the slipping avoidance algorithm f_{n_d}; commanded normal force f_n. Bottom plot (right axis): estimated normalized center of rotation $\tilde{c}$; Bottom plot (left axis): slipping velocity about the CoR estimated by the observer $\widehat{\omega}$. See the accompanying video (Appendix D.2).

vertical orientation and the second trajectory segment $\boldsymbol{q}_{5_2}(t)$ is a fixed grasp motion ($m_{5_2} = 0$) that brings the object in the place pose. This solution corresponds to line 13 of Algorithm 1 in Section 4.2.

The pivoting can be appreciated in Fig. 4.29. During the pivoting (between 49 and 51 seconds) the estimated slipping velocity $\widehat{\omega}$ reports a large peak that corresponds to the large orientation change of the object that can be appreciated in the corresponding snapshots of Fig. 4.22 and in the video (Appendix D.2).

After the pivoting, the robot can safely place the object by using the slipping avoidance mode as shown in the accompanying video (Appendix D.2).

4.4.4 Experiment 4

Experiment 4 is devoted to highlight the versatility of the planning algorithm. The initial condition is similar to the one of Experiment 3, but now the object P_B lays horizontally with its label upside down as shown in the first snapshot of Fig. 4.30. The planner found a grasp pose with the camera upside down, in fact, the camera is no longer visible in the first four snapshots. Nevertheless, the task continues in a way similar to the previous experiments.

The visual servoing algorithm is activated as usual. The aim of the visual controller is to reach the desired relative gripper/object pose, thus, the upside-down camera pose does not interfere with the algorithm (see Fig. 4.32 and the accompanying video in Appendix D.2).

This time the planner is able to find a solution in fixed grasp mode and the pivoting modality is never activated.

It is worth noticing that after the robot has reached the place pose, the gripper starts opening to release the object (at about $t = 60\,\mathrm{s}$) and the object first slightly rotates and then it slightly translates toward the shelf layer. These two motions are visible in the video (Appendix D.2) and are perfectly captured by the nonlinear observer that estimates two peaks in the velocity $\widehat{\omega}$ (Fig. 4.33). Moreover, it is clear that the second peak refers to a translational motion in view of the corresponding large estimated value of the CoR position $\tilde{c}$.

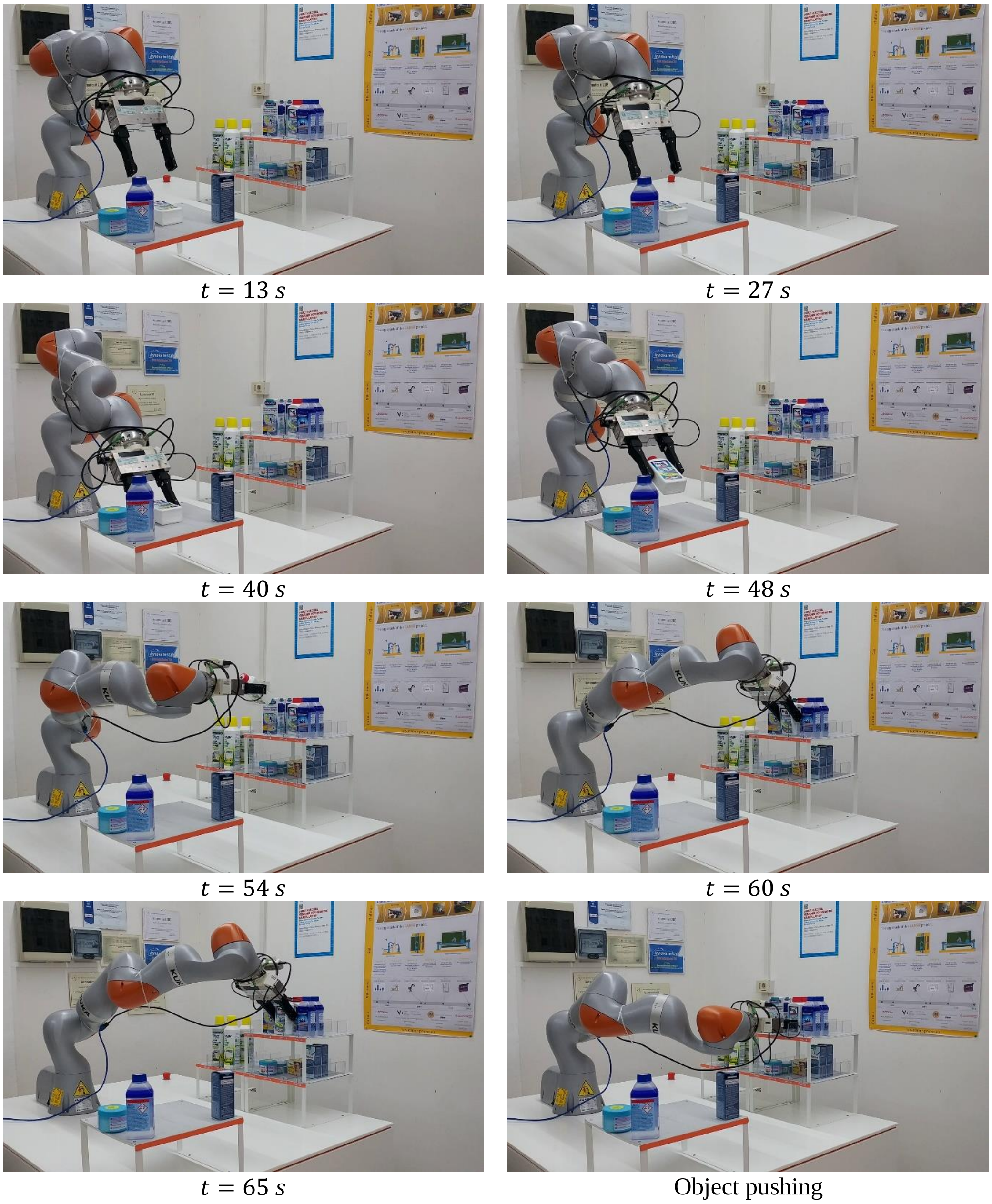

Figure 4.30: Experiment 4: Snapshots of the task execution, $t = 13\,\mathrm{s}$ corresponds to the robot in the rough pre-grasp pose $\widehat{\boldsymbol{T}}^{b}_{v_l}$. The last snapshot refers to the end of the object pushing phase. See the accompanying video (Appendix D.2).

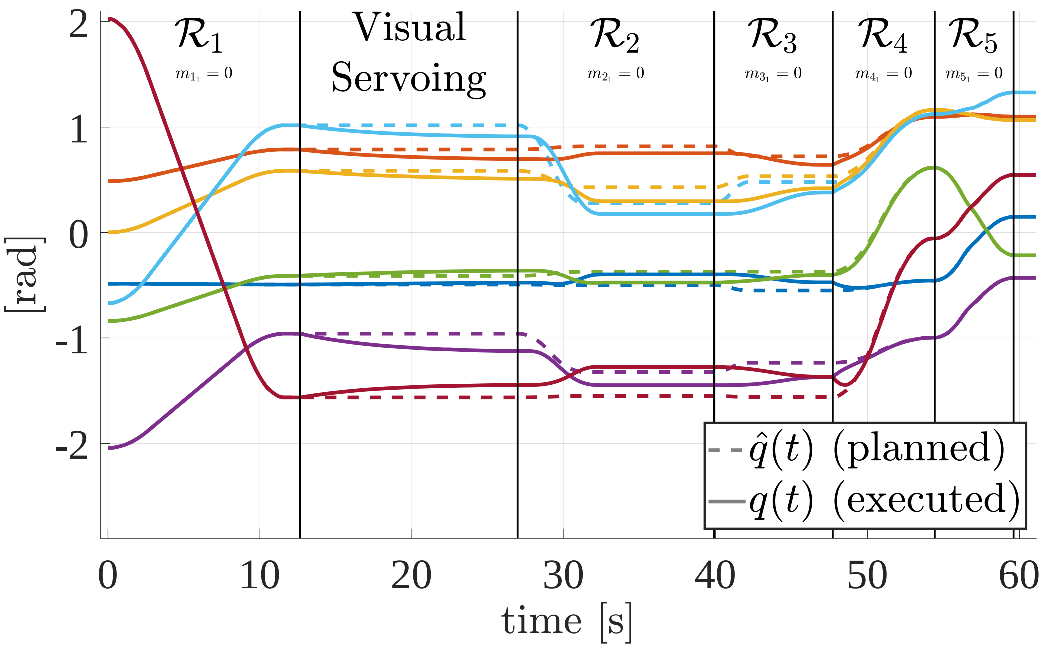

Figure 4.31: Experiment 4: Planned (dashed) and commanded (solid) joint trajectory. See the accompanying video (Appendix D.2).

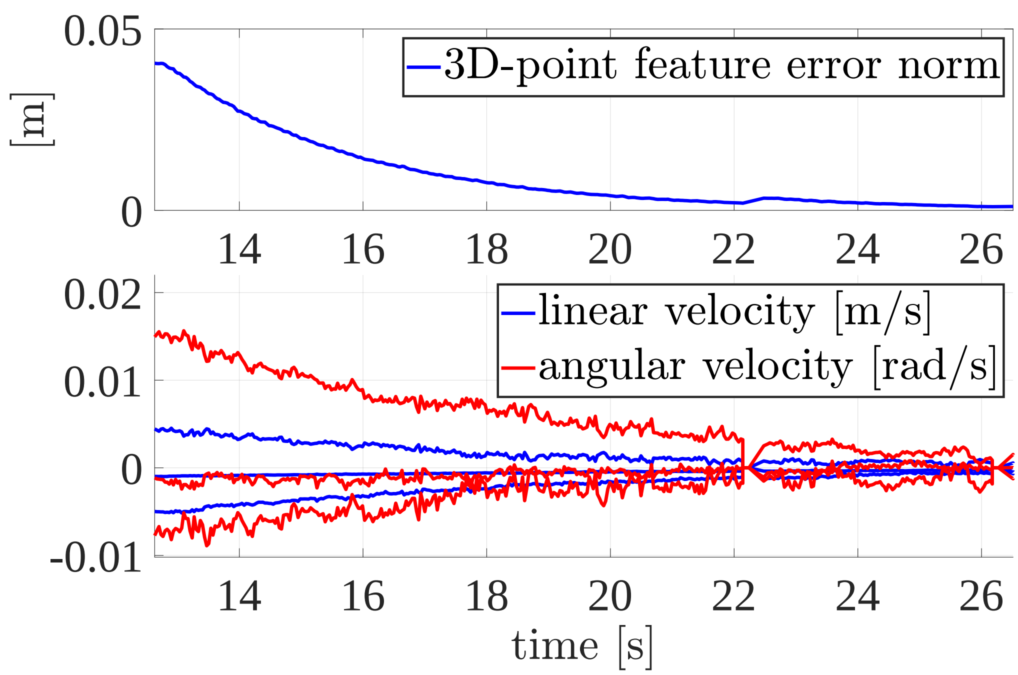

Figure 4.32: Experiment 4: ViSP 3D-point feature error norm (top) and the corresponding camera twist control output (bottom). See the accompanying video (Appendix D.2).

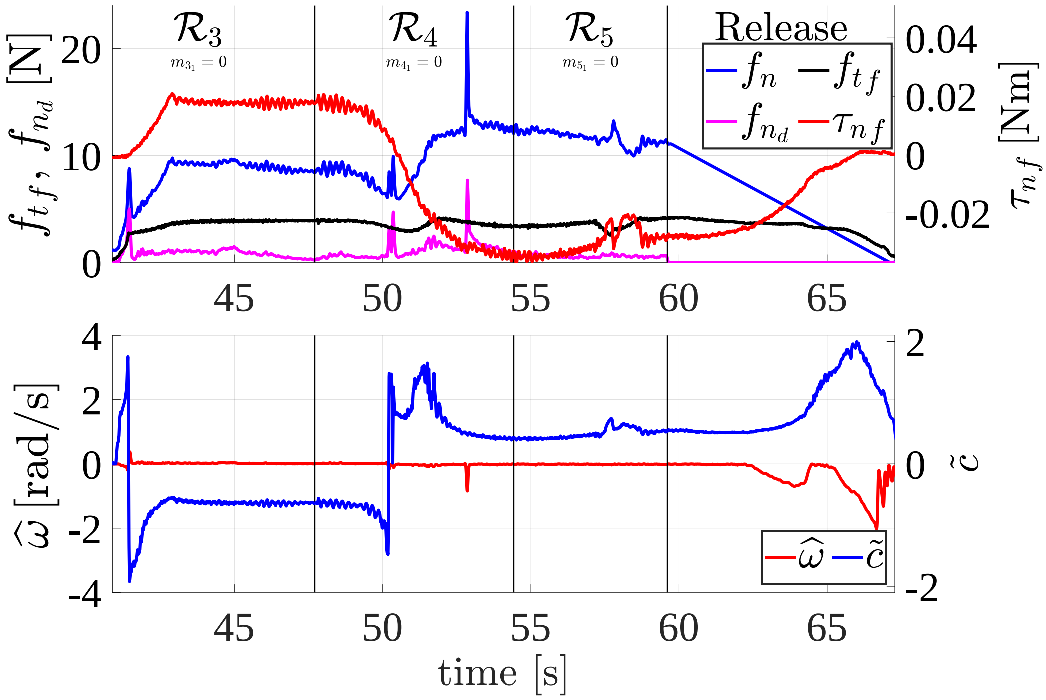

Figure 4.33: Experiment 4. Top plot (right axis): friction torque τ_{nf}. Top plot (left axis): tangential friction force f_{tf}; dynamic contribution of the slipping avoidance algorithm f_{n_d}; commanded normal force f_n. Bottom plot (right axis): estimated normalized center of rotation $\tilde{c}$; Bottom plot (left axis): slipping velocity about the CoR estimated by the observer $\widehat{\omega}$. See the accompanying video (Appendix D.2).

4.5 Conclusions

This chapter presented two strategies to integrate the manipulation abilities presented in Chapter 3 in a planning algorithm. The pivoting ability is kinetically represented as an additional revolute joint placed between the fingers. The chapter showed how, by adding such a joint, the robot has a larger workspace, in fact, it can perform tasks that before were infeasible, such as placing an object between two shelves by using an initial grasp angle that does not allow the gripper to enter between the shelves. The additional joint cannot be treated as the others because it represents the pivoting motion of the object between the fingers subject to gravity, thus, it cannot move in any direction.

The first strategy uses the gripper pivoting maneuver in all the robot motion and the object is constrained to keep a "vertical" orientation in the whole trajectory. This is useful when the object's initial and desired orientation are both vertical and the pivoting is used to avoid the obstacles between the gripper and the environment in a sort of null-space motion that moves the robot arm without move the object.

The second strategy has been designed to automatically choose the slipping control modality in specific segments of the planning trajectory. During the pivoting the arm or the object moves, but the object position is fixed in the space and it can only rotate. Nevertheless, this algorithm is able to generate both gripper and object pivoting maneuver.

Finally, this chapter presented a task and grasp planner built on top of the proposed pivoting planner. The algorithm needs the geometry of the object and its initial pose. By executing various planning attempts, the planner generates a feasible pick-and-place trajectory and automatically chooses the initial grasp pose. In the real case scenario, the object's initial pose is uncertain and only a rough estimation is available. For this reason, during the execution phase, the actual grasp has been achieved by using a visual servoing algorithm that aligns the gripper to the object to be grasped.

Four demonstrations have been carried out to show the effectiveness of the approach. The setup is a lab-simulated in-store logistic scenario and the task involves pick-and-place operations for autonomous shelf refilling. The experiments showed how the planner is able to automatically choose the initial grasp configuration, and autonomously decide to use gripper or object pivoting depending on the environmental scene.

The pivoting planner uses a standard motion planner and activates and deactivates the additional pivoting joint to find the desired trajectory. The particular low-level planner used may affect the result. A poorly configured planner may generate long and unnatural trajectories, have a long convergence time, or may not find a solution at all. Future evolutions of the planning approach will be devoted to directly build a low-level planner able to directly use the pivoting ability. A possible approach may be to use an RRT* algorithm (Karaman and Frazzoli 2011) by designing suitable cost function and constraints.

Chapter 5

Conclusion

This thesis demonstrates how in-hand manipulation is possible with simple end effectors that have limited intrinsic dexterity, i.e., parallel-jaw grippers. The main idea is to exploit external aids, such as gravity, and use the gripper normal force as a brake that can be released or applied to allow or stop the in-hand motion, respectively. The proposed approach relies only on the grasp force control and not on pushing maneuvers against the environment.

The approach relies on the Limit Surface concept that is described in Chapter 2 and then extended to the case of viscous friction. The LS framework is exploited to solve the *inverse LS problem*, i.e., find the instantaneous Center of Rotation position given the measured friction force and torque.

This thesis has proposed a planar slider dynamic model by merging the LS theory and the LuGre dynamic friction model. It describes the motion as a pure instantaneous rotation about the CoR and is able to catch the relation between the normal force and the resulting sliding motion. A complete stability and observability analysis has been carried out and, finally, the model is exploited to build a nonlinear observer able to catch the slipping velocity by using the measured translational and torsional friction. Experimental evaluations prove that the observer is able to reconstruct the slipping velocity by using an external IMU as ground truth.

In this framework, we propose two algorithms that provide two in-hand manipulation primitives, namely, slipping avoidance and pivoting. The slipping avoidance mode provides the normal force needed to firmly grasp an object avoiding both translation and rotation. The pivoting mode, instead, provides the normal force that allows the in-hand rotation of the object while avoiding translation. The combination of the two modalities and the robot motion allows to arbitrary reorient the object in-hand with respect to the gripper.

Finally, we have proposed two manipulation planning strategies able to use the aforementioned manipulation primitives. The first strategy constrains a vertical absolute object orientation in all the motion by using the pivoting ability. This approach is suitable only for a vertical final object orientation but permits to find solutions in tight spaces and uses the pivoting ability in the whole trajectory. The second strategy generates a sequence of trajectory segments, each one characterized by a control modality (slipping avoidance or pivoting). This approach is able to find a solution also for a non-vertical target object orientation, but the pivoting can be activated only if the grasp axis is fixed in the space.

On top of the last manipulation planner, this thesis proposed a higher-level task planner that computes a complete pick and place task by using the pivoting abilities. The planner is able to automatically choose the initial pick pose by selecting a feasible one from a given set.

The object initial pose is considered uncertain and, during the execution phase, a visual servoing algorithm is used to correctly grasp the object. This corrective action causes the robot motion to go away from the planned trajectory, nevertheless, an exponential interpolation brings again the robot to the planned path after the pick.

The complete approach is tested in a lab-simulated in-store logistic scenario where the robot is asked to place objects on supermarket shelves. The results demonstrate that in-hand manipulation is able to significantly enlarge the robot workspace and the task can be performed by a simple 1DOF gripper.

The model-based in-hand manipulation abilities are the main contribution of this thesis. In fact, in the current literature, similar model-based in-hand maneuvers are done by using a constant normal force and pushing the object against an external constraint (Chavan-Dafle, Holladay, and Rodriguez 2020), or by using an external visual sensor to track the pivoting angle (Viña B. et al. 2016). While, in this thesis, only force/tactile sensing is used and the only controllable input is the grasp force.

Of course, some assumptions may not fit all possible manipulation scenarios. Firstly, the motion is modeled as a planar slider. We need that the grasped object has two parallel faces and it is grasped such that it can move only in the plane orthogonal to the gripper actuation direction. The geometry of the objects considered in the experiments fits in the model formulation, but, an in-store scenario has also objects that cannot be treated as a planar slider, such as, cylindrical tubes or very deformable packages. Moreover, we need the model parameters; if the slider is rigid, then the only object dependent parameters are the dry and viscous friction coefficient (see Appendix B). As shown in the failure cases of Section 4.1.1, an underestimation or an overestimation of the friction coefficient may cause the inability to correctly execute the pivoting or the falling of the object, respectively.

Concerning the last experiments, visual servoing is used to deal with the uncertainty of the initial object pose. This approach is feasible only for texture-reach items, otherwise, the algorithm would be unable to find the keypoints. Luckily, the supermarket items have texture-reach labels, anyway, a more general approach could use a novel state-of-the-art technique that does not need texture-reach items such as DenseFusion (C. Wang et al. 2019). Unfortunately, such an approach has a bigger localization error compared to the closed-loop visual servoing, thus, more effort is needed in this research field.

This thesis opens many future extensions.

First of all, the mathematical investigation of the stability of the planar slider model carried out in Chapter 3 assumes that all the system inputs are constant. This is a bit restrictive because, during the pivoting maneuver, the external torque varies and the normal force is regulated according to a control law. Future works will be devoted to study the equilibrium of the trajectory of the slider model subject to time-varying external torque and normal force. To do that, could be worth introducing a modification of the system equations by explicitly considering the external torque as the gravity torque, however, this approach would need to introduce an additional state variable to track the angular position of the object.

It would be worth investigating the case of bimanual manipulation where the object is held by two grippers. This would yield to a different planar slider model and the theorems and propositions demonstrations may be different. Nevertheless, this would open to different manipulation primitives that involve the pivoting with respect to a gripper and slipping avoidance with respect to the other one.

Moreover, it would be interesting to add the translational slippage among the other in-hand manipulation primitives. The challenge in this case, would be to correctly estimate the amount of translational slippage by using only tactile sensing.

An interesting approach is the sensor fusion of tactile and visual information. A possible setup can include a vision system that tracks the object pose. Such measure may be added to the output equations of the nonlinear observer to accurately estimate the object pose during the sliding.

Finally, one of the main drawbacks of the model-based approaches is the need of parameters. Even if most of them are just fingertip dependent, and thus they can be accurately estimated only once, all the parameters are still a source of uncertainty. An interesting approach that deserves further investigation concerns the online adaptive estimation of the friction parameters. This could be done by using an external position sensor (even a vision system with high latency) and comparing the measured pose with the one estimated by the nonlinear observer.

Appendices

Appendix A

Proofs

A.1 Proof of Proposition 3.1

Proposition 3.1 (Boundedness)**.** *For any u such that $|u| < g(\cdot)$, the rectangle*

$$\mathcal{Z} = \left\{ (\zeta, \omega) \in \mathbb{R}^2 \, : \, |\zeta| \leq \frac{g(\cdot)}{\sigma_0}, \, |\omega| \leq \frac{g(\cdot)}{\sigma_1(\cdot)} \right\} \tag{3.16}$$

is positively invariant (i.e., all the solutions starting in $\mathcal{Z}$ remain in $\mathcal{Z}$) and asymptotically attractive, i.e., $\lim_{t\to\infty} \left\| \begin{bmatrix} \zeta & \omega \end{bmatrix}^T \right\|_{\mathcal{Z}} = 0$, while for any bounded $|u| > g(\cdot)$ the rectangle

$$\mathcal{Z}_u = \left\{ (\zeta, \omega) \in \mathbb{R}^2 \, : \, |\zeta| \leq \frac{|u|}{\sigma_0}, \, |\omega| \leq \frac{|u|}{\sigma_1(\cdot)} \right\} \tag{3.17}$$

is positively invariant.

Proof. Let define a positive definite and proper Lyapunov function candidate as

$$V(\zeta, \omega) = \frac{1}{2} \left(\frac{\sigma_0}{J} \zeta^2 + \omega^2 \right). \tag{A.1}$$

Its time derivative along the trajectories of the system (3.8) – (3.9) is

$$\dot{V}(\zeta, \omega) = -\frac{\sigma_0^2 \zeta^2}{J g(\cdot)} |\omega| + \frac{u}{J} \omega - \frac{\sigma_1(\cdot)}{J} \omega^2. \tag{A.2}$$

In the case $|u| < g(\cdot)$ this function is negative both when $|\zeta| > \frac{g(\cdot)}{\sigma_0}$ and when $|\omega| > \frac{g(\cdot)}{\sigma_1(\cdot)}$. The asymptotic attractiveness follows since $\dot{V} < 0$ outside $\mathcal{Z}$. Analogously, in the case $|u| > g(\cdot)$, $\dot{V}$ is negative both when $|\zeta| > \frac{|u|}{\sigma_0}$ and when $|\omega| > \frac{|u|}{\sigma_1(\cdot)}$, and in this case $\mathcal{Z}_u$ is asymptotically attractive. $\square$

A.2 Proof of Theorem 3.1

Theorem 3.1 (Global Asymptotic Stability of Equilibrium (3.20))**.** *Consider the system* (3.8) – (3.9) *and assume a constant input* $u = \bar{u}$ *such that* $|\bar{u}| < g(\cdot)$ *and a constant* $f_n > 0$ *and* c *such that the functions* $g(\cdot)$ *and* $\sigma(\cdot)$ *are constant. Then the solution of the system* (3.8) – (3.9) *converges globally asymptotically to* (3.20).

Proof. Note that according to Proposition 3.1, the set $\mathcal{Z}$ is attractive, and thus to prove the GAS of the equilibrium point it is sufficient to show that as soon as the solution enters $\mathcal{Z}$ it converges asymptotically to the equilibrium point. To this aim, translate the coordinates defining $\boldsymbol{x}$ as follows

$$\boldsymbol{x} = \begin{pmatrix} x_1 & x_2 \end{pmatrix}^T = \begin{pmatrix} \zeta - \frac{\bar{u}}{\sigma_0} & \omega \end{pmatrix}. \tag{A.3}$$

Letting

$$\begin{aligned} k &= \frac{\sigma_0}{J} > 0 \\ \nu &= \frac{\sigma_1(\cdot)}{J} > 0 \\ \alpha &= \frac{\bar{u}}{g(\cdot)} \\ \Delta u &= u - \bar{u}, \end{aligned} \tag{A.4}$$

system (3.8) – (3.9) becomes

$$\dot{\boldsymbol{x}} = \boldsymbol{A}\boldsymbol{x} - \boldsymbol{r}(\boldsymbol{x}) + \boldsymbol{b}\Delta u \tag{A.5}$$

where

$$\begin{aligned} \boldsymbol{A} &= \begin{pmatrix} 0 & 1 \\ -k & -\nu \end{pmatrix} \\ \boldsymbol{r}(\boldsymbol{x}) &= \begin{pmatrix} \left(\alpha + \frac{\sigma_0}{g(\cdot)} x_1\right) |x_2| \\ 0 \end{pmatrix} \\ \boldsymbol{b} &= \begin{pmatrix} 1 \\ \frac{1}{J} \end{pmatrix}. \end{aligned} \tag{A.6}$$

Moreover, define the translated domain of $\mathcal{Z}$

$$\mathcal{X} = \left\{ \boldsymbol{x} \in \mathbb{R}^2 \, : \, -\frac{g(\cdot)}{\sigma_0}(1+\alpha) < x_1 < \frac{g(\cdot)}{\sigma_0}(1+\alpha) \right\}. \tag{A.7}$$

Now, letting $\Delta u = 0$, 0-*stability* (Sontag 2008) of the system (A.5) is examined. Preliminarily, observe that in this case the solution of (A.5) is continuously differentiable. Note how $\forall \boldsymbol{x} \in \mathcal{X}$, the following inequality holds

$$\left| \alpha + \frac{\sigma_0}{g(\cdot)} x_1 \right| < 1. \tag{A.8}$$

To define the candidate Lyapunov-like function (Branicky 1998), define two open half-strips in $\mathbb{R}^2$

$$\mathcal{X}_1 = \{\boldsymbol{x} \in \mathcal{X} \,:\, x_2 > 0\} \cup \{\boldsymbol{0}\} \tag{A.9}$$
$$\mathcal{X}_2 = \{\boldsymbol{x} \in \mathcal{X} \,:\, x_2 < 0\} \cup \{\boldsymbol{0}\} \tag{A.10}$$

Of course it is

$$\bar{\mathcal{X}}_1 \cup \bar{\mathcal{X}}_2 = \mathcal{X} \tag{A.11}$$

where the symbol $\bar{\mathcal{X}}$ denotes the closure of the set $\mathcal{X}$. Let

$$V(\boldsymbol{x}) = \begin{cases} V_1(\boldsymbol{x}) = \boldsymbol{x}^T \boldsymbol{P} \boldsymbol{x} + \frac{1}{2}\beta_1 x_1^2, & \text{if } \boldsymbol{x} \in \mathcal{X}_1 \\ V_2(\boldsymbol{x}) = \boldsymbol{x}^T \boldsymbol{P} \boldsymbol{x} - \frac{1}{2}\beta_2 x_1^2, & \text{if } \boldsymbol{x} \in \mathcal{X}_2 \end{cases} \tag{A.12}$$

with

$$\begin{aligned} \boldsymbol{P} = &\begin{pmatrix} p_1 & p_2 \\ p_2 & p_3 \end{pmatrix} \\ &p_1, p_3 > 0 \\ &\quad \beta_1 > -2p_1 \\ &\quad \beta_2 < 2p_1 \\ &\quad p_2^2 < p_3(p_1 + \frac{1}{2}\min(\beta_1, -\beta_2)). \end{aligned} \tag{A.13}$$

The choice of $\boldsymbol{P}$, β_1 and β_2 above implies that

$$V(\boldsymbol{x}) > 0 \quad \forall \boldsymbol{x} \in \{\mathcal{X}_1 \cup \mathcal{X}_2\} \setminus \{\boldsymbol{0}\}. \tag{A.14}$$

Note also that $V(\boldsymbol{x})$ is undefined on the boundary $\bar{\mathcal{X}}_1 \cap \bar{\mathcal{X}}_2$ (the axis $x_2 = 0$) and discontinuous in its neighborhood, except at the origin, where it is $V(\boldsymbol{x}) = 0$. Nevertheless, note that $V_1(\boldsymbol{x})$ and $V_2(\boldsymbol{x})$ are well-defined in $\bar{\mathcal{X}}_1$ and $\bar{\mathcal{X}}_2$, respectively. It is easy to compute the time derivative of $V_2(\boldsymbol{x})$, $\boldsymbol{x} \in \bar{\mathcal{X}}_2$ along the trajectories of the system (A.5) as

$$\dot{V}_2(\boldsymbol{x}) = \boldsymbol{x}^T(\boldsymbol{P}\boldsymbol{A} + \boldsymbol{A}^T\boldsymbol{P})\boldsymbol{x} - \beta_2 x_1 \dot{x}_1 + 2\boldsymbol{x}^T\boldsymbol{P}\boldsymbol{r}(\boldsymbol{x}). \tag{A.15}$$

Since $\boldsymbol{A}$ is Hurwitz then, chosen the positive definite matrix

$$\boldsymbol{Q} = \begin{pmatrix} q_1 & 0 \\ 0 & q_3 \end{pmatrix}, \quad q_1, q_3 > 0 \tag{A.16}$$

the Lyapunov equation

$$\boldsymbol{P}\boldsymbol{A} + \boldsymbol{A}^T\boldsymbol{P} = -\boldsymbol{Q} \tag{A.17}$$

has the unique positive definite solution $\boldsymbol{P}$ with

$$\begin{aligned} p_1 &= \frac{\nu^2 + k}{2k\nu} q_1 + \frac{k}{2\nu} q_3 \\ p_2 &= \frac{q_1}{2k} \\ p_3 &= \frac{1}{2k\nu} q_1 + \frac{1}{2\nu} q_3. \end{aligned} \tag{A.18}$$

Note that in view of the constraints in (A.13), q_1 has to be selected such as

$$0 < q_1 < \sqrt{p_3 \left(p_1 + \frac{1}{2} \min(\beta_1, -\beta_2) \right)}. \tag{A.19}$$

Moreover, $\dot{V}_2(\boldsymbol{x})$ can be written as

$$\dot{V}_2(\boldsymbol{x}) = -\boldsymbol{x}^T \tilde{\boldsymbol{Q}}_2(\boldsymbol{x})\boldsymbol{x}, \tag{A.20}$$

with

$$\tilde{\boldsymbol{Q}}_2(\boldsymbol{x}) = \begin{pmatrix} q_1 - (\beta_2 - 2p_1)\frac{\sigma_0}{g(\cdot)} |x_2| & \frac{1}{2}(1+\alpha)\beta_2 - p_1\alpha \\ \frac{1}{2}(1+\alpha)\beta_2 - p_1\alpha & q_3 - 2p_2 \left(\alpha + \frac{\sigma_0}{g(\cdot)} x_1 \right) \end{pmatrix}. \tag{A.21}$$

$\tilde{\boldsymbol{Q}}_2(\boldsymbol{x})$ is positive definite $\forall \boldsymbol{x} \in \bar{\mathcal{X}}_2$ provided that q_1 is selected according to (A.19) and

$$\begin{aligned} \beta_2 &= \frac{2\alpha}{1+\alpha} p_1 \\ q_3 &> \frac{q_1}{k}. \end{aligned} \tag{A.22}$$

Note that the choice of β_2, necessary to nullify the off-diagonal entries, satisfies the constraints in (A.13) in view of the assumption $|\bar{u}| < g(\cdot)$, which also implies that the first entry on the diagonal is positive, and, finally, the second entry on the diagonal is positive in view of the inequality (A.8). Analogously, for $\boldsymbol{x} \in \bar{\mathcal{X}}_1$, the time derivative of $V_1(\boldsymbol{x})$ along the system trajectories can be computed as

$$\dot{V}_1(\boldsymbol{x}) = -\boldsymbol{x}^T \tilde{\boldsymbol{Q}}_1(\boldsymbol{x})\boldsymbol{x} \tag{A.23}$$

with

$$\tilde{\boldsymbol{Q}}_1(\boldsymbol{x}) = \begin{pmatrix} q_1 + \frac{\sigma_0}{g(\cdot)}\left|x_2\right|(\beta_1 + 2p_1) & -\frac{1}{2}(1-\alpha)\beta_1 + p_1\alpha \\ -\frac{1}{2}(1-\alpha)\beta_1 + p_1\alpha & q_3 - 2p_2\left(\alpha + \frac{\sigma_0}{g(\cdot)}x_1\right) \end{pmatrix}. \tag{A.24}$$

$\tilde{\boldsymbol{Q}}_1(\boldsymbol{x})$ is positive definite $\forall \boldsymbol{x} \in \bar{\mathcal{X}}_1$ provided that q_1 is selected according to (A.19) and

$$\begin{aligned} \beta_1 &= \frac{2\alpha}{1-\alpha}p_1 \\ q_3 &> \frac{q_1}{k}, \end{aligned} \tag{A.25}$$

which again satisfy the constrains in (A.13) in view of the assumption $|\bar{u}| < g(\cdot)$ and the inequality (A.8). In conclusion, the candidate Lyapunov-like function is always decreasing both for $\boldsymbol{x} \in \mathcal{X}_1$ and $\boldsymbol{x} \in \mathcal{X}_2$. It remains to establish the behavior of the system when the trajectories hit the boundary $x_2 = 0$. Denote with $\{t_n\}_{n\in\mathbb{N}}$ the sequence of time instants in which $x_2(t_n) = 0$. Inequality (A.8) implies that $\dot{\boldsymbol{x}}_1(t) \geq 0$ when $\boldsymbol{x}(t) \in \bar{\mathcal{X}}_1$, while $\dot{\boldsymbol{x}}_1(t) \leq 0$ when $\boldsymbol{x}(t) \in \bar{\mathcal{X}}_2$. Moreover, $\dot{x}_1(t) = 0$ when $\boldsymbol{x}(t)$ is on the boundary $x_2 = 0$, that means for all t such that $x_2(t) = 0$, $x_1(t)$ has a maximum or a minimum. Without loss of generality, we can assume that in t_n the trajectory is passing from $\mathcal{X}_1$ to $\mathcal{X}_2$ (see Fig. A.1), that means $\boldsymbol{x}(t) \in \mathcal{X}_1$, $t \in (t_{n-1}, t_n)$ and $\boldsymbol{x}(t) \in \mathcal{X}_2$, $t \in (t_n, t_{n+1})$, and assume $x_1(t_n) > 0$. Moreover, in view of the second system equation, $\dot{x}_2(t_n) = -kx_1(t_n) < 0$ and thus $x_2(t)$, $t > t_n$ is decreasing until the trajectory hits the isocline $x_2 = -\frac{k}{v}x_1$. Next, x_2 starts increasing, until the trajectory intersects the axis $x_2 = 0$, with $x_1(t_{n+1}) < 0$. Finally, the two sequences $\{V_1(\boldsymbol{x}(t_n))\}_{n\in\mathbb{N}}$ and $\{V_2(\boldsymbol{x}(t_n))\}_{n\in\mathbb{N}}$ will be shown to be monotonically decreasing. Since in $t = t_n$ the state trajectory is on the boundary, in view of their definition in (A.12), it is

$$V_1(\boldsymbol{x}(t_n)) = \left(p_1 + \frac{1}{2}\beta_1\right)x_1^2(t_n) \tag{A.26}$$

$$V_2(\boldsymbol{x}(t_n)) = \left(p_1 - \frac{1}{2}\beta_2\right)x_1^2(t_n). \tag{A.27}$$

Since both $\dot{V}_1(\boldsymbol{x}) < 0$, $\boldsymbol{x} \in \bar{\mathcal{X}}_1$ and $\dot{V}_2(\boldsymbol{x}) < 0$, $\boldsymbol{x} \in \bar{\mathcal{X}}_2$, then $\{|x_1(t_n)|\}_{n\in\mathbb{N}}$ is a monotonically decreasing sequence. Therefore, in view of (A.26) – (A.27), the

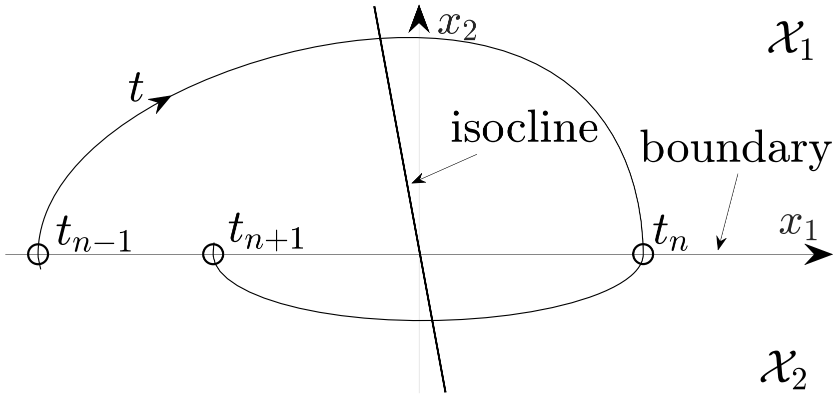

Figure A.1: Definition of the switching time instants t_n: circles identify points $\boldsymbol{x}(t_n) \in \bar{\mathcal{X}}_1 \cap \bar{\mathcal{X}}_2$.

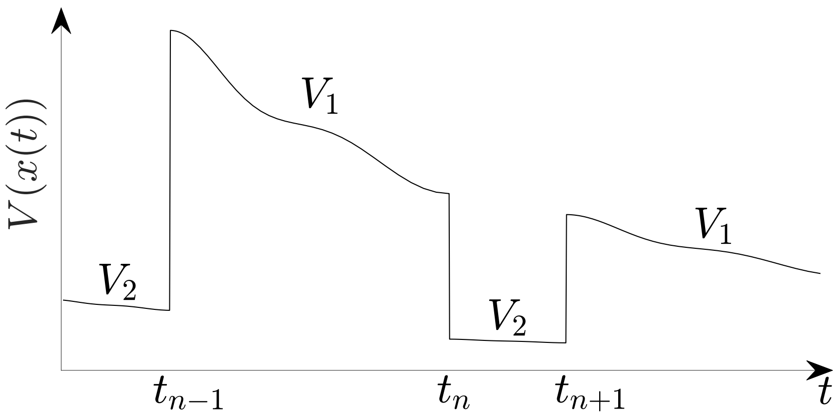

Figure A.2: Typical time history of the discontinuous Lyapunov function $V(\boldsymbol{x}(t))$.

two sequences$\{V_1(\boldsymbol{x}(t_n))\}_{n\in\mathbb{N}}$ and $\{V_2(\boldsymbol{x}(t_n))\}_{n\in\mathbb{N}}$ are monotonically decreasing too. Moreover, recalling that $V(\boldsymbol{x}(t))$ is decreasing in all the intervals $(t_n,\, t_{n+1})$, then

$$\lim_{t\to\infty} V(\boldsymbol{x}(t)) = 0. \tag{A.28}$$

A typical behaviour of the discontinuous Lyapunov function along the system trajectories is reported in Fig. A.2 for the case $\alpha > 0$, implying that $V_1(\boldsymbol{x}) > V_2(\boldsymbol{x})$, otherwise, for $\alpha < 0$, it is $V_1(\boldsymbol{x}) < V_2(\boldsymbol{x})$. In view of the positive definiteness of $V(\boldsymbol{x})$, the limit above obviously implies that $\boldsymbol{x}(t)$ converges to the origin, that is asymptotically stable in the sense of Lyapunov (Branicky 1998; Zhao and Hill 2008). $\square$

A.3 Proof of Proposition 3.2

Proposition 3.2 (Instability of Equilibrium (3.20)). *Assuming a constant input $u = \bar{u}$, if $|\bar{u}| > g(\cdot)$ and if*

$$\sigma_0 > \frac{(\sigma_1(\cdot))^2}{4J\left(\frac{|\bar{u}|}{g(\cdot)} - 1\right)} \tag{3.23}$$

the equilibrium point (3.20) *of the system* (3.8) – (3.9) *is unstable.*

Proof. As in the proof of Theorem 3.1, consider the change of coordinates (A.3) and the change of variables (A.4). Condition (3.23) becomes

$$k > \frac{\nu^2}{4(\alpha - 1)}. \tag{A.29}$$

The proof will be carried out with $\alpha > 1$, but the case $\alpha < -1$ is perfectly analogous. Let $\mathcal{W} \subset \mathbb{R}^2$ be a circle of radius r and center in the origin, where the continuously differentiable function

$$V(\boldsymbol{x}) = \frac{1}{2}x_1^2 x_2^2 \tag{A.30}$$

is positive semidefinite. Its time derivative along the trajectories of the system (3.8) – (3.9) is

$$\dot{V}(\boldsymbol{x}) = x_1 x_2^2 \left(x_2 - \left(\alpha + \frac{\sigma_0}{g(\cdot)} x_1 \right) |x_2| \right) - x_1^2 x_2 (k x_1 + \nu x_2) \tag{A.31}$$

Let

$$\mathcal{Y} = \left\{ \boldsymbol{x} \in \mathbb{R}^2 \,:\, x_1 \leq 0 \text{ and } x_2 \geq 0 \right\}, \tag{A.32}$$

then $\dot{V}(\boldsymbol{x})$ with $\boldsymbol{x} \in \mathcal{Y}$ can rewritten as

$$\dot{V}(\boldsymbol{x}) = -|x_1|\,|x_2| \left(\frac{\sigma_0}{g(\cdot)} |x_1|\,|x_2|^2 - \boldsymbol{y}^T \boldsymbol{F} \boldsymbol{y} \right), \tag{A.33}$$

where

$$\begin{aligned} \boldsymbol{y} &= \begin{pmatrix} |x_1| & |x_2| \end{pmatrix}^T \\ \boldsymbol{F} &= \begin{pmatrix} k & -\frac{\nu}{2} \\ -\frac{\nu}{2} & \alpha - 1 \end{pmatrix}. \end{aligned} \tag{A.34}$$

In view of the assumption (A.29), the matrix $\boldsymbol{F}$ is positive definite and thus

$$\boldsymbol{y}^T \boldsymbol{F} \boldsymbol{y} \geq \lambda_{\min}(\boldsymbol{F}) \left\| \boldsymbol{y} \right\|^2 , \tag{A.35}$$

being $\lambda_{\min}(\boldsymbol{F})$ the minimum eigenvalue of the matrix $\boldsymbol{F}$. This implies that $\dot{V}(\boldsymbol{x})$ is positive definite in the circular sector of radius $\lambda_{\min}(\boldsymbol{F})$ centered in the origin with $x_1 < 0$ and $x_2 > 0$. Therefore, by choosing the radius r of $\mathcal{W}$ equal to $\lambda_{\min}(\boldsymbol{F})$, the function $V(\boldsymbol{x})$ satisfies the assumptions of the Chetaev instability theorem (Khalil 2002, p. 124), i.e.,

i) $V(\boldsymbol{x})$ and $\dot{V}(\boldsymbol{x})$ are positive in $\{\mathcal{W} \cap \mathcal{Y}\} \setminus \{\boldsymbol{0}\}$

ii) $V(\boldsymbol{x})$ is zero in the origin and in the intersection between the boundary of $\mathcal{Y}$ and the circle $\mathcal{W}$, i.e., $\partial\mathcal{Y} \cap \mathcal{W}$

therefore the origin in unstable. Note that the proof with $\alpha < -1$ can be carried out in the same way by choosing the domain

$$\mathcal{Y} = \left\{ \boldsymbol{x} \in \mathbb{R}^2 \, : \, x_1 \geq 0 \text{ and } x_2 \leq 0 \right\} . \tag{A.36}$$

□

A.4 Proof of Proposition 3.3

Proposition 3.3 (Stability of Equilibrium (3.21))**.** *Considering a constant $u = \bar{u}$ and a constant $f_n > 0$ and c such that the functions $g(\cdot)$ and $\sigma(\cdot)$ are constant, the point* (3.21) *is an asymptotically stable equilibrium state of the system* (3.8) – (3.9) *with $\bar{u} > g(\cdot)$. Moreover, for any given scalar λ let*

$$\omega_0 = \frac{\sigma_0 g(\cdot)}{4J\lambda^2\sigma_1(\cdot)} . \tag{3.24}$$

Then an estimate of the domain of attraction is

$$\mathcal{D} = \left\{ (\zeta, \omega) \in \mathbb{R}^2 \, : \, \lambda^2 \left(\zeta - \frac{g(\cdot)}{\sigma_0} \right)^2 + (\omega - \bar{\omega})^2 < (\bar{\omega} - \omega_0)^2 \right\} . \tag{3.25}$$

Proof. Again, the translated system is defined as follows

$$\boldsymbol{x} = \begin{pmatrix} x_1 & x_2 \end{pmatrix}^T = \begin{pmatrix} \zeta - \frac{g(\cdot)}{\sigma_0} & \omega - \bar{\omega} \end{pmatrix}^T . \tag{A.37}$$

As in the proof of Theorem 3.1, considering the symbols defined in (A.4), the equations of the system (3.8) – (3.9) can be rewritten as

$$\dot{x}_1 = x_2 + \bar{\omega} - \frac{\sigma_0}{g(\cdot)}\left(x_1 + \frac{g(\cdot)}{\sigma_0}\right)|x_2 + \bar{\omega}| \tag{A.38}$$

$$\dot{x}_2 = -kx_1 - \nu x_2. \tag{A.39}$$

Let

$$V(\boldsymbol{x}) = \frac{1}{2}\boldsymbol{x}^T \begin{pmatrix} \lambda^2 & 0 \\ 0 & 1 \end{pmatrix} \boldsymbol{x} \tag{A.40}$$

be a candidate Lyapunov function. It is positive definite and proper and its derivative along the trajectories of the system (A.38) – (A.39) is

$$\dot{V}(\boldsymbol{x}) = \boldsymbol{x}^T \begin{pmatrix} \lambda^2 & 0 \\ 0 & 1 \end{pmatrix} \begin{pmatrix} x_2 + \bar{\omega} - \left(x_1 \frac{\sigma_0}{g(\cdot)} + 1\right)|x_2 + \bar{\omega}| \\ -kx_1 - \nu x_2 \end{pmatrix}, \tag{A.41}$$

that, in the domain $\mathcal{D}$, $x_2 > \bar{\omega}$, can be rewritten as

$$\dot{V}(\boldsymbol{x}) = -\lambda^2 \frac{\sigma_0}{g(\cdot)} x_1^2 (x_2 + \bar{\omega}) - kx_1 x_2 - \nu x_2^2. \tag{A.42}$$

Completing the square, this function is negative definite if

$$x_2 + \bar{\omega} > \frac{k^2 g(\cdot)}{4\nu\lambda^2\sigma_0}, \tag{A.43}$$

Moreover, using (A.40), the largest invariant ellipsoid of the form $V(\boldsymbol{x}) = c$ and satisfying $\omega > \omega_0$ is given in (3.25). Hence, for any initial state in the domain $\mathcal{D}$, there exist a value of λ such that the trajectory of the system converges to the origin. The proof for the equilibrium point (3.22) in the case $\bar{u} < -g(\cdot)$ is perfectly analogous. □

A.5 Proof of Proposition 3.4

Proposition 3.4 (Observability)**.** *Let*

$$\mathcal{M} = \left\{(\zeta, \omega) \in \mathbb{R}^2 \,:\, \omega > 0\right\}, \tag{3.27}$$

then the system (3.8) – (3.9) *with output equation* (3.26) *is locally weakly observable (Hermann and Krener 1977) at any initial state* $(\zeta(0), \omega(0)) \in \mathcal{M}$. *Moreover, the same holds in the domain*

$$\mathcal{M}' = \left\{(\zeta, \omega) \in \mathbb{R}^2 \,:\, \omega < 0\right\}. \tag{3.28}$$

Proof. The proof will be carried out in $\mathcal{M}$ since the description in $\mathcal{M}'$ is perfectly analogous. The thesis holds if and only if the following matrix has rank 2 $\forall(\zeta,\, \omega) \in \mathcal{M}$ (Nijmeijer and Schaft 1990)

$$\mathbf{\Theta}(\zeta,\, \omega) = \begin{pmatrix} \mathrm{d}h(\zeta,\, \omega) \\ \mathcal{L}^1_{\boldsymbol{f}}\mathrm{d}h(\zeta,\, \omega) \end{pmatrix} \tag{A.44}$$

where $\mathrm{d}h$ represents the gradient of the function $h(\zeta,\, \omega)$ and $\mathcal{L}^i_{\boldsymbol{f}}$ is the Lie derivative operator of order i along the vector function $\boldsymbol{f}(\zeta,\, \omega)$ whose components are the second members of the equations (3.8) – (3.9). This matrix for $(\zeta,\, \omega) \in \mathcal{M}$ is

$$\mathbf{\Theta}(\zeta,\, \omega) = \begin{pmatrix} \sigma_0 & \sigma_1(\cdot) \\ -\frac{\sigma_0}{J}\sigma_1(\cdot) - \frac{\sigma_0^2}{g(\cdot)}\omega & -\frac{\sigma_1(\cdot)^2}{J} + \sigma_0\left(1 - \frac{\sigma_0}{g(\cdot)}\zeta\right) \end{pmatrix} \tag{A.45}$$

that is full rank for $\omega > 0$ owing to the boundedness property. $\square$

Appendix B

SUNTouch Finger

The slipping control strategy presented in this thesis requires the direct measurement of the friction forces and torque that the robot exchanges with the manipulated objects. This ability is given by the SUNTouch fingers (Fig. B.1), designed and produced internally by the RoboticsLab of Università degli Studi della Campania "Luigi Vanvitelli".

The sensor is based on the working principle firstly designed in (De Maria, C. Natale, and Pirozzi 2012) and refined in (Costanzo, De Maria, et al. 2019). A suitably designed deformable layer is positioned above a discrete number of sensible points (called "taxels"). The external force and moment applied to the sensor yield deformations which are measured by the taxels. The taxels, spatially distributed below the deformable layer, provide a set of signals corresponding to a distributed information (called "tactile map") about the sensor deformations. The whole tactile map allows, after a calibration procedure, to estimate contact force and moment. The taxels have been developed by using an optoelectronic technology, and, in particular, each sensing point is constituted by an emitter and a receiver, mounted side by side, working in reflection mode. The soft pad has been realized by using the silicone molding technology with the molds made with a high-resolution 3D printing manufacturing process. The pad used in this thesis is a hemispherical one with a radius of 0.025 m.

Figure B.2 shows the designed PCB. Each taxel is constituted by a photo-reflector, manufactured by New Japan Radio (code NJL5908AR). The PCB integrates 25 taxels, organized in a 5×5 matrix, with a spatial resolution of 3.55 mm. The LEDs are driven with adjustable current sources (manufacturer code LM334) to improve the stability of the emitted light, by reducing its temperature drift. A resistor transduces the photocurrent measured by the photo-reflector into a voltage that is measured by the 12-bit A/D channels of a microcontroller. The controller communicates the measured voltages to

Figure B.1: The SUNTouch finger.

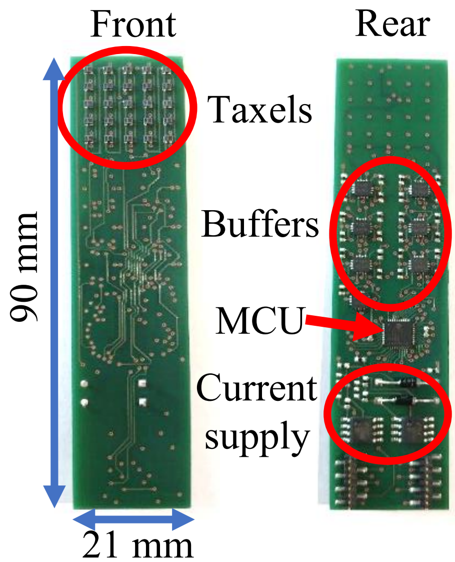

Figure B.2: Front and rear views of the new assembled PCB with the highlighting of the components.

a PC via a serial interface. The resulting sampling frequency is 500 Hz.

The assembled force/tactile sensor is fixed inside a case designed to house the sensor and for installation on the WSG50 finger flange (see Fig. 4.13). Se Appendix C for more details on the WSG50 gripper.

B.1 Sensor Calibration

In order to use the sensor, the taxels voltages have to be transformed into forces and torques. This is achieved by training a FeedForward Neural Network (FF-NN). The critical point is the training data collection. The objective is to estimate the contact wrench in all possible combinations in a large interval of the contact plane orientation. The dimensionality of the problem is large, so there is a significant risk of missed wrench/orientation combinations in the training set. Therefore, a robotized calibration setup has been realized.

The tactile sensor is mounted on a ground-truth force/tactile sensor (ATI NANO43) (see Fig. B.3). A Meca500 robot is programmed to apply all the desired force/torque combinations on the deformable layer with various orientation. At the same time, the wrench measured by the reference sensor and the voltages from the tactile map are stored to build the training data.

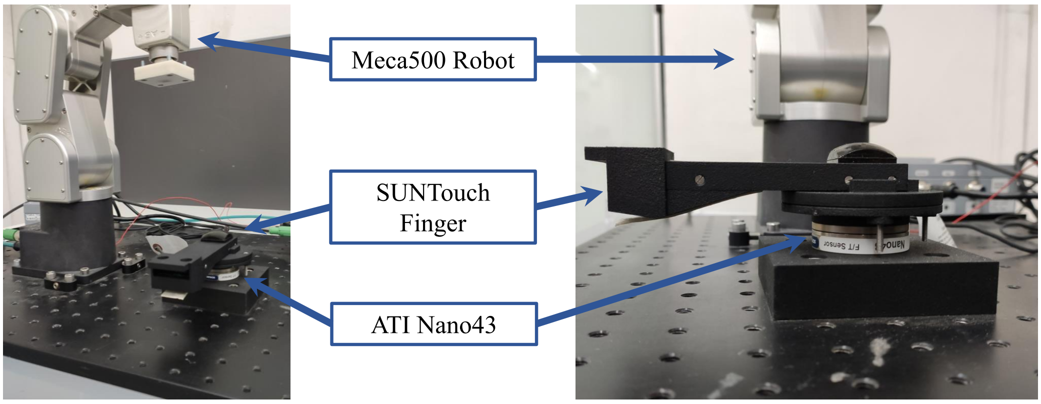

Figure B.3: Setup used to acquire the data for the calibration.

Finally, the data are used to train a FF-NN. The network is made of six hidden layers, each one composed of 90 neurons and a sigmoidal activation function, whereas the output layer has a linear activation function and six neurons.

B.2 Friction Parameter Estimation

As pointed out in Chapter 2, three of the five parameters of the soft contact model, i.e., δ, γ, and k, can be identified by experiments on the sensor pad itself, while μ and β_A have to be estimated through experiments involving the contact between the sensor pad and the manipulated object, e.g., through procedures similar to those described in (Costanzo, De Maria, and C. Natale 2018).

The experimental setup to perform the estimation of δ and γ is the same used for the calibration procedure (Fig. B.3). These two parameters appear in the radius model (2.24), thus it is possible to measure various values of the normal force f_n and the corresponding radius ρ and then minimize the mean square error on the model (2.24). The normal force is directly measured by the ATI reference sensor while the radius can be geometrically computed from the forward kinematics of the robot. In fact, knowing the penetration Δz in the robot moving direction it is possible to geometrically compute the radius of the contact area as

$$\rho = \sqrt{2r_p\Delta z - \Delta z^2} \tag{B.1}$$

where $r_p = 0.025\,\mathrm{m}$ is the radius of the sensor pad.

The plot in Fig. B.4 reports the obtained samples (f_n, ρ) and the interpolating curve of analytic expression as in (2.24), where $\gamma = 0.2545$ and

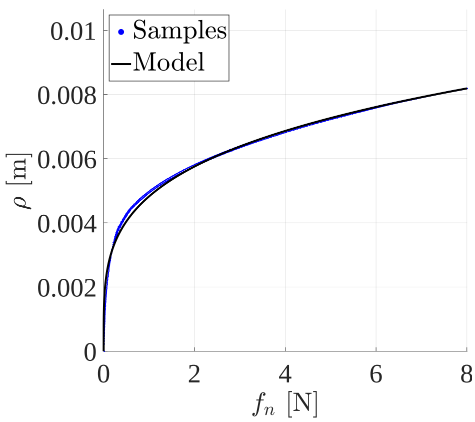

Figure B.4: Samples of (f_n, ρ) acquired to estimate δ and γ.

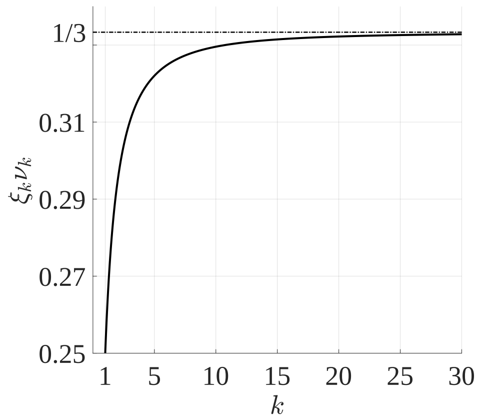

Figure B.5: The product $\xi_k \nu_k$ in function of k.

$\delta = 0.004824\,\mathrm{m/N}^\gamma$ have been estimated by minimizing the mean square error. Not surprisingly, the estimated value of γ is very close to the value 0.259 reported by Xydas and Kao (1999) for a similar silicone rubber.

Concerning the parameter k, first of all, observing Fig. 2.5 allows appreciating how the normalized Limit Surface is only slightly sensitive to the variations of k, therefore, it is not worth investigating a specific procedure to accurately estimate k. The relationship (2.28) implies

$$\xi_k \nu_k = \frac{\tau_{n\max}}{2\mu\delta f_n^{\gamma+1}}. \tag{B.2}$$

Recalling (2.25) and (2.27), the product $\xi_k \nu_k$ is an analytic function of the k variable and it is represented in Fig. B.5. By using a rigid contact object it is possible to apply rotations and translations to estimate $\tau_{n\max}$ and μ respectively for various values of the normal force and then compute $\xi_k \nu_k$ from (B.2). On the SUNTouch sensor pad, the procedure yields the range [0.3036, 0.3214] for the product $\xi_k \nu_k$ that corresponds to a possible variation of k in the interval [2.478, 4.817]. Therefore the value $k = 4$ has been selected.

The object dependent parameters μ and β_A can be estimated through a simple pure translational motion measuring the forces and the robot translational velocity v_t. The friction tangential force measured during this motion is

$$f_{tf} = \mu f_n + \beta_A \pi \rho^2 v_t, \tag{B.3}$$

i.e., the superposition of the maximum dry translational friction and the viscous one. μ can be computed as

$$\mu = \frac{f_{tf}}{f_n} \tag{B.4}$$

at the end of the translational motion, when $v_t = 0$ and the residual force is the maximum dry friction. Finally, β_A can be estimated by inverting (B.3), namely,

$$\beta_A = \frac{f_{tf} - \mu f_n}{\pi \rho^2 v_t}. \tag{B.5}$$

B.3 Using the measures of two fingers

As stated in Remark 3.4 the formulation made in Chapter 3 can be used also in the case of a parallel jaw gripper equipped with two sensorized fingertips. We adopt the concept of Grasp Limit Surface by Shi, Woodruff, et al. (2017) and assume a perfect geometrical and physical symmetry of the two contacts. This is equivalent to define a unique measured external wrench $(\boldsymbol{f}_m, \boldsymbol{\tau}_m)$ and internal grasp force f_n as follows

$$\boldsymbol{f}_m = \boldsymbol{f}_{m1} + \boldsymbol{f}_{m2} \tag{B.6}$$

$$\boldsymbol{\tau}_m = \boldsymbol{\tau}_{m1} + \boldsymbol{\tau}_{m2} \tag{B.7}$$

$$f_n = |f_{n1}| + |f_{n2}| \tag{B.8}$$

where $\boldsymbol{f}_{mi}$ and $\boldsymbol{\tau}_{mi}$ are the force and torque measured by the i-th sensorized finger both expressed in a common frame located at the CoP with the z-axis in the gripper actuation direction; and f_{n_i} is the normal load measured by the i-th finger, namely the z component of $\boldsymbol{f}_{m_i}$. Note that, expressed in the common frame, f_{n1} and f_{n2} have opposite sign because each finger pushes against the slider from an opposite direction, thus the absolute value in (B.8) is needed to compute a positive internal grasp force.

In case the two contacts are not perfectly symmetric, the external wrench can be obtained by following the procedure detailed in Section 2 of (Costanzo, De Maria, and C. Natale 2020b).

Appendix C

Experimental Setup

In all the experiments of this thesis, the grasp force is actuated by a WSG50 gripper (Fig. 4.13). It can be programmed via a LUA script to receive velocity commands through an Ethernet interface. Due to limitations of the LUA interpreter, the velocity commands can be received at 50 Hz only. The gripper is force controlled via a feedback loop closed on the normal force f_n measured by the sensorized fingers (Appendix B).

Moreover, the gripper is not able to actuate velocity commands below 5 mm/s. Any command below that value is clipped to zero by the gripper driver. This will slightly affect the performances of the low-level grasp force control loop.

The gripper is mounted on a LBR IIWA 7 (Fig. C.1) through a custom 3D printed flange that permits to mount also an Intel D435i RGB-D camera (see Fig. 4.13). The camera is used only in the visual servo algorithm of Section 4.3.

The robot is mounted on the Kuka action cube (Fig. C.1) which also hosts few shelves simulating a supermarket scenario.

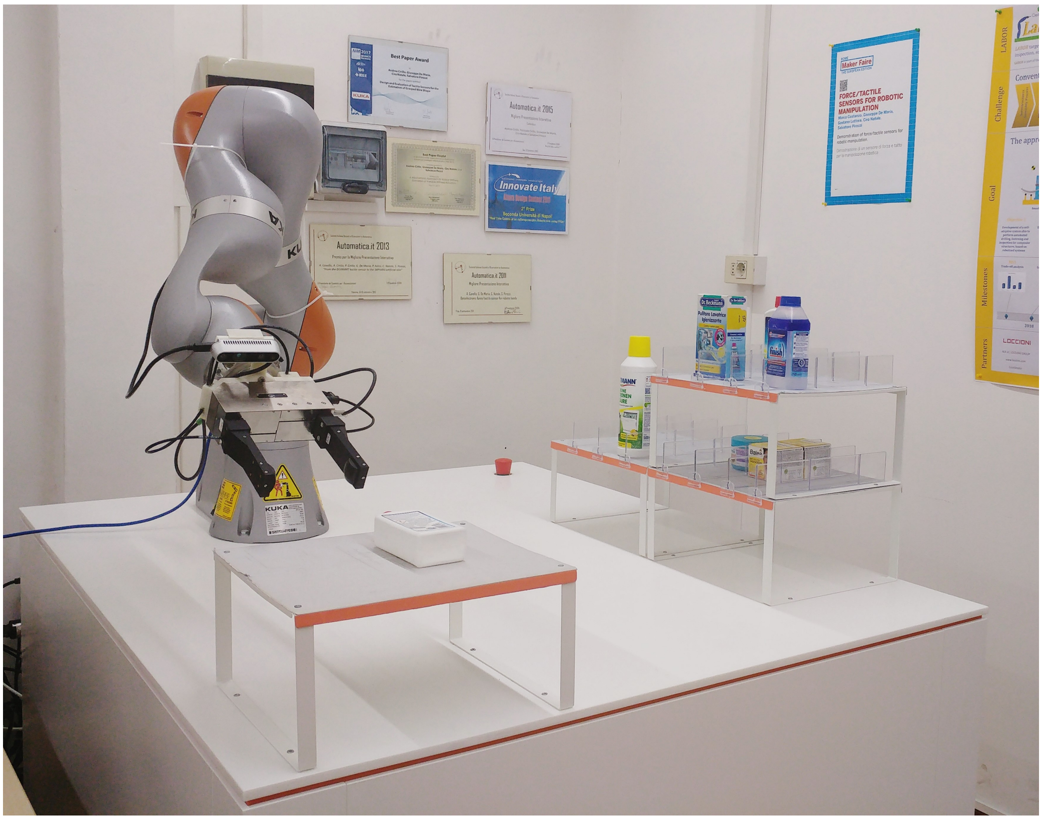

Figure C.1: Kuka action cube.

Appendix D

Multimedia Links

D.1 Video of Section 4.1.1

The video of the experiments in Section 4.1.1 can be found at the following link

`https://www.youtube.com/watch?v=pGLi5sqFMwI`

D.2 Video of Section 4.4

The video of the experiments in Section 4.4 can be found at the following link

`https://youtu.be/9PYlYEkQnh8`

For convenience, Tab. D.1 contains the links to the video starting from the single experiment.

Experiment	Link
Experiment 1	`https://youtu.be/9PYlYEkQnh8`
Experiment 2	`https://youtu.be/9PYlYEkQnh8?t=54`
Experiment 3	`https://youtu.be/9PYlYEkQnh8?t=94`
Experiment 4	`https://youtu.be/9PYlYEkQnh8?t=144`

Table D.1: Links to video of Section 4.4.

Appendix E

Source Code

The algorithms presented in this thesis have been written under the ROS framework and are available on GitHub.

slipping_control

The repository is available at the following URL

`https://github.com/marcocostanzo/slipping_control`

This repository provides all the computation needed for the Limit Surface (Chapter 2) and the Dynamic Planar Slider model (Chapter 3).

More in detail, this package provides:

- estimation of $\tilde{c}$ through the algorithm (2.80);
- implementation of the nonlinear observer (3.32) – (3.33) discretized via a 4-order Runge–Kutta method;
- slipping avoidance algorithm (Section 3.5);
- pivoting algorithm of Section 3.6.

The functionalities are triggered via ROS actions and services.

sun_pivoting_planner

The repository is available at the following URL

`https://github.com/marcocostanzo/sun_pivoting_planner`

This repository provides:

- the motion/manipulation planner of Section 4.2;

- the higher-level task/grasp planner of Section 4.3.

The planners are written on top of the MoveIT! framework. The ROS nodes expose their functionalities via ROS actions.

Bibliography

Antonova, R., S. Cruciani, C. Smith, and D. Kragic (2017). *Reinforcement Learning for Pivoting Task*.

Armstrong-Hélouvry, B. (1991). *Control of Machines with Friction*. Springer US.

Armstrong-Hélouvry, B., P. Dupont, and C. Canudas De Wit (1994). "A survey of models, analysis tools and compensation methods for the control of machines with friction". In: *Automatica* 30.7, pp. 1083–1138. ISSN: 0005-1098.

Beeson, P. and B. Ames (2015). "TRAC-IK: An open-source library for improved solving of generic inverse kinematics". In: *2015 IEEE-RAS 15th International Conference on Humanoid Robots (Humanoids)*, pp. 928–935.

Berenson, D., S. Srinivasa, D. Ferguson, and J. Kuffner (2009). "Manipulation planning on constraint manifolds". In: *2009 IEEE International Conference on Robotics and Automation (ICRA)*, pp. 625–632.

Bliman, P.-A. (1992). "Mathematical study of the Dahl's friction model". In: *European Journal of Mechanics Series A/Solids* 11.6, pp. 835–848.

Bottarel, F., G. Vezzani, U. Pattacini, and L. Natale (2020). "GRASPA 1.0: GRASPA is a Robot Arm graSping Performance BenchmArk". In: *IEEE Robotics and Automation Letters* 5.2, pp. 836–843.

Branicky, M. S. (1998). "Multiple Lyapunov functions and other analysis tools for switched and hybrid systems". In: *IEEE Transactions on Automatic Control* 43.4, pp. 475–482.

Canudas De Wit, C., H. Olsson, K. J. Astrom, and P. Lischinsky (1995). "A new model for control of systems with friction". In: *IEEE Transactions on Automatic Control* 40.3, pp. 419–425.

Cavallo, A., M. Costanzo, G. De Maria, and C. Natale (2020). "Modeling and slipping control of a planar slider". In: *Automatica* 115.108875. ISSN: 0005-1098.

Chavan-Dafle, N., R. Holladay, and A. Rodriguez (2020). "Planar in-hand manipulation via motion cones". In: *The International Journal of Robotics Research* 39.2-3, pp. 163–182.

Chavan-Dafle, N. and A. Rodriguez (2015). "Prehensile pushing: In-hand manipulation with push-primitives". In: *2015 IEEE/RSJ International Conference on Intelligent Robots and Systems (IROS)*, pp. 6215–6222.

Chavan-Dafle, N., A. Rodriguez, R. Paolini, B. Tang, S. Srinivasa, M. Erdmann, M. Mason, I. Lundberg, H. Staab, and T. Fuhlbrigge (2014). "Extrinsic dexterity: In-hand manipulation with external forces". In: *2014 IEEE International Conference on Robotics and Automation (ICRA)*, pp. 1578–1585.

Chitta, S., I. Sucan, and S. Cousins (2012). "MoveIt! [ROS Topics]". In: *IEEE Robotics Automation Magazine* 19.1, pp. 18–19.

Cirillo, A., P. Cirillo, G. De Maria, C. Natale, and S. Pirozzi (2017). "Control of linear and rotational slippage based on six-axis force/tactile sensor". In: *2017 IEEE International Conference on Robotics and Automation (ICRA)*, pp. 1587–1594.

Controzzi, M., C. Cipriani, and M. C. Carrozza (2014). "Design of Artificial Hands: A Review". In: *The Human Hand as an Inspiration for Robot Hand Development*. Ed. by R. Balasubramanian and V. J. Santos. Cham: Springer International Publishing, pp. 219–246. ISBN: 978-3-319-03017-3.

Costanzo, M., G. De Maria, G. Lettera, and C. Natale (2020). "Grasp Control for Enhancing Dexterity of Parallel Grippers". In: *2020 IEEE International Conference on Robotics and Automation (ICRA)*. 31 May - 31 August. Paris, France, pp. 524–530.

Costanzo, M., G. De Maria, and C. Natale (2018). "Slipping Control Algorithms for Object Manipulation with Sensorized Parallel Grippers". In: *2018 IEEE International Conference on Robotics and Automation (ICRA)*, pp. 7455–7461.

Costanzo, M., G. De Maria, and C. Natale (2020a). "Control of Sliding Velocity in Robotic Object Pivoting Based on Tactile Sensing". In: *IFAC-PapersOnLine*. 21th IFAC World Congress, Berlin, Germany, July 12-17, 2020, pp. 10085–10090.

Costanzo, M., G. De Maria, and C. Natale (2020b). "Two-Fingered In-Hand Object Handling Based on Force/Tactile Feedback". In: *IEEE Transactions on Robotics* 36.1, pp. 157–173.

Costanzo, M., G. De Maria, C. Natale, and S. Pirozzi (Feb. 2019). "Design and Calibration of a Force/Tactile Sensor for Dexterous Manipulation". In: *Sensors* 19.4, p. 966. ISSN: 1424-8220.

Costanzo, M., S. Stelter, C. Natale, S. Pirozzi, G. Bartels, A. Maldonado, and M. Beetz (2020). "Manipulation Planning and Control for Shelf Replenishment". In: *IEEE Robotics and Automation Letters* 5.2, pp. 1595–1601.

Cruciani, S., B. Sundaralingam, K. Hang, V. Kumar, T. Hermans, and D. Kragic (2020). "Benchmarking In-Hand Manipulation". In: *IEEE Robotics and Automation Letters* 5.2, pp. 588–595.

Cruciani, S., H. Yin, and D. Kragic (2020). "In-Hand Manipulation of Objects with Unknown Shapes". In: *ICRA*.

D'Amore, A., G. De Maria, L. Grassia, C. Natale, and S. Pirozzi (2011). "Silicone-rubber-based tactile sensors for the measurement of normal and tangential components of the contact force". In: *Journal of Applied Polymer Science* 122.6, pp. 3757–3769.

Dahl, P. R. (1968). *A solid friction model.* Tech. rep. El Segundo, CA.

De Maria, G., C. Natale, and S. Pirozzi (2012). "Force/tactile sensor for robotic applications". In: *Sensors and Actuators A: Physical* 175, pp. 60–72. ISSN: 0924-4247.

Dragan, A., N. Ratliff, and S. Srinivasa (2011). "Manipulation planning with goal sets using constrained trajectory optimization". In: *2011 IEEE International Conference on Robotics and Automation*, pp. 4582–4588.

Drazin, P. G. (2002). *Nonlinear Systems.* Cambridge Texts in Applied Mathematics. Cambridge University Press.

Engeberg, E. D. and S. G. Meek (2013). "Adaptive Sliding Mode Control for Prosthetic Hands to Simultaneously Prevent Slip and Minimize Deformation of Grasped Objects". In: *IEEE/ASME Transactions on Mechatronics* 18.1, pp. 376–385.

Fang, Z., G. Bartels, and M. Beetz (2016). "Learning models for constraint-based motion parameterization from interactive physics-based simulation". In: *2016 IEEE/RSJ International Conference on Intelligent Robots and Systems (IROS)*, pp. 4005–4012.

Funabashi, S., A. Schmitz, S. Ogasa, and S. Sugano (2020). "Morphology Specific Stepwise Learning of In-Hand Manipulation With a Four-Fingered Hand". In: *IEEE Transactions on Industrial Informatics* 16.1, pp. 433–441.

Goyal, S. (1989). *Planar sliding of a rigid body with dry friction: limit surfaces and dynamics of motion.* Cornell University, Jan.

Goyal, S., A. Ruina, and J. Papadopoulos (1991a). "Planar sliding with dry friction Part 1. Limit surface and moment function". In: *Wear* 143.2, pp. 307–330. ISSN: 0043-1648.

Goyal, S., A. Ruina, and J. Papadopoulos (1991b). "Planar sliding with dry friction Part 2. Dynamics of motion". In: *Wear* 143.2, pp. 331–352. ISSN: 0043-1648.

Grebenstein, M., M. Chalon, W. Friedl, S. Haddadin, T. Wimböck, G. Hirzinger, and R. Siegwart (2012). "The hand of the DLR Hand Arm System: Designed for interaction". In: *The International Journal of Robotics Research* 31.13, pp. 1531–1555.

Grebenstein, M., M. Chalon, M. A. Roa, and C. Borst (2018). "DLR Multi-fingered Hands". In: *Humanoid Robotics: A Reference*. Ed. by A. Goswami and P. Vadakkepat. Dordrecht: Springer Netherlands, pp. 1–41. ISBN: 978-94-007-7194-9.

Gunji, D., Y. Mizoguchi, S. Teshigawara, A. Ming, A. Namiki, M. Ishikawaand, and M. Shimojo (2008). "Grasping force control of multi-fingered robot hand based on slip detection using tactile sensor". In: *2008 IEEE International Conference on Robotics and Automation*, pp. 2605–2610.

Hartman, P. (Jan. 2002). *Ordinary Differential Equations*. Society for Industrial and Applied Mathematics.

Haustein, J. A., S. Cruciani, R. Asif, K. Hang, and D. Kragic (2019). "Placing Objects with prior In-Hand Manipulation using Dexterous Manipulation Graphs". In: *2019 IEEE-RAS 19th International Conference on Humanoid Robots (Humanoids)*, pp. 453–460.

Hermann, R. and A. Krener (1977). "Nonlinear controllability and observability". In: *IEEE Transactions on Automatic Control* 22.5, pp. 728–740.

Hertz, H. R. (1882). "On the Contact of Rigid Elastic Solids and on Hardness". In: *Ch 6: Assorted Papers*.

Heyneman, B. and M. R. Cutkosky (2013). "Slip interface classification through tactile signal coherence". In: *2013 IEEE/RSJ International Conference on Intelligent Robots and Systems*, pp. 801–808.

Ho, V. A., Z. Wang, and S. Hirai (2013). "Beam bundle model of human-like fingertip for investigation of tactile mechanism". In: *2013 IEEE/RSJ International Conference on Intelligent Robots and Systems*, pp. 4491–4498.

Hogan, F., J. Ballester, S. Dong, and A. Rodriguez (2020). "Tactile Dexterity: Manipulation Primitives with Tactile Feedback". In: *ICRA*.

Hornik, K. (1991). "Approximation capabilities of multilayer feedforward networks". In: *Neural Networks* 4.2, pp. 251–257. ISSN: 0893-6080.

Hou, Y., Z. Jia, and M. Mason (2019). *Reorienting Objects in 3D Space Using Pivoting*.

Hou, Y., Z. Jia, and M. Mason (2020). *Manipulation with Shared Grasping*.

Howe, R. D. and M. R. Cutkosky (1996). "Practical Force-Motion Models for Sliding Manipulation". In: *The International Journal of Robotics Research* 15.6, pp. 557–572.

Huang, B., M. Li, R. L. De Souza, J. J. Bryson, and A. Billard (June 2016). "A modular approach to learning manipulation strategies from human demonstration". In: *Autonomous Robots* 40.5, pp. 903–927. ISSN: 1573-7527.

IFR International Federation of Robotics (2018). *World Robotics Industrial Robots and Service Robots*. Tech. rep.

Johanastrom, K. and C. Canudas De Wit (2008). "Revisiting the LuGre friction model". In: *IEEE Control Systems Magazine* 28.6, pp. 101–114.

Johannes, V., M. Green, and C. Brockley (1973). "The role of the rate of application of the tangential force in determining the static friction coefficient". In: *Wear* 24.3, pp. 381–385. ISSN: 0043-1648.

Kaboli, M., K. Yao, and G. Cheng (2016). "Tactile-based manipulation of deformable objects with dynamic center of mass". In: *2016 IEEE-RAS 16th International Conference on Humanoid Robots (Humanoids)*, pp. 752–757.

Karaman, S. and E. Frazzoli (2011). "Sampling-based algorithms for optimal motion planning". In: *The International Journal of Robotics Research* 30.7, pp. 846–894.

Kawasaki, H., T. Komatsu, K. Uchiyama, and T. Kurimoto (1999). "Dexterous anthropomorphic robot hand with distributed tactile sensor: Gifu hand II". In: *IEEE SMC'99 Conference Proceedings. 1999 IEEE International Conference on Systems, Man, and Cybernetics (Cat. No.99CH37028)*. Vol. 2, 782–787 vol.2.

Khalil, H. K. (2002). *Nonlinear systems; 3rd ed.* Upper Saddle River, NJ: Prentice-Hall.

Kingston, Z., M. Moll, and L. Kavraki (2017). "Decoupling Constraints from Sampling-Based Planners". In: *International Symposium of Robotics Research.*

Kuhn, H. and M. Sternbeck (June 2013). "Integrative retail logistics: An exploratory study". In: *Operations Management Research* 6.1, pp. 2–18. ISSN: 1936-9743.

Li, J., S. Dong, and E. Adelson (2018). "Slip Detection with Combined Tactile and Visual Information". In: *2018 IEEE International Conference on Robotics and Automation (ICRA)*, pp. 7772–7777.

Lynch, K. and F. Park (2017). *Modern Robotics: Mechanics, Planning and Control*. New York: Cambridge University Press.

Marchand, E., F. Spindler, and F. Chaumette (2005). "ViSP for visual servoing: a generic software platform with a wide class of robot control skills". In: *IEEE Robotics & Automation Magazine* 12.4, pp. 40–52.

Marques, F., P. Flores, J. C. Pimenta Claro, and H. M. Lankarani (Nov. 2016). "A survey and comparison of several friction force models for dynamic analysis of multibody mechanical systems". In: *Nonlinear Dynamics* 86.3, pp. 1407–1443. ISSN: 1573-269X.

Meier, M., F. Patzelt, R. Haschke, and H. J. Ritter (2016). "Tactile Convolutional Networks for Online Slip and Rotation Detection". In: *Artificial Neural Networks and Machine Learning – ICANN 2016*. Ed. by A. E. Villa, P. Masulli, and A. J. Pons Rivero. Cham: Springer International Publishing, pp. 12–19. ISBN: 978-3-319-44781-0.

Moody, J. E. and C. J. Darken (1988). *Learning with Localized Receptive Fields*. Tech. rep. YALEU/DCS/RR-649. Yale University, Department of Computer Science.

Nassour, J., V. Ghadiya, V. Hugel, and F. H. Hamker (2018). "Design of new Sensory Soft Hand: Combining air-pump actuation with superimposed curvature and pressure sensors". In: *2018 IEEE International Conference on Soft Robotics (RoboSoft)*, pp. 164–169.

Nijmeijer, H. and A. van der Schaft (1990). *Nonlinear Dynamical Control Systems*. New York: Springer New York.

Nilsson, R. (2009). "Inverse Kinematics". MA thesis. Luleå University of Technology.

Palli, G., C. Melchiorri, G. Vassura, U. Scarcia, L. Moriello, G. Berselli, A. Cavallo, G. D. Maria, C. Natale, S. Pirozzi, C. May, F. Ficuciello, and B. Siciliano (2014). "The DEXMART hand: Mechatronic design and experimental evaluation of synergy-based control for human-like grasping". In: *The International Journal of Robotics Research* 33.5, pp. 799–824.

Papazov, C. and D. Burschka (2011). "An Efficient RANSAC for 3D Object Recognition in Noisy and Occluded Scenes". In: *Computer Vision – ACCV 2010*. Ed. by R. Kimmel, R. Klette, and A. Sugimoto. Berlin, Heidelberg: Springer Berlin Heidelberg, pp. 135–148. ISBN: 978-3-642-19315-6.

Piazza, C., G. Grioli, M. Catalano, and A. Bicchi (2019). "A Century of Robotic Hands". In: *Annual Review of Control, Robotics, and Autonomous Systems* 2.1, pp. 1–32.

Regoli, M., U. Pattacini, G. Metta, and L. Natale (2016). "Hierarchical grasp controller using tactile feedback". In: *2016 IEEE-RAS 16th International Conference on Humanoid Robots (Humanoids)*, pp. 387–394.

Reinecke, J., A. Dietrich, F. Schmidt, and M. Chalon (2014). "Experimental comparison of slip detection strategies by tactile sensing with the BioTac® on the DLR hand arm system". In: *2014 IEEE International Conference on Robotics and Automation (ICRA)*, pp. 2742–2748.

Richardson, R. and H. Nolle (1976). "Surface friction under time-dependent loads". In: *Wear* 37.1, pp. 87–101. ISSN: 0043-1648.

Romano, J. M., K. Hsiao, G. Niemeyer, S. Chitta, and K. J. Kuchenbecker (2011). "Human-Inspired Robotic Grasp Control With Tactile Sensing". In: *IEEE Transactions on Robotics* 27.6, pp. 1067–1079.

Rosset, L. M., M. Florek-Jasinska, M. Suppa, and M. A. Roa-Garzón (2019). "Experimental study on model- vs. learning-based slip detection". In: *2019 19th International Conference on Advanced Robotics (ICAR)*, pp. 493–500.

Ruderman, M. (2017). "On break-away forces in actuated motion systems with nonlinear friction". In: *Mechatronics* 44, pp. 1–5. ISSN: 0957-4158.

Rusinkiewicz, S. and M. Levoy (2001). "Efficient variants of the ICP algorithm". In: *Proceedings Third International Conference on 3-D Digital Imaging and Modeling*, pp. 145–152.

Santello, M., M. Flanders, and J. F. Soechting (1998). "Postural Hand Synergies for Tool Use". In: *Journal of Neuroscience* 18.23, pp. 10105–10115. ISSN: 0270-6474.

Schoepfer, M., C. Schuermann, M. Pardowitz, and H. Ritter (2010). "Using a Piezo-Resistive Tactile Sensor for Detection of Incipient Slippage". In: *ISR 2010 (41st International Symposium on Robotics) and ROBOTIK 2010 (6th German Conference on Robotics)*, pp. 1–7.

Shadow Robot Company (2003). "Design of a dexterous hand for advanced Clawar applications". In: *Proceedings International Conference Climbing Walking Robots*, pp. 691–698.

Shi, J., H. Weng, and K. Lynch (2020). "In-Hand Sliding Regrasp With Spring-Sliding Compliance and External Constraints". In: *IEEE Access* 8, pp. 88729–88744.

Shi, J., J. Z. Woodruff, P. B. Umbanhowar, and K. M. Lynch (2017). "Dynamic In-Hand Sliding Manipulation". In: *IEEE Transactions on Robotics* 33.4, pp. 778–795.

Shkulipa, S., W. den Otter, and W. Briels (2005). "Surface Viscosity, Diffusion, and Intermonolayer Friction: Simulating Sheared Amphiphilic Bilayers". In: *Biophysical Journal* 89.2, pp. 823–829. ISSN: 0006-3495.

Sontag, E. (2008). "Input to State Stability: Basic Concepts and Results". In: *P. Nistri and G. Stefani, Nonlinear and Optimal Control Theory.* Springer-Verlag Berlin Heidelberg, pp. 163–220.

Spiers, A. J., M. V. Liarokapis, B. Calli, and A. M. Dollar (2016). "Single-Grasp Object Classification and Feature Extraction with Simple Robot Hands and Tactile Sensors". In: *IEEE Transactions on Haptics* 9.2, pp. 207–220.

Stepputtis, S., Y. Yang, and H. Ben Amor (2018). "Extrinsic Dexterity Through Active Slip Control Using Deep Predictive Models". In: *2018 IEEE International Conference on Robotics and Automation (ICRA)*, pp. 3180–3185.

Sucan, I., M. Moll, and L. Kavraki (2012). "The Open Motion Planning Library". In: *IEEE Robotics Automation Magazine* 19.4, pp. 72–82.

Torres-Jara, E. and L. Natale (Feb. 2018). "Sensitive Manipulation: Manipulation Through Tactile Feedback". In: *International Journal of Humanoid Robotics* 15.01, p. 1850012.

Toussaint, M. (2009). "Robot Trajectory Optimization Using Approximate Inference". In: *Proceedings of the 26th Annual International Conference on Machine Learning*. ICML '09. Montreal, Quebec, Canada: Association for Computing Machinery, pp. 1049–1056. ISBN: 9781605585161.

Ueda, J., A. Ikeda, and T. Ogasawara (2005). "Grip-force control of an elastic object by vision-based slip-margin feedback during the incipient slip". In: *IEEE Transactions on Robotics* 21.6, pp. 1139–1147.

van Hoof, H., T. Hermans, G. Neumann, and J. Peters (2015). "Learning robot in-hand manipulation with tactile features". In: *2015 IEEE-RAS 15th International Conference on Humanoid Robots (Humanoids)*, pp. 121–127.

Veiga, F., H. van Hoof, J. Peters, and T. Hermans (2015). "Stabilizing novel objects by learning to predict tactile slip". In: *2015 IEEE/RSJ International Conference on Intelligent Robots and Systems (IROS)*, pp. 5065–5072.

Viña B., F. E., Y. Karayiannidis, C. Smith, and D. Kragic (2016). "Adaptive control for pivoting with visual and tactile feedback". In: *2016 IEEE International Conference on Robotics and Automation (ICRA)*, pp. 399–406.

Wang, C., D. Xu, Y. Zhu, R. Martín-Martín, C. Lu, L. Fei-Fei, and S. Savarese (2019). "DenseFusion: 6D Object Pose Estimation by Iterative Dense Fusion". In: *2019 IEEE/CVF Conference on Computer Vision and Pattern Recognition (CVPR)*, pp. 3338–3347.

Xydas, N. and I. Kao (1999). "Modeling of Contact Mechanics and Friction Limit Surfaces for Soft Fingers in Robotics, with Experimental Results". In: *The International Journal of Robotics Research* 18.9, pp. 941–950.

Yanqian, Y., C. Sui-lin, and L. Chi Y (1986). *Theory of limit cycles*. Vol. 66. Translations of mathematical monographs. Providence, R.I.: American Mathematical Society.

Zapata-Impata, B., P. Gil, and F. Torres (Jan. 2019). "Learning Spatio Temporal Tactile Features with a ConvLSTM for the Direction Of Slip Detection". In: *Sensors* 19.3, p. 523. ISSN: 1424-8220.

Zeng, A., S. Song, J. Lee, A. Rodriguez, and T. Funkhouser (2020). "TossingBot: Learning to Throw Arbitrary Objects With Residual Physics". In: *IEEE Transactions on Robotics* 36.4, pp. 1307–1319.

Zhao, J. and D. Hill (2008). "On stability, L_2-gain and H_∞ control for switched systems". In: *Automatica* 44.5, pp. 1220–1232. ISSN: 0005-1098.

Zhou, J., Y. Hou, and M. Mason (2019). “Pushing revisited: Differential flatness, trajectory planning, and stabilization”. In: *The International Journal of Robotics Research* 38.12-13, pp. 1477–1489.